High field dynamic nuclear polarization methods: Microwave sources and mechanisms

by

Michael Mardini

A.B. Chemistry, Washington University in St. Louis, 2016

Submitted to the Department of Chemistry
in partial fulfillment of the requirements for the degree of

DOCTOR OF PHILOSOPHY IN CHEMISTRY

at the

MASSACHUSETTS INSTITUTE OF TECHNOLOGY

February 2024

Authored by:	Michael Mardini Department of Chemistry September 27, 2023
Certified by:	Robert G. Griffin Arthur Amos Noyes Professor of Chemistry Thesis Supervisor
Accepted by:	Adam P. Willard Professor of Chemistry Graduate Officer

This doctoral thesis has been examined by a committee of the Department of Chemistry as follows:

Professor Keith A. Nelson: _____

Thesis Committee Chair
Haslam and Dewey Professor of Chemistry

Professor Robert G. Griffin: _____

Thesis Supervisor
Arthur Amos Noyes Professor of Chemistry

Professor Mei Hong: _____

Thesis Committee Member
Professor of Chemistry

High field dynamic nuclear polarization methods: Microwave sources and mechanisms

by

Michael Mardini

Submitted to the Department of Chemistry
on September 27, 2023 in partial fulfillment of the requirements for the degree of

DOCTOR OF PHILOSOPHY IN CHEMISTRY

ABSTRACT

In thirty years of active development, dynamic nuclear polarization (DNP) has emerged as a forefront technique for expanding the scope of solid state nuclear magnetic resonance. For the most part, and particularly at high fields, these advances have come with continuous-wave microwave irradiation and the introduction of nitroxide-based biradicals exploiting the cross effect mechanism. In this thesis, I argue that this approach is not necessarily optimal and report progress towards arbitrary-waveform DNP, in the construction of a suitable solid-state microwave source, and the use of narrow-line monoradicals exploiting the Overhauser effect. My colleagues and I have also investigated the Overhauser mechanism through selective deuteration of radicals, leading to a relatively simple modification which yielded a significant increase in Overhauser enhancement. Finally, I detail studies of two unexplored DNP mechanisms in trityl: the three-spin solid effect and resonant mixing. With solid-state microwave sources and Overhauser radicals, DNP is now more accessible as we can achieve reasonable enhancement without the need for a gyrotron. Moreover, as amplifier and resonator technologies continue to develop, it is likely that pulsed DNP will emerge at high fields and overtake continuous-wave DNP in absolute sensitivity enhancement as well.

Thesis supervisor: Robert G. Griffin
Title: Arthur Amos Noyes Professor of Chemistry

Acknowledgments

I'm only at this point thanks to the help and support of so many people over the years. I'd like to thank Bob Griffin, my esteemed advisor all this time, who's provided so much guidance and perspective for my work. I also thank the other members of my thesis committee, Mei Hong and Keith Nelson, for their time and their helpful input. I should also thank a previous student of Bob's and my advisor during my time as an undergraduate at WashU, Xander Barnes, who got me into physical chemistry and the field of DNP in the first place.

To everyone I've met during my time in the Griffin group, I thank you for your camaraderie through it all. In particular I've had the pleasure of working closely with several amazing postdocs, Christy, Kong, Ravi, and Yifan, all of whom have helped me both at a fundamental level and also by teaching me how to be a researcher. Ravi especially has been a true catalyst for curiosity-driven research and in always pushing our experiments to be better. My fellow graduate students in the group have been my mentors and teammates, and I'd specifically like to thank Qing and Cody who, all of those years ago in the midst of wrapping their time up, taught me to run the 380 MHz spectrometer that has been my home base since. Dan, Brian, Natalie, and Yifu, thank you for working with me all this time, offering help when needed and even just for being there for all those meetings and outings. None of our work would be possible without the support of Dr. Dave Ruben, who built most of the NMR spectrometers here and continues to answer questions and update software as needed, nor our technicians Ajay Thakkar, Mike Mullins, and Stephen Thomson. And of course my thanks to Jill and Wanda for help on the administrative side of things, I've certainly needed it.

Several collaborators have also made my work possible. Here at MIT, we have our organic chemistry friends Tim Swager and Léo Delage-Laurin for their preparations of several deuterated variants of BDPA and their general assistance and perspective for the project. Over at Bruker, Ivan Sergeyev, Dan Banks, James Kempf, and the late Melanie Rosay have all provided us instrument time and other assistance. Eric Bryerton and Virginia Diodes, Inc. have been integral to our collaboration incorporating their technology into our DNP system. Yangping Liu and Weixiang Zhai at Tianjin Medical University provided some interesting modified trityls, and Snorri Sigurdsson, Iram Ahmad, and Sucharita Mandal at the University of Iceland kindly provided us with freshly synthesized NMe_3-BDPA to test.

To my cohort of physical chemistry PhD students, I extend my gratitude as I can still think fondly of working on PSets for hours (somehow...). And in the following years I'm happy to have had so many wonderful smart people as my friends, especially Ray, Amr,

Lexie, Megan, Tom, Mari, and Jesse.

To my friends from college, Avi, Sreyas, and Braham, with whom I played Mahjong online every Saturday in the height of quarantine: thank you for keeping me going, it really was the highlight of my week and I'm glad we've all grown closer since. Carter, my man: you're a great friend, even if I am so bad at keeping in touch that all we do is talk about fighting games for a bit every couple months. Speaking of fighting games, to those I've met through my hobby, especially Spencer, Branch, Kane, and Brandon: much love, and even if I end up leaving Boston you can bet I'll be back for Beach Episode.

Many thanks to my sister Julie. Not only can we share a laugh at any moment, no matter how long it's been, but she's also one of the most thoughtful and kind people I know, plus now she's a super girlboss lawyer lady and I love that for her. And finally my parents, Antwan and Jemma, who have supported me from the start and still do in so many ways.

Contents

List of Figures

List of Tables

Chapter 1

Introduction

Solid-state nuclear magnetic resonance (NMR) can determine atomic level details of nearly anything one can pack into a rotor, including applications to biomolecular and materials science studies. The information comes from our ability to detect, resolve, and interpret signals from individual nuclei, which inevitably becomes more challenging for more complex systems. Fundamentally, we have access to multidimensional NMR, which can essentially sacrifice sensitivity for resolution and thereby facilitate interpretation. For conventional NMR, the ultimate source (and limit) of sensitivity, beyond conditions of any particular pulse sequence or instrumentation, is the slight polarization of nuclear spins at thermal equilibrium. Hyperpolarization techniques, including my area of research, dynamic nuclear polarization (DNP), aim to exceed that limit; DNP does so by using microwave irradiation to transfer polarization from unpaired electrons (radicals) to nuclei of interest. At high magnetic fields, the state-of-the-art for DNP currently involves continuous-wave (CW) microwave sources and polarizing agents supporting cross-effect (CE) DNP mechanisms. For several reasons, these methods are not optimal, and my aim in this thesis is to introduce instrumentation which can already provide tangible advantages and will prove essential for future DNP methods. In this chapter, I first provide a summary of the NMR experiment and the definition of polarization and detail

some of the interactions relevant to solid-state NMR. Then, I discuss fundamentals of continuous-wave DNP and the existing research on pulsed DNP. Finally, I briefly survey microwave technology applicable to DNP at high fields.

1.1 Overview of nuclear magnetic resonance

1.1.1 Nuclear magnetism

In the early days of quantum physics, Stern and Gerlach demonstrated the quantization of the magnetic moment of silver atoms[1], in accordance with the idea of a quantized intrinsic angular momentum, which would come to be called spin. It turned out that they had actually observed the electron spin in this early experiment, but Stern and colleagues' later experiments on hydrogen molecules[2, 3] measured the magnetic moment of the ^{1}H nucleus, i.e. the proton. Later, Alvarez and Bloch also measured the neutron magnetic moment[4]. Spin and magnetic moment are related via:

$$\boldsymbol{\mu} = g\frac{e}{2m}\mathbf{S} \tag{1.1}$$

for elementary fermions (e.g. electrons and quarks) where $\boldsymbol{\mu}$ and $\mathbf{S}$ are the magnetic moment and spin angular momentum vectors, respectively, e is the elementary charge, m is the particle mass, and g a dimensionless quantity (the g-factor) specific to each type of particle. Composite particles such as protons, neutrons, and nuclei in general have a magnetic moment defined using the proton mass m_p instead:

$$\boldsymbol{\mu} = g\frac{e}{2m_\mathrm{p}}\mathbf{I} \tag{1.2}$$

where again each particle has its own g-factor and we use $\mathbf{I}$ by convention to refer to nuclear spin. We typically use the gyromagnetic ratio to express the relationship between

magnetic moment and spin:

$$\boldsymbol{\mu}_I = \gamma_I \mathbf{I}. \tag{1.3}$$

When placed in an external magnetic field $\mathbf{B}_0$, a magnetic moment tends to align itself with the field vector. This interaction is the Zeeman interaction[5] and has an associated Hamiltonian

$$\hat{H}_Z = -\hat{\boldsymbol{\mu}} \cdot \mathbf{B}_0 = -\gamma \hat{\mathbf{I}} \cdot \mathbf{B}_0 = -\hat{I}_z \gamma B_0 \tag{1.4}$$

where for the final equality we can assume that $\mathbf{B}_0$ is aligned with the z-axis. The nucleus has spin S, which can take values $0, \frac{1}{2}, 1, \frac{3}{2}, \ldots$, and for a given value of S there are $2S+1$ eigenstates of $\hat{I}_z$, each with an associated spin quantum number m_S:

$$\hat{I}_z \left| S; m_S \right\rangle = \hbar m_S \left| S; m_S \right\rangle; \quad m_S = -S, -S+1, \ldots, S-1, S. \tag{1.5}$$

In the simplest nonzero case, $S = \frac{1}{2}$, there are two eigenstates of $\hat{H}_Z$, with magnetic moments $\mu_{z\pm} = \pm\gamma\hbar/2$ and energies $E_\pm = \mp\hbar\gamma B_0/2$. Their energy difference is

$$\Delta E = |\hbar \gamma B_0| \tag{1.6}$$

This energy difference leads to a very slight bulk magnetic moment, as the lower state is preferentially occupied according to the Boltzmann distribution. We can calculate the relative difference between the populations, the *polarization*:

$$P = \frac{N_+ - N_-}{N_+ + N_-} = \frac{e^{-\hbar\gamma B_0/2k_B T} - e^{+\hbar\gamma B_0/2k_B T}}{e^{-\hbar\gamma B_0/2k_B T} + e^{+\hbar\gamma B_0/2k_B T}} = \tanh\left(\frac{\hbar\gamma B_0}{2k_B T}\right) \approx \frac{\hbar\gamma B_0}{2k_B T} \tag{1.7}$$

where k_B is the Boltzmann constant and T the temperature, and we have assumed $\gamma > 0$ so that $m_S = +\frac{1}{2}$ is the lower-energy state. The final approximation relies on $|\hbar\gamma B_0| \ll T$, which we refer to as the high-temperature approximation and is generally valid for nuclei even at very high fields and liquid helium temperatures. The bulk

magnetic moment at equilibrium is the sum of the $N = (N_+ + N_-)$ individual magnetic moments:[6]

$$M_{\text{eq}} = N_+\mu_{z+} + N_-\mu_{z-} = (N_+ - N_-)\frac{\hbar\gamma}{2} = N\frac{\hbar\gamma B_0}{2k_{\text{B}}T}\frac{\hbar\gamma}{2} = \frac{N\hbar^2\gamma^2 B_0}{4k_{\text{B}}T}. \tag{1.8}$$

1.1.2 The development of nuclear magnetic resonance

The primary method to detect this magnetic moment is *magnetic resonance*. The term refers to stimulation of transitions between the spin states by application of an oscillating magnetic field; when the frequency of oscillation matches the energy level difference, resonance can be observed through some detection scheme. Rabi and colleagues demonstrated this nuclear magnetic resonance effect on molecular beams[7]; the use of electromagnetic radiation (usually radiofrequencies, hence the common term "RF" for irradiation during NMR experiments) came about somewhat later in the works of Purcell[8] and Bloch[9]. For these experiments, a sample is placed within both the static field $\mathbf{B}_0$ and a coil whose axis is perpendicular to the main field. Conceptually, when the resonance condition is met in this setup, the net magnetization of the sample will begin to precess about the axis of the oscillating field, rather than about $\mathbf{B}_0$. The changing magnetic moment changes the magnetic field and thus also the current through the coil, which we can actively monitor, and because the magnetization is a bulk property the effect is actually large enough that we can detect it, making nuclear magnetic resonance spectroscopy reasonable for many samples with an abundance of nuclei with nonzero spin.

The utility of NMR for chemists would be developed through the understanding of *internal* spin interactions, in contrast to the external interactions with the static and perturbing magnetic fields. We will survey these briefly later in this section, but for now we will continue with the description of the experiment. The works of Purcell and Bloch are known as continuous-wave (CW) NMR, as the RF irradiation is constantly active and

its frequency or, more often, the static field strength is varied until resonance is observed. A transformative shift came about with Fourier transform (FT) or simply pulsed NMR: Ernst and Anderson[10] demonstrated faster acquisition of spectra with improved sensitivity by applying a short, intense RF pulse to start the experiment. This excites all nuclei whose frequency is in the vicinity of the RF, and the strong pulse places the magnetization in the transverse plane, far from equilibrium. Each nuclear spin will now precess at its own frequency, contributing accordingly to the induced current; by using phase-sensitive (quadrature) detection of this *free induction decay* (FID) relative to the transmitter reference, we functionally measure the x and y components of the magnetization vector in the rotating frame as a function of time. Fourier transformation of the time domain signal produces a set of peaks in the frequency domain, each associated with a particular type of nucleus.

Not only do pulsed experiments represent an increase in throughput and quality of NMR spectra, but they enable us to conceptualize new types of experiments in which we manipulate the spin system and Hamiltonian to tease out specific interactions. A wide variety of pulse sequences have been developed for various purposes; many of these employ multidimensional spectroscopy to 1) measure two or more different frequencies and 2) establish or measure a correlation between them. The basic paradigm of two-dimensional NMR spectroscopy is[11] 1) preparation of the system with an initial RF pulse, 2) indirect evolution for time t_1, 3) an optional mixing period, often with additional RF pulses, to transfer magnetization to a different set of nuclei, and 4) the traditional direct detection of the FID during time t_2. The indirect evolution refers to the incrementing of t_1 in separate acquisitions; additional indirect dimensions can be added for higher-dimensional spectroscopy. Fourier transformation along each time dimension yields for each frequency detected during t_1 a set of frequencies during t_2; these correlations are caused by the mixing period and can be interpreted in the context of which interactions are active during the mixing. Unless a particular interaction is be-

ing measured, a multidimensional spectrum pulls apart the peaks of a one-dimensional spectrum, so signals are better resolved and more easily assigned. These sequences are generally less sensitive than one-dimensional experiments: there is additional relaxation during the evolution and mixing periods and the mixing is not always a perfect transfer of magnetization. In terms of time, the indirect detection means that a separate FID is collected for each t_1 point, further lowering the acquisition rate; this problem is compounded with each additional indirect dimension. Multidimensional spectra are so useful that we are willing to collect them for hours, days, or even weeks, but they do highlight a major challenge of NMR, low sensitivity, which we will revisit shortly.

1.1.3 Internal spin interactions

The interesting information we can extract with NMR is contained in the *internal* interactions of the spin system. All the terms in the NMR spin Hamiltonian can be written as a coupling of two vectors via some coupling tensor:

$$\hat{H} = \hat{\mathbf{I}} \cdot \overrightarrow{\mathbf{A}} \cdot \hat{\mathbf{J}}. \tag{1.9}$$

We can categorize the different interactions by what the vectors $\hat{\mathbf{I}}$ and $\hat{\mathbf{J}}$ refer to. We start with those linear in the spin operators; that is, only $\hat{\mathbf{I}}$ is actually a vector of spin operators, and $\hat{\mathbf{J}}$ is actually an external vector, usually the magnetic field. We have already seen that (cf. Equation (1.4))

$$\hat{H}_Z = \hat{\mathbf{I}} \cdot \left(-\gamma \overrightarrow{\mathbf{1}}\right) \cdot \mathbf{B}_0 \quad and \quad \hat{H}_{RF} = \hat{\mathbf{I}} \cdot \left(-\gamma \overrightarrow{\mathbf{1}}\right) \cdot \mathbf{B}_1. \tag{1.10}$$

We now introduce the *chemical shift* interaction, which is a consequence of the electron orbitals in the vicinity of the spin.[12] When an external magnetic field is applied, it induces a current in the electrons. That current in turn generates a local magnetic field at the nucleus, which we describe as a "shielding" of the nuclear spin from the external

magnetic field according to the chemical shielding tensor $\overrightarrow{\boldsymbol{\sigma}}$. The chemical shift refers to the fact that measuring the strength of this interaction, which amounts to a shift from the expected frequency for an isolated nucleus, gives a direct and sensitive report on the chemical environment of the nucleus. Each nucleus in a molecule has its own chemical shift, and its measurement is foundational for NMR spectroscopy in practice; from the chemical shift information we can determine the identity and purity of a substance, as is routine for organic synthetic chemists, and we can combine the assignments with other techniques for atomic-level dynamics and structural information.

We can combine $\overrightarrow{\boldsymbol{\sigma}}$ with the Zeeman interaction (Equation (1.4)):

$$\hat{H}_{\mathrm{Z,CS}} = -\gamma \hat{\mathbf{I}} \cdot \left(\overrightarrow{\mathbf{1}} - \overrightarrow{\boldsymbol{\sigma}} \right) \cdot \mathbf{B}_0. \tag{1.11}$$

The elements of $\overrightarrow{\boldsymbol{\sigma}}$ depend on the details of the electron distribution around the nucleus and on the orientation of the molecule with respect to $\mathbf{B}_0$. We often make a high-field approximation and disregard terms in the Hamiltonian which do not commute with $\hat{I}_z$, as the Zeeman interaction is much stronger than the internal interactions. In this case, only the $\sigma_{zz}^{(\mathrm{lab})}$ term survives:

$$\hat{H}_{\mathrm{Z,CS}} = -\gamma B_0 (1 - \sigma_{zz}^{(\mathrm{lab})}) \hat{I}_z \tag{1.12}$$

with the (lab) superscript indicating the laboratory frame of reference and suggestive that this component of the tensor is usually determined via transformation to other frames. If the tensor $\overrightarrow{\boldsymbol{\sigma}}$ is *symmetric* (equal to its transpose)[1] then we know we can diagonalize it via an orthogonal transformation, i.e. a change of frame/basis.[6] The frame in which $\overrightarrow{\boldsymbol{\sigma}}$ is diagonal is the principal axis system (PAS) and the three nonzero elements are σ_{XX}, σ_{YY}, and σ_{ZZ}. We can go from the PAS representation to the laboratory

[1] We can express any matrix as the sum of a symmetric and antisymmetric matrix. When we do so for the chemical shielding tensor, the antisymmetric component does not contribute to the truncated Hamiltonian so we can disregard it.

frame via a rotation by the Euler angles $\Omega_{LP} = \{\alpha_{LP}, \beta_{LP}, \gamma_{LP}\}$:[12]

$$\overrightarrow{\boldsymbol{\sigma}}^{(\text{lab})} = \mathcal{R}(\Omega_{LP})\overrightarrow{\boldsymbol{\sigma}}^{(\text{PAS})}\mathcal{R}(\Omega_{PL}) \tag{1.13}$$

where $\mathcal{R}$ is the Cartesian rotation matrix, and $\mathcal{R}(\Omega_{PL}) = \mathcal{R}(\Omega_{LP})^{\dagger}$. We can do this calculation and find that

$$\sigma_{zz}^{(\text{lab})} = \sigma_{XX}\sin^2\beta\cos^2\gamma + \sigma_{YY}\sin^2\beta\sin^2\gamma + \sigma_{ZZ}\cos^2\beta. \tag{1.14}$$

Often, we express chemical shielding as

$$\sigma_{zz}^{(\text{lab})} = \sigma_{\text{iso}} + \frac{1}{2}\delta\left(3\cos^2\theta - 1 - \eta\sin^2\theta\cos 2\phi\right) \tag{1.15}$$

where $\sigma_{\text{iso}} = \frac{1}{3}(\sigma_{XX} + \sigma_{YY} + \sigma_{ZZ})$, $\delta = \sigma_{ZZ} - \sigma_{\text{iso}}$, and $\eta = (\sigma_{YY} - \sigma_{XX})/\delta$, and we have replaced the angles β and γ by θ and ϕ, respectively.

The next set of terms are bilinear in the spin operators: $\hat{\mathbf{I}}$ and $\hat{\mathbf{J}}$ in Equation (1.9) are two different spin operator vectors $\hat{\mathbf{I}}_1$ and $\hat{\mathbf{I}}_2$. These mechanisms are important as they enable the possibility of magnetization transfer between two spins. One mechanism for this is the magnetic dipole-dipole interaction, which is a through-space interaction directly resulting from the magnetic field due to one spin being felt at another nearby. We can express this as

$$\hat{H}_{\text{DD}}^{(12)} = b_{12}\left(\frac{3(\hat{\mathbf{I}}_1\cdot\mathbf{r}_{12})(\hat{\mathbf{I}}_2\cdot\mathbf{r}_{12})}{r_{12}^2} - \hat{\mathbf{I}}_1\cdot\hat{\mathbf{I}}_2\right), \tag{1.16}$$

where $b_{12} = -\mu_0\gamma_1\gamma_2\hbar/4\pi r_{12}^3$, with μ_0 the vacuum permeability and r_{12} the internuclear distance, and $\mathbf{r}_{12}$ the vector connecting the two spins. Invoking the same high-field

approximation, we can truncate Equation (1.16) to

$$\hat{H}_{\mathrm{DD}}^{(12)} = b_{12} \cdot \frac{1}{2}\Big(3\cos^2\theta_{12} - 1\Big)\big(3\hat{I}_{1z}\hat{I}_{2z} - \mathbf{I}_1 \cdot \mathbf{I}_2\big) \tag{1.17}$$

where θ_{12} is the angle between the vector $\mathbf{r}_{12}$ and the magnetic field $\mathbf{B}_0$. In the form of Equation (1.9) this is

$$\hat{H}_{\mathrm{DD}}^{(12)} = \hat{\mathbf{I}}_1 \cdot \overrightarrow{\boldsymbol{D}} \cdot \hat{\mathbf{I}}_2 = b_{12}\Big(3\cos^2\theta_{12} - 1\Big)\left(\hat{\mathbf{I}}_1 \cdot \begin{pmatrix} -\frac{1}{2} & 0 & 0 \\ 0 & -\frac{1}{2} & 0 \\ 0 & 0 & 1 \end{pmatrix} \cdot \hat{\mathbf{I}}_2\right). \tag{1.18}$$

If the spins are heteronuclei ($\gamma_1 \neq \gamma_2$) we can simplify Equation (1.17) further to

$$\hat{H}_{\mathrm{DD}}^{(12)} = b_{12} \cdot \frac{1}{2}\Big(3\cos^2\theta_{12} - 1\Big)2\hat{I}_{1z}\hat{I}_{2z}. \tag{1.19}$$

The dipolar interaction directly contains structural information through the distance dependence. That is, if one measures the strength of the dipolar coupling between two nuclei, one can read out the distance between them; with enough such distances (or, more often, bounds on the possible distances) one can solve for a complete set of atomic coordinates: a structure like one would get from crystallography.

The other bilinear interaction we frequently encounter in NMR is the J-coupling: an indirect coupling between two spins mediated by bonding electrons. Like the chemical shielding interaction, the J-coupling is very useful for chemists: it is informed by the nature of the electron distribution around the nuclei and reports on the chemical environment. The Hamiltonian for the interaction is

$$\hat{H}_{\mathrm{J}}^{(12)} = 2\pi\hat{\mathbf{I}}_1 \cdot \overrightarrow{\boldsymbol{J}} \cdot \hat{\mathbf{I}}_2 \tag{1.20}$$

where the 2π is included as the J-coupling tensor is typically expressed in Hz. While $\overrightarrow{\boldsymbol{J}}$

is in principle anisotropic, the anisotropy is small enough it can be ignored, and even if not it will have the same form as the direct dipolar coupling[12]. So we use the isotropic value $J_{12} = \frac{1}{3}\mathrm{Tr}\left[\overrightarrow{J}\right]$ as in

$$\hat{H}_{\mathrm{J}}^{(12)} = \begin{cases} 2\pi J_{12}\hat{\mathbf{I}}_1 \cdot \hat{\mathbf{I}}_2 & \text{homonuclear} \\ 2\pi J_{12}\hat{I}_{1z}\hat{I_{2z}} & \text{heteronuclear} \end{cases} \tag{1.21}$$

The final type of interaction is quadratic in the spin operators: both $\hat{\mathbf{I}}$ and $\hat{\mathbf{J}}$ in Equation (1.9) refer to the same spin. This category contains the quadrupolar interaction, which involves the electric quadrupole moment of the nucleus and the electric field gradient (EFG) due to the electrons around it. The electric quadrupole moment Q is only nonzero for nuclei with spin $I > 1/2$. For these nuclei,

$$\hat{H}_{\mathrm{Q}} = \frac{eQ}{2I(2I-1)\hbar}\hat{\mathbf{I}} \cdot \overrightarrow{V} \cdot \hat{\mathbf{I}}. \tag{1.22}$$

$\overrightarrow{V}$ is the electric field gradient tensor and again is anisotropic. The quadrupolar interaction is often large, even compared to the Zeeman interaction, so the secular approximation is not always valid. The EFG tensor is extremely sensitive to molecular motions, so NMR of quadrupolar nuclei can provide very accurate measurements of dynamics. But quadrupolar nuclei also tend to exhibit fast relaxation rates and broad lineshapes, rendering spectroscopy difficult. We will not concern ourselves further with quadrupolar interactions in this thesis.[2]

1.1.4 Solid-state NMR and magic angle spinning

With the interactions introduced, we can look at how these manifest in real samples. Specifically, we are concerned with the anisotropic interactions. In liquid samples, the

[2]There will be some discussion of ^{2}H nuclei ($I = 1$) but these are used only as low-γ substitutes for ^{1}H.

random tumbling of molecules in solution occurs on a much faster timescale than our NMR experiment. For that reason, we observe the effect of a time-averaged interaction: any anisotropic components are averaged to zero, and we only observe the isotropic value of the tensor. For the chemical shift and J-coupling interactions, their tensors have an isotropic value which is measured in solution NMR; the dipolar coupling tensor is traceless and the interaction not observed. To emphasize: in solution NMR, each nuclear site exhibits a single narrow peak according to the isotropic chemical shift or a small multiplet of narrow peaks due to its J-coupling interaction(s).

A molecule in a solid sample is essentially fixed in place: there may be small local motions of the atoms, but there certainly is not fast isotropic tumbling. Generally we need to use the full forms of the chemical shift anisotropy (CSA) and dipolar coupling tensors. For the chemical shift, each molecule has its own fixed orientation and will contribute a single sharp line to the spectrum, so one option is to study a single crystal of the sample, rotate it to several known orientations with a goniometer, and measure the resonance frequency as function of the orientation to determine the chemical shielding tensor. If instead we have a powder sample and we are simultaneously acquiring spectra of all possible molecular orientations, we end up with an inhomogeneously broadened lineshape for each nuclear site. An even bigger problem for solid-state NMR is the dipolar coupling. Each nucleus is coupled to each other nucleus in the sample, and the simultaneous and overlapping action of all these interactions leads to a homogeneously broadened line.

The solution for solid-state spectroscopy was to emulate the motional averaging that liquids have intrinsically. A clue for how to go about this is in Equation (1.17): if one could by some experimental means make the time average of $(3\cos^2\theta_{12} - 1)$ equal zero, the dipolar coupling would also be zero. Magic-angle spinning (MAS) was introduced[13, 14] to achieve exactly that: by mechanically rotating the sample around an axis oriented at $\theta_m \approx 54.74^\circ$ with respect to $\mathbf{B}_0$, i.e. $\cos^2\theta_m = 1/3$, narrowing of the dipolar line-

shape was observed. The chemical shift and first-order quadrupolar[3] interactions are also narrowed by this process. The degree of narrowing is dependent on the strength of the interaction relative to the spinning frequency ω_r. We accomplish the spinning by placing the sample in a small cylindrical rotor fitted with an air turbine – a controlled flow of nitrogen gas drives the rotor to spin, while gas bearings allow the rotor to float within the stator assembly as it spins. In terms of the mathematics, we introduce an additional frame, the rotor frame, which is related to the laboratory frame by $\Omega_{LR}(t) = \{0, \theta_m, \omega_r t\}$. The PAS is related to the rotor frame by a fixed set of Euler angles Ω_{RP} for each crystallite orientation, so we can compute the Hamiltonian for each using the composite rotation $\mathcal{R}_{LR}\mathcal{R}_{RP}$. As the orientation is time-dependent, so is the Hamiltonian. The non-oscillating components are the isotropic term and terms which depend on $3\cos^2\theta_m - 1$, which we have set to zero. The oscillating terms have frequency ω_r or $2\omega_r$, so the Hamiltonian and resultant FID are periodic; in the Fourier transformed spectrum, this manifests as rotational sidebands at $\omega_{iso} + n\omega_r$, where ω_{iso} is the isotropic frequency and n is an integer. The sideband manifold will fall within the static lineshape, but each sideband will be a sharp peak. Already, this is a useful result; for example, the sideband intensities can be fitted to determine CSA tensor parameters under slower MAS.[15] But when the MAS frequency is much larger than the interaction, the time-dependent terms have almost no effect on the FID as they are averaged so effectively. Under these conditions, solid-state spectra can be acquired with liquids-like resolution.

In real samples, especially those with many ^{1}H nuclei, which have strong dipolar couplings, MAS alone does not lead to well-resolved spectra. We can help further average the dipolar couplings with RF irradiation, conceptually rotating the spin vectors rather than the spatial tensor involved in the interaction. Heteronuclear decoupling is straightforward: while acquiring the FID of a nucleus such as ^{13}C, irradiation is applied at the

[3] Notably, second-order and higher terms are *not* averaged to zero under MAS.

^{1}H frequency, nutating the ^{1}H magnetization and causing its time average to be zero. Continuous-wave (CW) decoupling can yield acceptable results but other schemes[16–18] have been designed which interlace with MAS to yield greater overall narrowing while requiring less power.[4]

For all that the dipolar interaction hinders the resolution of solid-state NMR, it is also a source of structural information inaccessible via solution NMR. To that end, dipolar *recoupling* sequences have been designed which lessen, in a controlled way, the degree to which the dipolar interaction is averaged under MAS. Usually this involves synchronization of the pulse sequence or other Hamiltonian terms with the MAS, sometimes in the timing of the pulses to the rotor period as in REDOR[19], matching the difference in frequency of two nuclei to the MAS frequency as in (homonuclear) rotational resonance[20], matching the amplitude of an RF field to the MAS frequency in DARR[21], and many other permutations (see a recent review from Liang et al.[22] for a more complete compilation).

These methods can work exceptionally well for sparse spin systems, emulating the ideal case of an isolated spin pair. But we are interested in using solid-state NMR to examine large biomolecular assemblies without having to prepare a large number of specifically labeled samples. Moreover, in these systems where many dipolar interactions are active simultaneously, we are most interested in the *weakest* interactions for structural studies as these long-range distances are most likely to constrain a three-dimensional structure. Detecting such interactions requires extremely high signal-to-noise, straining the sensitivity of solid-state NMR.

[4] Using lower-power decoupling is a practical benefit. In a traditional solenoid coil an electric field is also generated at the sample which leads to sample heating, so one cannot safely apply high-power proton decoupling for long acquisition times or with short recovery delays. Even if an "E-free" coil is in use one must still consider, for example, the duty cycle of the RF amplifiers if operating near their maximum power.

1.2 Dynamic nuclear polarization

We can now move to the discussion of dynamic nuclear polarization, the main subject of this thesis. Dynamic nuclear polarization is the transfer of polarization from unpaired electrons (which themselves have spin-$\frac{1}{2}$) to nuclei for the purpose of then observing NMR signals.

1.2.1 Motivation for DNP and overview

NMR, particularly solid-state NMR, is limited by the relatively small polarization of nuclear spins at thermal equilibrium (Equation (1.7)). To quantify it, we can consider ^{1}H nuclei in a field of 23.5 T and temperature 200 K (a ^{1}H frequency of 1 GHz and a temperature near the floor of operation without specialized cryogenic equipment). In this case, $P_{1H} \approx 1.2 \times 10^{-4}$: a tiny majority of the spins align with the external field and actually contribute to the FID. Under the same conditions, the electron polarization is $P_e \approx 0.079$, almost three orders of magnitude larger as the electron gyromagnetic ratio is much larger than that of protons, $\gamma_e/\gamma_{1H} \approx 658$. If even some of this polarization can be transferred to nuclei, the bulk magnetic moment (Equation (1.8)) and thus our detected signal will be increased ("enhancement" in the parlance of DNP).

The possibility of DNP was first hypothesized by Overhauser[23] and soon thereafter observed by Carver and Slichter[24]. The experiment was straightforward: saturation of the electron spin transitions by microwave irradiation at the electron Larmor frequency led to a dynamic equilibrium that increased the effective nuclear polarization, in this case that of ^{7}Li. This effect is now referred to as the Overhauser effect and is indeed the same fundamental mechanism as the nuclear Overhauser effect often used for structural studies in solution NMR.

Other mechanisms were discovered and described, namely the solid effect[25], cross effect[26], and thermal mixing[27]. We will survey these mechanisms shortly, but each

one imposes its own requirements and restrictions on the microwave irradiation and the nature of the polarizing agent. The polarizing agent is how we introduce electron spins into a system; usually, we use a stable radical with favorable magnetic properties. With the availability of good polarizing agents, DNP can remain largely agnostic to the actual system whose NMR spectra we want to measure, making it generally applicable as a sensitivity enhancement method for any potential NMR experiment.

1.2.2 Physics of DNP

To start, we need some description of how the introduction of electron spins to the spin system changes the Hamiltonian. Many electron paramagnetic resonance (EPR) interactions are very similar as those of NMR but are described and calculated differently. For example, the environment and orientation dependence of the observed resonance frequency is no longer described as chemical shielding but rather as variance of the g value in Equation (1.1), hence the terms "g-tensor" and "isotropic g value"; this is still expressed as a coupling between the electron spin operators and the external field. Electron spins still experience through-space dipole couplings both to other unpaired electrons and to nuclei; the dipolar coupling to nuclei is part of the "hyperfine" interaction but again is of the same form as Equation (1.12). However, the electrons cannot be treated as point objects but rather their couplings have to be computed as an integral over the electron distribution. This leads to another critical distinction when electrons are involved in a magnetic interaction. Because the electron distribution can overlap with the other interacting spin, different types of interactions can manifest. When the other spin is also an electron and their wavefunctions overlap, the exchange interaction is active – in form and even notation this is like the J-coupling in NMR, but its origin is different. And when an electron wavefunction has nonzero amplitude at the site of a

nucleus, the Fermi contact interaction occurs:[28]

$$\hat{H}_{\mathrm{FC}} = \frac{8\pi\hbar}{3}\gamma_{\mathrm{e}}\gamma_{\mathrm{n}}\,\rho(\mathbf{r}_{\mathrm{n}})\hat{\mathbf{S}}\cdot\hat{\mathbf{I}} = a_{\mathrm{iso}}\hat{\mathbf{S}}\cdot\hat{\mathbf{I}} \tag{1.23}$$

where $\rho(\mathbf{r}_{\mathrm{n}})$ is the spin density of the electron at the nuclear position. The Fermi contact interaction forms the isotropic component of the combined hyperfine interaction while the dipolar interaction forms the traceless component.

While it was not the first discovered mechanism, the solid effect (SE) is the most straightforward to derive quantum mechanically. The Hamiltonian for an electron-nucleus spin system is (S operators correspond to the electron spin):

$$\hat{H} = \omega_{0\mathrm{S}}\hat{S}_{\mathrm{z}} - \omega_{0\mathrm{I}}\hat{I}_{\mathrm{z}} + \hat{\mathbf{S}}\cdot\overrightarrow{\boldsymbol{A}}\cdot\hat{\mathbf{I}}, \tag{1.24}$$

where the effects of the g-tensor and chemical shift tensor are already incorporated in the (now orientation-dependent) values for the Larmor frequency ω_0, the opposite sign of $\omega_{0\mathrm{I}}\hat{I}_{\mathrm{z}}$ reflects that a proton and nucleus have opposite sign gyromagnetic ratios, and the hyperfine tensor $\overrightarrow{\boldsymbol{A}}$ contains contributions from the Fermi contact term and the dipolar term. We would again like to truncate the Hamiltonian to the secular terms, but we must consider that of the Zeeman interactions, $|\omega_{0\mathrm{S}}| \gg |\omega_{0\mathrm{I}}|$, so our truncation now is only to those terms which commute with $\hat{S}_{\mathrm{z}}$:

$$\hat{H} = \omega_{0\mathrm{S}}\hat{S}_{\mathrm{z}} - \omega_{0\mathrm{I}}\hat{I}_{\mathrm{z}} + A_x\hat{S}_{\mathrm{z}}\hat{I}_{\mathrm{x}} + A_y\hat{S}_{\mathrm{z}}\hat{I}_{\mathrm{y}} + A_z\hat{S}_{\mathrm{z}}\hat{I}_{\mathrm{z}} \overset{\text{rotation}}{=} \omega_{0\mathrm{S}}\hat{S}_{\mathrm{z}} - \omega_{0\mathrm{I}}\hat{I}_{\mathrm{z}} + B\hat{S}_{\mathrm{z}}\hat{I}_{\mathrm{x}} + A\hat{S}_{\mathrm{z}}\hat{I}_{\mathrm{z}} \tag{1.25}$$

where the last rotation is about the z-axis and is done so only one *pseudosecular* term $B\hat{S}_{\mathrm{z}}\hat{I}_{\mathrm{x}} = \sqrt{A_x^2 + A_y^2}\,\hat{S}_{\mathrm{z}}\hat{I}_{\mathrm{x}}$ is needed. If we apply microwave irradiation at frequency $\omega_{\mu\mathrm{w}}$ and transform to the rotating frame of the irradiation:

$$\hat{H} = \Omega_{\mathrm{S}}\hat{S}_{\mathrm{z}} - \omega_{0\mathrm{I}}\hat{I}_{\mathrm{z}} + A\hat{S}_{\mathrm{z}}\hat{I}_{\mathrm{z}} + B\hat{S}_{\mathrm{z}}\hat{I}_{\mathrm{x}} + \omega_{1\mathrm{S}}\hat{S}_{\mathrm{x}}, \tag{1.26}$$

where Ω_S is the microwave frequency offset $(\omega_{0S} - \omega_{\mu w})$, and then tilt the frame so the effective field acting on the electron is along z:

$$\hat{H} = \omega_{\text{eff}}\hat{S}_z - \omega_{0I}\hat{I}_z + (\hat{S}_z\cos\theta - \hat{S}_x\sin\theta)(A\hat{I}_z + B\hat{I}_x), \tag{1.27}$$

where $\omega_{\text{eff}} = \sqrt{\omega_{1S}^2 + \Omega_S^2}$ and $\tan\theta = (\omega_{1S}/\Omega_S)$. From here, we enter the interaction frame of the electron effective field and the nuclear Zeeman field:

$$\begin{aligned}\tilde{H} = {} & A\cos\theta\hat{S}_z\hat{I}_z - A\sin\theta\Big(\hat{S}_x\cos\omega_{\text{eff}}t - \hat{S}_y\sin\omega_{\text{eff}}t\Big)\hat{I}_z \\ & + B\cos\theta\hat{S}_z\big(\hat{I}_x\cos\omega_{0I}t + \hat{I}_y\sin\omega_{0I}t\big) \\ & - B\sin\theta\Big(\hat{S}_x\cos\omega_{\text{eff}}t - \hat{S}_y\sin\omega_{\text{eff}}t\Big)\big(\hat{I}_x\cos\omega_{0I}t + \hat{I}_y\sin\omega_{0I}t\big).\end{aligned} \tag{1.28}$$

Finally, we can calculate the first-order average Hamiltonian. We see that the sinusoidal terms will all average to zero if we choose a long time τ for the integration, i.e. $\tau \gg 2\pi/\omega_{\text{eff}}, 2\pi/\omega_{0I}$, except the terms on the third line of Equation (1.28) when $\omega_{\text{eff}} = \pm\omega_{0I}$. This is the *matching condition* for the solid effect, and taking the $\omega_{\text{eff}} = -\omega_{0I}$ case yields

$$\overline{\tilde{H}}^{(1)} = \frac{1}{\tau}\int_0^\tau \tilde{H}(t)\,\mathrm{d}t = A\cos\theta\hat{S}_z\hat{I}_z - \frac{B\sin\theta}{2}\Big(\hat{S}_x\hat{I}_x + \hat{S}_y\hat{I}_y\Big). \tag{1.29}$$

This matching condition is the "zero-quantum" (ZQ) condition owing to the $(\hat{S}_x\hat{I}_x + \hat{S}_y\hat{I}_y)$ term; choosing $\omega_{\text{eff}} = \omega_{0I}$ (in this case when we have assumed the electron and nucleus have opposite sign γ's) yields the double-quantum (DQ) condition containing $(\hat{S}_x\hat{I}_x - \hat{S}_y\hat{I}_y)$. By defining the initial density matrix $\rho(0) = \hat{S}_z$, tilting it by θ to $\rho'(0) = \hat{S}_z\cos\theta -$

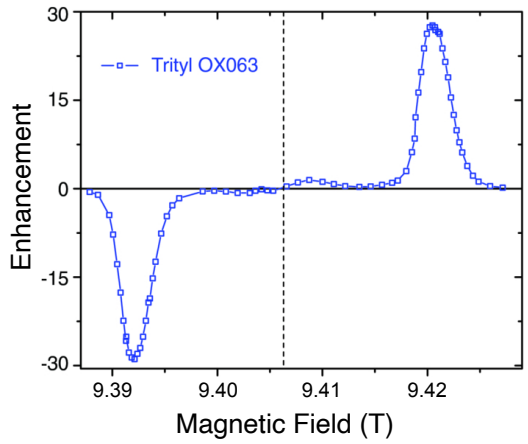

(a) Solid effect

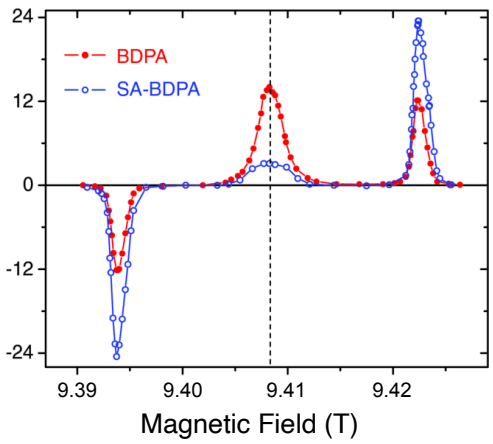

(b) Overhauser effect and solid effect

Figure 1.1: DNP enhancement profiles of narrow line radicals, exemplifying SE and OE DNP. Samples are (a) trityl-OX063 in glycerol-water and (b) BDPA in polystyrene, SA-BDPA in glycerol-water. Figures reproduced from [29].

$\hat{S}_x \sin\theta$ in our tilted frame, and then applying the propagator $U(t) = e^{-i\overline{\tilde{H}}t}$, we have

$$\begin{aligned}\rho'(t) = {} & \hat{S}_x \cos\theta\left(\frac{B\sin\theta}{4}t\right) - \hat{S}_x \sin\theta \cos\left(\frac{A\cos\theta}{2}t\right)\cos\left(\frac{B\sin\theta}{4}t\right) \\ & + \hat{I}_x \sin\theta \sin\left(\frac{A\cos\theta}{2}t\right)\sin\left(\frac{B\sin\theta}{4}t\right) + \hat{I}_z \cos\theta \sin^2\left(\frac{B\sin\theta}{4}t\right) \\ & + \text{bilinear terms}\ldots\end{aligned} \tag{1.30}$$

The frame of the I operators was not affected by our tilted frame, so we can easily identify the final components of the nuclear magnetization along $\hat{I}_x$ and $\hat{I}_z$. Moreover, we can state that in the limit of low-power microwave irradiation ($\omega_{1S} \to 0$), the only way to achieve the matching condition $\omega_{\text{eff}} = \pm\omega_{0I}$ is for $\Omega_S \approxeq \pm\omega_{0I}$. In this case, θ is near zero so the $\hat{I}_x$ term is small, and we can approximate the $\hat{I}_z$ component as

$$\langle I_z \rangle (t) = \frac{B^2\omega_{1S}^2}{16\omega_{0I}^2}t^2. \tag{1.31}$$

Taken together, the ZQ and DQ matching conditions lead to the characteristic enhancement profile for SE DNP (Figure 1.1a). Equation (1.31) is a simplification of the real-world

SE enhancement, as we have ignored such factors as relaxation and magic angle spinning, and also we only consider the polarization transfer to a single nearby nucleus. In DNP NMR we generally do not observe such nuclei directly, but rather observe an enhanced signal from the *bulk* nuclei (far from the electron) as polarization spreads via *spin diffusion* away from the initially polarized nuclei[30]. However, it does provide a key point of why the SE is not generally favored at high fields: the inverse square dependence on ω_{0I}, compounded by lower availability of high-power microwave sources at higher frequencies, so high ω_{1S} is also difficult to achieve.

The Overhauser effect, like the solid effect, involves a single electron-nucleus spin system. However, it also requires *cross-relaxation* between the electron and nucleus, which in turn would have to be due to a fluctuating hyperfine interaction. In that case, saturation of the electron spins with on-resonance irradiation leads to a dynamic equilibrium with the relaxation processes, and if the ZQ and DQ cross-relaxation rates differ, an effective transfer of polarization is achieved. In systems with high electron mobility (conductors and solutions), dynamics leading to a fluctuating hyperfine interaction and electron-nuclear cross-relaxation can reasonably be expected, but not in insulating solids typical of solid-state NMR. As such, the enhancement profiles of SA-BDPA and BDPA[29, 31], reproduced in Figure 1.1b, were both surprising and interesting. Moreover, the OE enhancement appeared to scale *favorably* with increasing external field, unlike the SE and CE enhancements, while also requiring minimal ω_{1S}. These properties make it appealing for use at high fields, but the OE in insulating has been observed only for a small set of polarizing agents (until recently[32], only for BDPA and derivatives thereof).

The cross effect requires an additional electron in the spin system. In particular, the Larmor frequencies of the two electrons must differ by the nuclear Larmor frequency, they must be coupled to one another, and at least one of them must be hyperfine-coupled to the nucleus in question. Then, saturation of one of the two electrons leads to a polarization difference between the two; polarization can then be transferred to

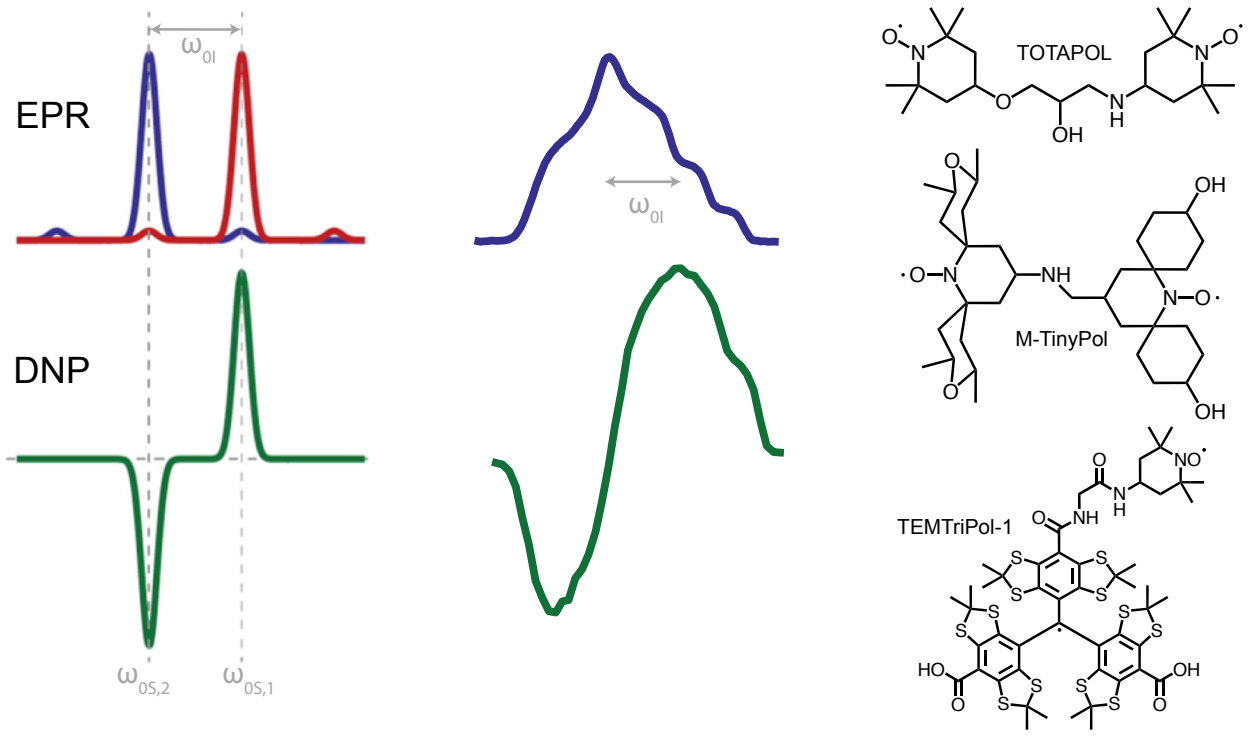

(a) A single e-e-n system. Reproduced from [33].

(b) TOTAPOL in glycerol-water. Adapted from [34].

(c) A sample of structures of CE biradicals.

Figure 1.2: Cross effect matching condition, a typical biradical field profile, and several biradicals which have been synthesized to further improve CE DNP at high fields. Biradicals in (c) are TOTAPOL[34], M-TinyPol[35], and TEMTriPol-1[36].

the nucleus in an energy-conserving three-spin flip. The resultant enhancement profile is shown in Figure 1.2a; in this case each electron has a single narrow peak in its EPR spectrum. In practice we employ radicals with broad g-tensors such as nitroxides for CE DNP. For a given molecular orientation, a nitroxide has a relatively narrow spectrum, so the CE matching condition $\omega_{0S,1} - \omega_{0S,2} = \pm\omega_{0I}$ will be satisfied for many different pairs of electrons in a solid sample. Moreover, biradical nitroxides have been employed to great effect for CE DNP: by ensuring that two unpaired electrons can always be found in close proximity, usually with a strong exchange coupling, we achieve larger DNP enhancements at lower radical concentration compared to monoradical nitroxides. The EPR spectrum and DNP enhancement profile of TOTAPOL, one of the first biradicals developed for DNP, are shown qualitatively in Figure 1.2b.

The CE mechanism scales less poorly with increasing field than the SE, and it also works well under MAS. These factors have made it the premier mechanism for high-field solid-state DNP, including most applications. It has also sparked intense interest in improving polarizing agents for high fields. Thanks to better understanding of the properties which make biradicals favorable for DNP[37, 38], new bisnitroxide radicals such as M-TinyPol[35], shown in Figure 1.2c have been prepared to optimize, e.g., the inter-electron coupling and relative g-tensor orientation. A further class of biradicals are those in which one of the radicals is a narrow-line radical such as trityl while the other is a nitroxide, such as TEMTriPol-1, also shown in Figure 1.2c. These facilitate saturation of one electron by including a radical with a narrow EPR lineshape and minimize the effect of depolarization under MAS. Depolarization is a consequence of the several level anti-crossing events which occur under MAS regardless of whether microwave irradiation is present[39–41]. Specifically, CE events which enable transfer of polarization to nuclei when a large electron polarization difference is present can also draw polarization from nuclei when the electron polarization difference is small. This occurs when bisnitroxide radicals are spun without microwave irradiation: at some points their g-tensors align in such a way that they have the same Larmor frequency. In this case the electrons can exchange polarization and equilibrate such that the polarization difference is zero.

Thermal mixing (TM) involves the same kind of energy-conserving three-spin flip as the cross effect, but it does not invoke the g-tensor anisotropy to lead to the $\omega_{0S,1} - \omega_{0S,2} = \pm\omega_{0I}$ condition. Rather, it requires a dense network of strongly dipolar coupled electrons such that the dipolar linewidth is on the order of the nuclear Larmor frequency. From there, it makes a thermodynamic argument which we can summarize briefly here[42]. There are three thermal reservoirs in the system due to the electron Zeeman interaction, the nuclear Zeeman interaction, and the electron-electron dipolar interaction, which start at thermal equilibrium with the lattice. Irradiation with microwaves near the electron Larmor frequency lowers the effective field experienced by

the electrons in the rotating frame, but their equilibrium polarization from the laboratory frame is mostly preserved, lowering the *spin temperature* of the Zeeman reservoir. The lower effective field also places the rotating frame Zeeman interaction strength on the order of the dipolar interaction, placing these two reservoirs in contact and thus cooling the dipolar reservoir. Finally, the dipolar reservoir is in contact with the nuclear Zeeman reservoir because, again, the dipolar linewidth is on the order of the nuclear Larmor frequency. TM is generally not considered in the context of high-field MAS DNP: since dipolar couplings are independent of field, the condition that they remain on the order of the nuclear Larmor frequency will not generally be met.

1.2.3 Pulsed DNP

Despite active development and many successful applications, CW DNP remains limited by decreasing enhancements at higher magnetic fields, with the possible exception of the Overhauser effect which is not yet well understood or widely applied. Pulsed DNP, by contrast, offers the possibility of field-independent enhancement. Unlike CW DNP, which involves weak microwave fields saturating electron spin transitions, pulsed DNP uses strong microwave pulses to generate electron spin coherences, which in turn lead to predictable and efficient polarization transfers to nuclei. Moreover, the intellectual space of time-domain experiments is vast, and we have decades of pulse sequence development in NMR and EPR to guide future endeavors. Tan et al. have written an excellent chapter summarizing progress in pulsed DNP as of 2019[43]. We will only briefly highlight some salient points.

Generally, pulsed DNP requires that one be able to generate electron spin coherences faster than they decay. That is, we require $\omega_{1S} \gg 2\pi/T_{2e}$, in contrast with the requirement for CW DNP that $\omega_{1S} \gg 2\pi/T_{1e}$ to achieve efficient saturation of the electron energy level transitions. The other major requirement is that one have sufficient control of the timing and phase of the microwave pulses. This latter requirement will

be the focus of Chapter 2 of this thesis.

One approach to pulsed DNP is to irradiate both the electron and the nucleus during the pulse sequence. This has been done in the Nuclear Rotating Frame (NRF-DNP)[44, 45] and the Dressed State Solid Effect (DSSE)[46] experiments. However, the resultant enhancements are small, likely because the nuclear magnetization relaxes too quickly when built up along the spin-lock axis.

The other approach, which has seen greater success, involves irradiation of only the electron spins. These build up longitudinal nuclear magnetization, allowing for efficient spin diffusion to the bulk as in CW DNP. The first such experiment is Nuclear Orientation via Electron Spin Locking (NOVEL)[47], which establishes an electron spin lock with Rabi frequency equal to the nuclear Larmor frequency. Obviously this is an increasingly demanding requirement at higher fields. However, the possibility of off-resonance NOVEL[48] relaxes this requirement somewhat, and was able to achieve 70% of the on-resonance NOVEL enhancement with only $\omega_{1S} = \omega_{0I}/3$, only $1/9$ of the microwave power requirement in terms of watts. Moreover, the authors offer insight into operation with intermediate microwave power available, between the low-power limit of the solid effect and the high-power limit of on-resonance NOVEL.

The integrated solid effect (ISE)[49, 50] achieves an adiabatic passage for the entire EPR line, resulting in polarization transfer. That is, by sweeping the effective field experienced by the electrons in the microwave rotating frame from strictly $+z$ to strictly $-z$, the electron magnetization remains coherent and parallel to the effective field. At some point during the sweep, for every electron spin, the SE matching condition $\omega_{\text{eff}} = \omega_{0I}$ is satisfied, enabling polarization transfer to hyperfine-coupled nuclei. The sweep must be adiabatic, which imposes requirements on the microwave power and the sweep rate. Henstra and colleagues originally performed the experiment by sweeping the magnetic field with fixed-frequency microwave irradiation[50]; more recent formulations of the experiment have employed frequency sweeps instead[51]. While performing frequency-

swept experiments on narrow-line radicals, an effect termed the "stretched" solid effect was observed when the sweep was not centered about the EPR resonance. This effect was also observed at higher field (3.35 T), where it actually resulted in higher enhancement than the ISE. Through further characterization[52] the adiabatic solid effect, involving very narrow sweeps directly about the SE conditions, was observed and also found to yield excellent enhancement, particularly with limited microwave power. Most recently, theory has been developed to unify these three effects[53] and was employed in conjunction with an upgraded and highly capable 3.35 T spectrometer to achieve unprecedented enhancement[54].

The last group of experiments is perhaps the one which most appeals to solid-state NMR spectroscopists: multiple-pulse sequences in the vein of Time-Optimized Pulsed DNP (TOP-DNP)[55], devised with techniques akin to those used to construct dipolar recoupling sequences. Proceeding from TOP-DNP have emerged XiX-DNP[56], BEAM-DNP[57], and TPPM-DNP[58]. The theoretical tool of choice for the design of these sequences has been operator-based triple-mode Floquet theory[59, 60], which is equipped to handle the many incommensurate frequencies involved (typically the microwave effective field, the nuclear Larmor frequency, and the periodicity of the sequence itself).

1.3 Microwave sources for DNP

From the preceding section we can devise a few properties of an ideal microwave source for DNP, then address the realities of sources available at higher fields.

1. It should have as high power as possible. A useful waypoint is that it should be capable of satisfying the NOVEL condition $\omega_{1S} = \omega_{0I}$ at its corresponding field.

2. It should have a spectrally pure output to be capable of precisely satisfying matching conditions based on microwave offset.

3. It should offer long term stability and ease of use, and not require significant funding or lab space.

4. For pulsed DNP, it should be capable of arbitrary control over the amplitude and phase of the output with extreme timing precision.

Here, it should be noted that the power requirement is dependent on the resonant structure, if present, used to generate a B_1 field at the sample. With sufficiently high Q factors, even a few milliwatts can achieve high ω_{1S}.

With these requirements in mind as axes of performance, we can discuss the two main categories of devices used in high-field ($B_0 \geq 5\,\mathrm{T}$, $\omega_{0S} \geq 140\,\mathrm{MHz}$) solid-state DNP: gyrotrons and solid-state (semiconductor-based) sources.

1.3.1 Gyrotrons

Gyrotrons are a type of vacuum electronic device, which generate microwaves via interaction between an electron beam and an electromagnetic mode of an interaction cavity. Since their initial introduction to high field DNP[61], they have seen continued proliferation and even commercialization[62]. Their success is primarily thanks to their high, stable output power. Indeed, gyrotrons which output megawatts of power suitable for heating of plasma for fusion experiments have been constructed. For DNP, we routinely use gyrotrons outputting up to about 100 W; much higher might lead to undesirable amounts of sample heating.

Gyrotrons do have some shortcomings with respect to an ideal microwave source. One major issue is that they require their own superconducting magnet with field strength approximately equal to that of the NMR magnet (or half that field, for second-harmonic operation). This is an expensive initial investment, and also requires space for sufficient separation between the two magnets, and several meters of corrugated waveguide to transmit the microwaves across the room. And in terms of capabilities, gyrotrons

are generally limited to continuous-wave, fixed-frequency operation, though frequency-agile gyrotrons have also been developed[63, 64] with an eye towards time-domain DNP.

1.3.2 Solid-state sources

For high field DNP, Schottky diode-based sources, which exploit nonlinear capacitance to multiply an input signal to a higher frequency, have emerged as possible alternatives to gyrotrons[65, 66]. Coupled with lower frequency devices, these Amplifier Multiplier Chains (AMCs) offer much lower power than gyrotrons, but in exchange are extremely compact and require essentially no additional infrastructure. Most excitingly, they integrate well with pulse generators and frequency mixers for arbitrary control capabilities. They have been used for static EPR and DNP where a resonant cavity could be used, including in our lab[67, 68]; our 140 GHz cavity allows $\omega_{1S}/2\pi = 5$ MHz with only 100 mW from the AMC.

1.3.3 Amplifiers

Perhaps the best prospect for an ideal microwave source is a combination of a solid-state source with a high power amplifier, much like we use for RF pulses in NMR. The development of amplifiers at frequencies relevant to high field DNP is an area of ongoing research. Gyro-amplifiers, with operating principles similar to those of gyrotron oscillators, have been developed at 140 GHz[69] and 250 GHz[70], capable of outputting hundreds of watts. Another option is a traveling wave tube amplifier (TWTA); amplifiers operating around 233 GHz for military use have been reported[71–73] and could potentially be adapted for DNP.

Chapter 2

An Arbitrary Waveform 250 GHz Microwave Source

With the development of a 250 GHz gyro-amplifier at MIT and the verification of pulsed DNP sequences, we were interested in constructing a pulsed MAS DNP instrument operating at 250 GHz. The plan was to construct a solid-state source to serve as a driver for the amplifier. This chapter describes the construction and characterization of that solid-state source. We were also pleasantly surprised at how effective the source was for CW DNP, particularly for acquiring frequency profiles facilitating the investigations of CW mechanisms. *The majority of the remainder of this chapter has been published in "Frequency-swept dynamic nuclear polarization" by Mardini and Palani et al.[74].*

2.1 Introduction

We have discussed the potential benefits of employing pulsed DNP at high fields (Section 1.2.3), namely the possibility of field independent benefits in contrast to the unfavorable scaling of the solid effect (SE) and cross effect (CE). With regard to the capability of modulating the frequency, amplitude, and phase of microwave irradiation, a prerequisite for pulsed DNP, a suitable microwave source must be capable of outputting pulses

as short as a few ns, with amplitude and phase modulation occurring even faster.

Frequency-agile gyrotrons have shown that they can alter the microwave frequency by up to 20 MHz per µs and achieve a pseudo-gating ability by quickly shifting the microwave frequency on- and off-resonance[63, 64]. However, pulsed DNP sequences that generate and manipulate electron spin coherences, such as TOP-DNP[55], XiX-[56] and TPPM-DNP[58], and BEAM-DNP[57], operate on the timescale of ns, too fast for the current generation of gyrotron oscillators but perhaps within reach with further innovations. Besides gyrotron sources, solid-state microwave sources have recently emerged as attractive options for frequency, amplitude, and phase modulations while also being cost- and space-efficient. They consist of frequency multiplier diodes to take advantage of mixers, amplifiers, and filters readily available at lower frequencies to achieve complete amplitude and phase modulation. Incorporating arbitrary waveform generation leads to the most flexible microwave sources for pulsed DNP applications. An arbitrary waveform-modulated microwave source for EPR and DNP applications was demonstrated at 5 T[68, 75, 76] and more recently at 7 T[77–79]. Kuzhelev and Akhmetzyanov et al. showed the advantage of arbitrarily-shaped, broadband pulses for PELDOR measurements in EPR[80]. Sergeyev et al. demonstrated a 263 GHz solid-state diode source for MAS DNP application[66], but without arbitrary waveform capabilities.

Finally, in developing new and improving established DNP methods, it is important to be able to record the Zeeman field profiles to discern and disentangle the dominant DNP mechanism. Historically, this has required a magnet equipped with a sweep coil to vary the main magnetic field B_0. The sweep process is tedious, requiring that the probe be retuned as the NMR frequency changes, data is usually low resolution for that same reason. This process also increases the rate of helium boiloff, increasingly relevant as helium becomes scarce and expensive. In the worst case, an improperly conducted field sweep can lead to a magnet quench. Using an arbitrary waveform generator (AWG) to independently perform frequency sweeps over any range up to several GHz circumvents

these issues: the sweeps require essentially no supervision or retuning of the probe, and pose no danger to the magnet. All told, these reasons provided ample rationale for developing an AWG-based microwave frequency sweep system for DNP at high fields.

We report here the implementation of frequency-swept AWG-equipped solid-state source for DNP experiments at 250 GHz (9 T). We attain a frequency range of ∼8 GHz centered at 250 GHz with microwave output power of 160 mW, and demonstrate the observation of all contemporary high-field CW DNP mechanisms – the Overhauser effect (OE)[23, 24, 29, 81, 82], the solid effect (SE)[83–85], the cross effect (CE)[86–91], and the recently described mechanism of resonant mixing (RM)[92, 93] (Chapter 4). With this modest power, the generated Rabi field B_1 is insufficient to fully realize the usefulness of frequency chirps with MAS probes, though we do observe a modest improvement over monochromatic irradiation in a mixed radical system. Among CW DNP mechanisms, we observe the best performance with the Overhauser effect, and have used the microwave source to investigate the nuclear polarization transfer pathway in BDPA radicals in ortho-terphenyl matrix[81, 82] (Chapter 3). Here, we demonstrate the OE with a recently reported water-soluble BDPA as a promising means for DNP studies of biological macromolecules without requiring an expensive high-power gyrotron.

The reported instrumental advances are important steps towards realizing pulsed DNP at magnetic fields of 9 T and above. The AWG enables any conceivable pulsed DNP sequence with a time resolution of $<$100 ps, including the repeated pulse architecture of TOP-DNP and XiX-DNP. Beyond rectangular pulses, there exists the possibility of shaped pulses to achieve desired excitation patterns – our ability to manipulate electron spins is approaching that of dedicated EPR spectroscopy. The next steps include increasing the generated B_1 by augmenting the spectrometer with a microwave amplifier and/or a more efficiently coupled sample chamber.

2.2 Initial construction

Developments in diode technology enabled frequency doubling diodes which would handle increased input power from a high-power amplifier at 60 GHz; in collaboration with Virginia Diodes, Inc. (VDI) we proposed the construction of a microwave source for DNP which would use these new diodes. In their initial configuration, VDI provided us a relatively standard system architecture: we would provide an input signal at ~10.4 GHz, and that signal would be multiplied a total of 24×, including the final two doubling diodes to reach 250 GHz. As such, our initial design for the AWG integration had mixing occur with a local oscillator (LO) around 10 GHz and using a relatively low intermediate frequency (IF) from the AWG, as shown in Figure 2.1(D).

As part of our initial testing, we examined frequency profiles for a BDPA/OTP sample (1,3-bisdiphenylene-2-phenylallyl in ortho-terphenyl) and observed abnormally broad and weak SE matching conditions, which differed from our observations when omitting the AWG and only adjusting the LO (Figure 2.2). Evidently, our mixing arrangement was flawed in some way, especially considering the problem seemed only to manifest away from the center of the output range, when the AMC frequency was large. We subsequently measured the power output of the AMC at different AWG frequencies and saw no difference, leading us to analyze the frequency content of the output. Frequency measurements at 250 GHz were made using a 12th-harmonic mixer arrangement, with a LO at about 20.8 GHz mixing with the AMC output to generate a signal around 400 MHz which we could readily amplify and characterize with a spectrum analyzer. Frequency measurements at 10.4 and 31.2 GHz only needed an appropriate LO (10 and 27 GHz, respectively) and double-balanced mixer to bring the signal within the bandwidth of the spectrum analyzer.

Results of the analysis are shown in Figure 2.1(A)–(C). We found that despite a relatively clean input signal, where undesired frequencies were suppresed by ~30 dB rela-

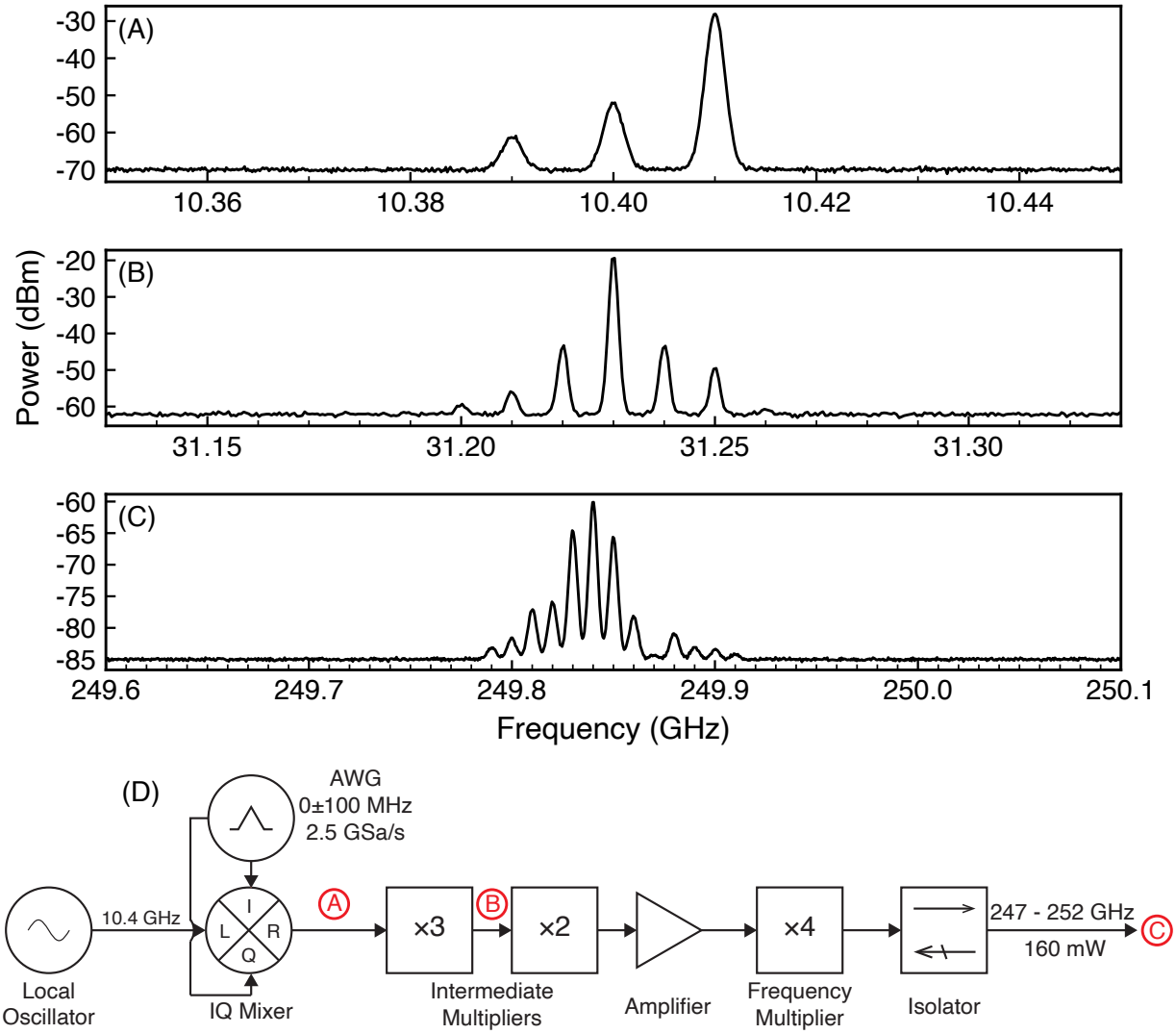

Figure 2.1: Characterization of the initial, ultimately rejected, design of the AWG-AMC solid-state microwave source. (A)–(C): representative frequency measurements made at the corresponding points shown in the circuit diagram in (D), with the LO set to 10.4 GHz and the AWG outputting +10 MHz, for a nominal final frequency of 249.84 GHz. Plotted spectra are approximate reconstructions of the spectrum analyzer output onto the absolute frequency domain; powers can be assessed within a plot but not between plots as the downconversion schemes for each frequency differ significantly. (A): output from the IQ mixer shows the desired signal at 10.41 MHz and the suppressed opposite sideband and leakage of the LO. (B): output following a single tripler step. (C): dense comb of sidebands at the final output. (D): schematic of source configuration for these measurements.

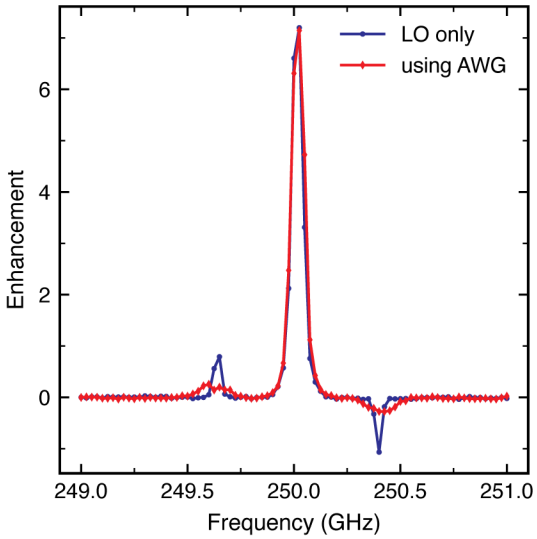

Figure 2.2: Initial DNP frequency profiles of BDPA/OTP collected using either the AWG (red) to vary the frequency for a fixed LO or using the LO alone (blue).

tive to the desired one (Figure 2.1(A)), the output signal was a comb of frequencies (sidebands) centered about the desired frequency, comparable to the desired frequency in amplitude and spaced by the AWG frequency (Figure 2.1(C)). We then saw that the sidebands were related to the multiplication process, with an intermediate density of sidebands observed after the first tripler stage (Figure 2.1(B)). The result is understood by considering that the multipliers also act as mixers when multiple tones are present in the input signal. Thus, the amplitude of an undesired sideband relative to the primary frequency is increased by a factor of $20 \cdot \log N$ dB during a multiplication step with multiplication factor N, the same as the fundamental increase in phase noise with frequency multiplication. As such, even though our sidebands were well-suppressed at 10 GHz, they became prominent following multiplication by $N = 24$. As an initial solution, we were able to further improve the sideband suppression in Figure 2.1(A) by fine-tuning the AWG output to compensate for phase and amplitude imbalances between the I and Q channels of the AWG and mixer. However, we found the corrections highly frequency dependent, rendering them unsuitable for routine implementation. Our only option, then, was to change the mixing scheme.

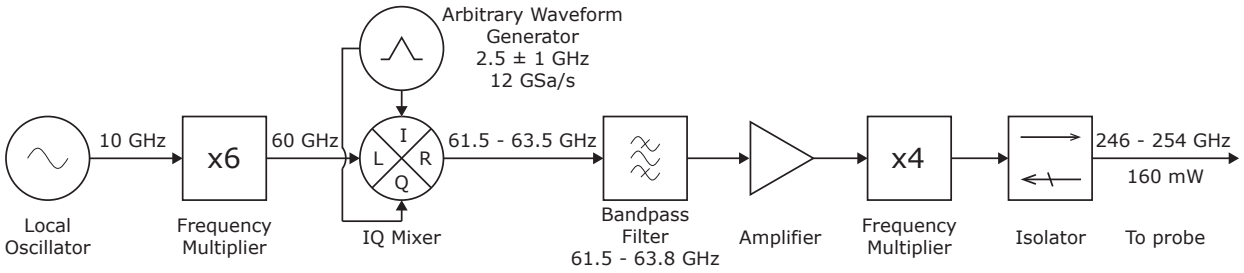

Figure 2.3: The circuit used to generate microwaves at 250 GHz. A 10 GHz signal from an oscillator is fed into a series of multipliers to reach 60 GHz; that output is mixed at an IQ mixer with signals from an arbitrary waveform generating operating between 1.5 and 3.5 GHz. The upper sideband of mixer output, between 61.5 and 63.5 GHz is filtered before being input to a high-power amplifier, which brings the output power to 3 W prior to the final pair frequency doubling diodes, ultimately outputting a frequency between 246 and 254 GHz with a power of 220 mW. To protect the multipliers from reflected power, a directional isolator is used as well; the insertion loss of −1.4 dB lowers the final output power to 160 mW.

In our revised design, shown in Figure 2.3, we address the sideband problem in two ways. First, we use a much higher AWG frequency to ensure that any sidebands after mixing are far away (cf. Figure 2.1(A)) and also use a bandpass filter to remove those sidebands, if present, ultimately providing the multipliers as clean an input as possible. Second, we perform the mixing at a higher frequency so that the multiplication factor after mixing is as low as possible; a high-frequency IQ mixer operating around 60 GHz was available off-the-shelf and easily incorporated into our system. These changes appeared to resolve our issues: subsequent measurements of the 250 GHz output now yield only a single tone.

2.3 Results and discussion

2.3.1 Frequency stability and related measurements

With the system established, we compared its frequency stability to that of our 250 GHz gyrotron (Figure 2.4). The AMC output frequency had a standard deviation of about 60 kHz, while that of the gyrotron was about 1.6 MHz, an order of magnitude larger. That

the AMC output frequency is more stable is expected: its frequency stability is tied to the stability of the 10 GHz phase-locked loop LO, while that of the gyrotron depends on fluctuations in the beam voltage and current, among other factors[94, 95]. For most applications, including routine DNP, the slight fluctuations of the gyrotron frequency are not critical, but for precise DNP and EPR measurements, the additional stability of the AMC may be essential.

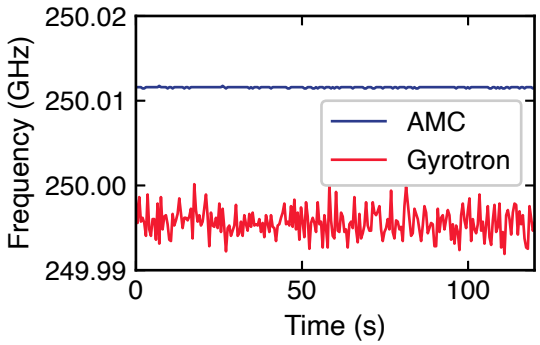

Figure 2.4: Frequency stability measurements of the two sources near 250 GHz. Measurements were made using a harmonic downconversion and the FFT function of a digital oscilloscope. The scope's sampling rate was 5.0 GS/s and each trace 50 kS (10 µs acquisition time); each plotted point corresponds to the frequency of maximum intensity for a particular trace, and two traces were acquired per second.

We made similar frequency measurements for the AMC source outputting frequency chirps and observed approximately the expected distribution of frequencies (Figure 2.5). We attribute the observation of sidebands to the time-domain acquisition of the oscilloscope as the sideband spacing is determined by the chirp repetition frequency (1 MHz for 1 µs, 100 kHz for 10 µs).

Finally, we attempted a "multitone" signal in which the AWG output would contain two equally intense frequencies which, if each were multiplied individually and then summed, would lead to an output signal with two frequencies which could be used to simultaneously irradiate different parts of the EPR spectrum, as in an ELDOR experiment, or to satisfy different DNP conditions. Perhaps as expected from our observations with the lower frequency AWG (Figures 2.1 and 2.2) the existence of two tones in

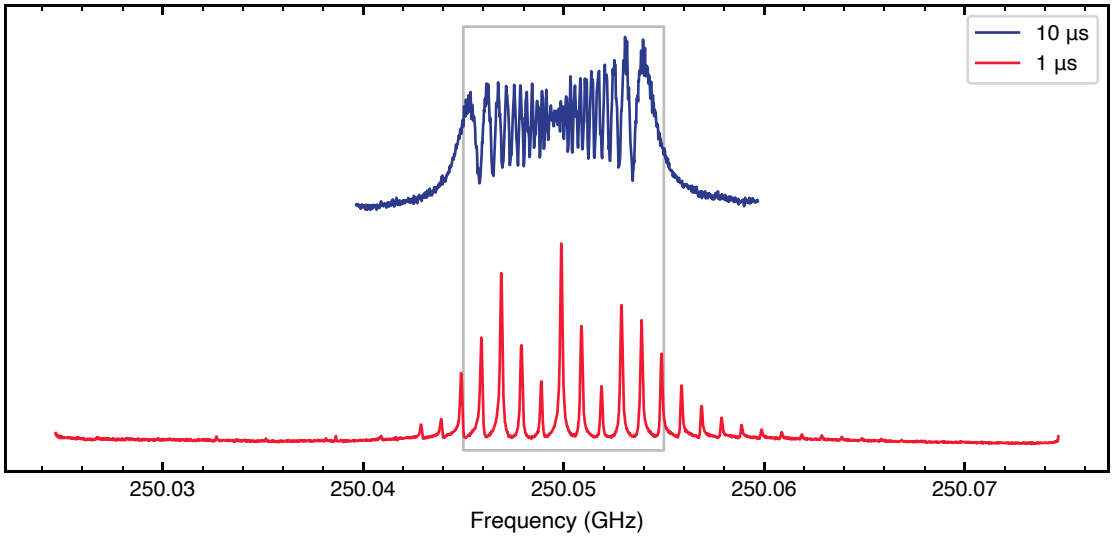

Figure 2.5: Measurements of the AMC output frequency during microwave chirping over 250.05 GHz ± 5 MHz. Traces are envelopes of the observed signals after approximately repeated acquisitions, about 1 minute real time. Gray box represents the nominal chirp range.

the input signal led to an output signal which mixed the two and proliferated sidebands. For example, when we attempted to simultaneously output 250.0 and 250.1 GHz tones (Figure 2.6, bottom trace), we observed primarily a single tone at 250.05 GHz and small sidebands with 25 MHz spacing, matching 1/4 of the 100 MHz nominal difference, i.e., the difference between the frequencies out of the AWG, prior to the ×4 multiplication. Confirming this, we repeated the measurement outputting 250.025 and 250.075 GHz tones simultaneously (Figure 2.6, top trace), and we again observed a primary signal at 250.05 GHz, but now sidebands were present at 12.5 MHz, again corresponding to 1/4 of the 50 MHz frequency difference. A system such as ours would need an independent second microwave source to simultaneously output two discrete frequencies.

2.3.2 Continuous-wave DNP frequency profiles

We have routinely used the system as a continuous-wave microwave source. Some characteristic results on DNP test samples are shown in Figure 2.7, demonstrating several CW

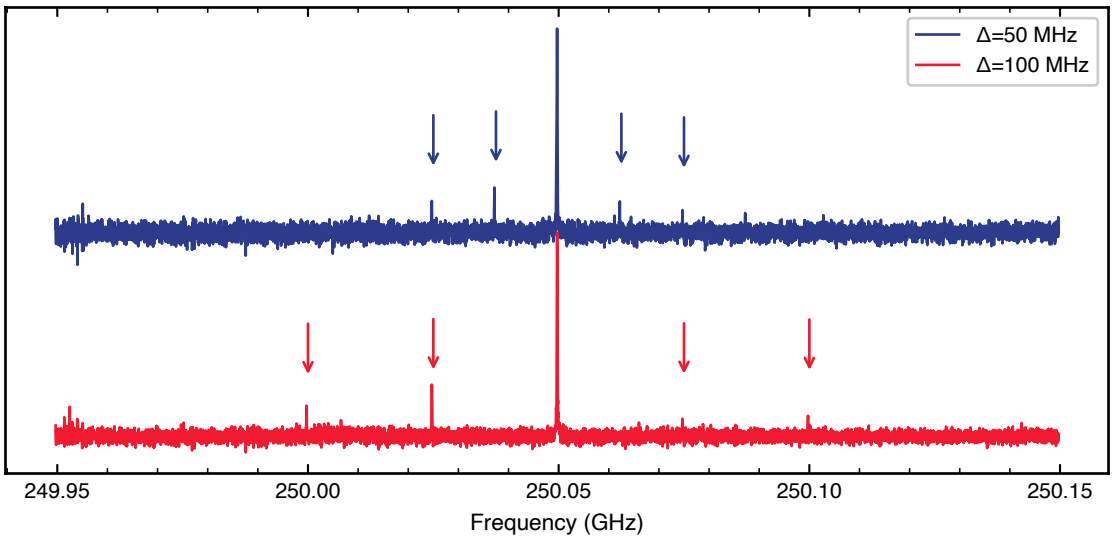

Figure 2.6: Attempted generation of multiple simultaneous tones using the AWG-AMC, with frequencies 250.05 GHz $\pm$ $\Delta/2$. Arrows indicate sideband spacings of $\Delta/4$.

DNP mechanisms: the cross effect with AMUPol[96], the solid effect and Overhauser effect with BDPA[29, 81, 82] (Chapter 3), the resonant mixing effect[92, 93] (Chapter 4) or debatably thermal mixing effect with trityl[97], and the ^{13}C enhancement profile of diamond powder containing P1 centers, which has been reported to include several overlapping mechanisms[98].

One unexpected result was the emergence of fine, ripple-like features in the AMUPol profile (Figure 2.7(A)). A previous study with a solid-state diode source also showed some fine features when compared to a field profile with a gyrotron source[66], and we likely have somewhat lower power than that study, exacerbating the effect. One might also suspect that the effect is an instrumental artifact, e.g. standing waves on the waveguide. We believe this not to be the case as no such ripples are observed in any of the other profiles in Figure 2.7. Further experiments are underway to determine the physical origin of these ripples, but are beyond the scope of this thesis.

At 9 T, the frequency range needed to explore all these mechanisms spans $\sim$1.5 GHz (with constant output power over that range). With a conventional gyrotron, one would fix the frequency and power of the gyrotron and sweep the NMR magnetic field, which

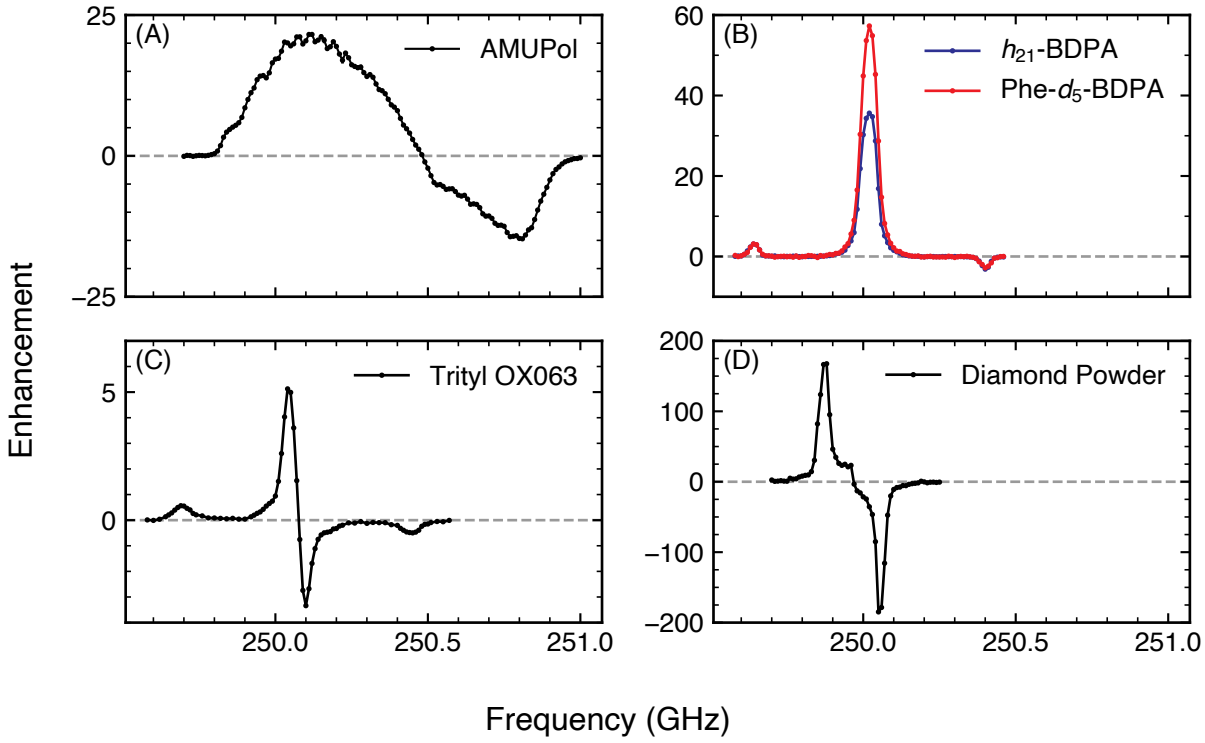

Figure 2.7: ^{1}H DNP (A–C) and ^{13}C DNP (D) frequency profiles obtained with the solid-state microwave source for polarizing agents (A) AMUPOL in 6:3:1 glycerol-d_8:D_2O:H_2O exhibiting CE DNP, (B) h_{21}-BDPA and Phe-d_5-BDPA in OTP matrix exhibiting OE and SE DNP, (C) Trityl-OX063 in 6:3:1 DMSO-d_6:D_2O:H_2O exhibiting SE and arguably resonant mixing (RM), and (D) diamond powder containing P1 centers primarily exhibiting CE DNP to natural abundance ^{13}C nuclei. Profiles in (A)–(C) were collected under MAS (5 to 7 kHz) at 90 to 100 K, and (D) under static conditions at room temperature. Specific sample details are elaborated in Section 2.4, and DNP experimental conditions in Table 2.1.

is a tedious process, expensive both in time and excess helium boiloff. A gyrotron can be designed to be tunable over several GHz[99], but in our experience hysteresis effects make it so the frequency and power must be constantly monitored to guarantee an accurate profile. With the AWG, frequency adjustment is instantaneous and repeatable, making it easily automated and allowing entire profiles to collect largely unattended. As a result, while the absolute enhancements with only 160 mW of microwave power are modest compared to those with several watts from a gyrotron, the ease of collecting these profiles has made it practical to investigate these CW mechanisms in detail.

2.3.3 Frequency-chirped irradiation

To take advantage of our ability to modulate the microwave output, we compared the fixed-frequency enhancements in Figure 2.7 to those using a frequency chirp. In most cases, our limited output power made the chirp no better than a single frequency. However, we did observe a slight improvement in CE enhancement for a mixed radical system[89] of 30 mM 4-amino TEMPO and 15 mM trityl-OX063 as Han and colleagues reported previously[79]. This system is favorable for observing the benefit of chirped irradiation: the narrow-line trityl is more efficiently saturated by chirping the microwave frequency across the EPR line at a rate faster than the MAS frequency.

The resultant CE enhancement, which depends on the polarization difference between the narrow-line trityl and wide-line nitroxide, concomitantly increases. In Figure 2.8 we report a maximum relative increase of about 13%, resulting in an absolute enhancement of 9.0 when using a chirp width of 30 MHz and a chirp time of 1 µs. We expect that with higher available ω_{1S}, from increased incident microwave power and/or improved coupling efficiency, chirped DNP will outperform single-frequency irradiation under a broader range of conditions. We justify this expectation with the theoretical understanding of the cross effect under MAS as distinct events in a rotor period[39]. Microwave irradiation is involved in electron-microwave events, which are avoided level

crossings when the microwave frequency matches the electron Larmor frequency that result in saturation of the electron spin. The efficiency of saturation during the event, which leads to polarization difference between electrons and eventual nuclear enhancement, is governed by the adiabaticity probability,

$$P_{\mathrm{EM}} \approx \pi \omega_{1\mathrm{S}}^2 / \left(2 \frac{\partial |\omega_{\mathrm{e}}|}{\partial t} \right), \tag{2.1}$$

where ω_{e} is the instantaneous microwave offset which will be due to both the g-tensor anisotropy under MAS and the chirp rate of the microwave irradiation. Equation (2.1) suggests the importance of high $\omega_{1\mathrm{S}}$, especially at high chirp rates. We expect chirped irradiation will also prove useful for mixed biradicals which essentially aim to improve on this radical mixture, such as TEMTriPol[36].

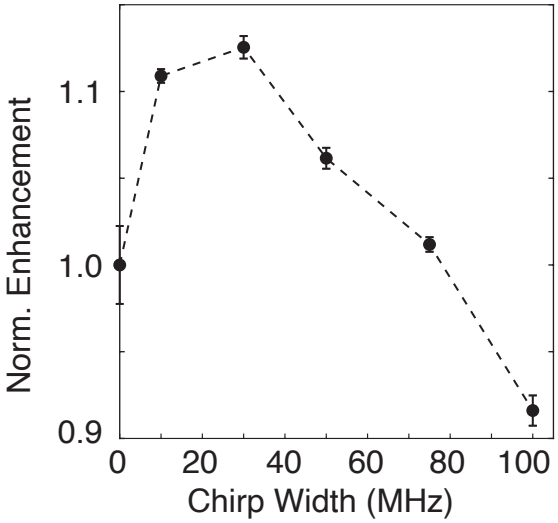

Figure 2.8: Relative performance of repeated 1 µs chirps of varying chirp widths for a sample of 30 mM 4-amino TEMPO and 15 mM in 6:3:1 glycerol-d_6:D_2O:H_2O. For all experiments, the MAS frequency was 5 kHz and the sample temperature 100 K.

2.3.4 Applications for Overhauser DNP

With the current instrumentation, we looked to Overhauser effect (OE) DNP as an application which does not require high microwave power. We have previously reported

large OE enhancements ($\varepsilon \sim 70$) with the AMC microwave source, but these employed BDPA in the organic matrix ortho-terphenyl (OTP)[81, 82]. A water-soluble BDPA is desirable for OE DNP in aqueous samples, including biological systems. A recently reported water-soluble derivative of BDPA[48] aimed to mitigate stability issues of previous water-soluble BDPAs[49,50]. With this NMe_3-BDPA, we observed bulk enhancements of ~25 in a degassed sample (Figure 2.9(A)).

We subsequently prepared a sample of microcrystals of the fibril-forming peptide fragment GNNQQNY doped with NMe_3-BDPA and observed a relayed enhancement[100] of ~4.2 (Figure 2.9(B)). Further optimizations may make NMe_3-BDPA an appealing polarizing agent, particularly for solid-state diode sources at high fields, considering the favorable scaling of the OE with increased magnetic field[29] and the low required microwave power.

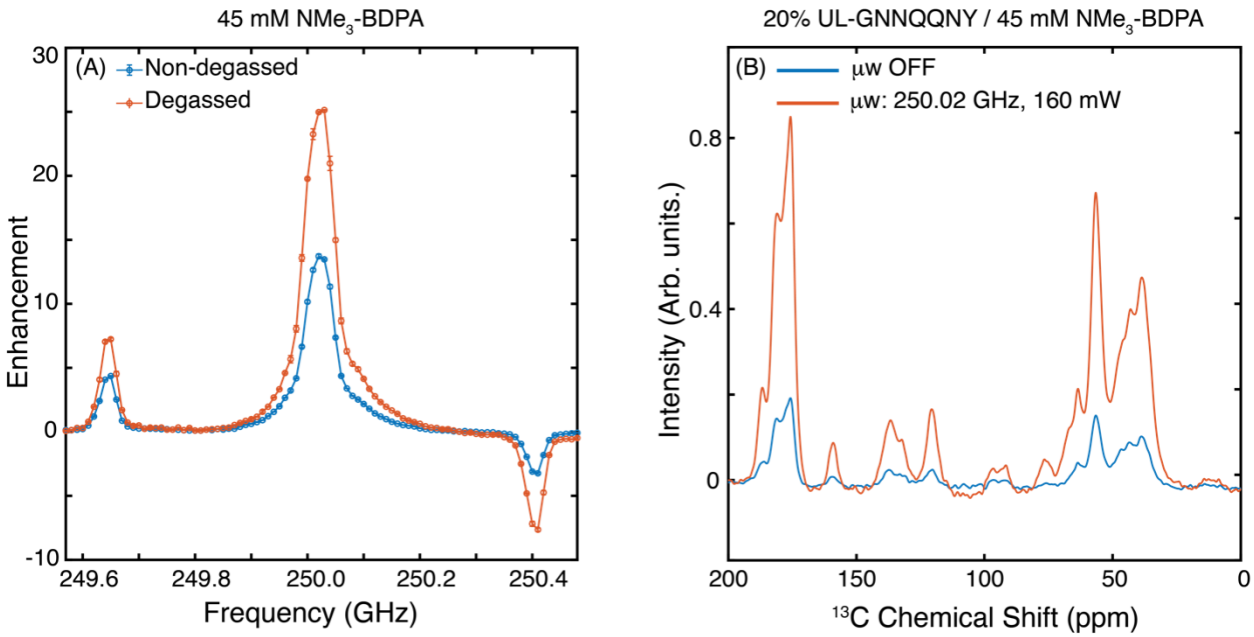

Figure 2.9: Results using the AWG driven solid-state source in conjunction with water-soluble NMe_3-BDPA. (A): Bulk ^1H enhancement for 45 mM NMe_3-BDPA in 6:3:1 glycerol-d_8:D_2O:H_2O at 95 K and spinning at 6 kHz, demonstrating the effect of freeze-pump-thaw degassing. (B): ^{13}C CP spectra of uniformly labeled GNNQQNY microcrystals wet with a small volume of the same 45 mM NMe_3-BDPA at 95 K and spinning at 7 kHz.

2.4 Materials and methods

In this section we describe sample preparation protocols for all samples in this chapter and give experimental details for DNP-NMR spectra in Table 2.1.

Sample	T (K)	$\omega_r/2\pi$ (kHz)	T_B (s)	NMR Sequence
AMUPol	90	6.0	10	^{1}H-saturation, {^{1}H}^{13}C-CP, 83 kHz TPPM decoupling during acquisition
BDPA BDPA-d_5	90	5.0	180	^{1}H-saturation, ^{1}H solid echo
Trityl-OX063	100	7.0	20	^{1}H-saturation, ^{1}H solid echo
Diamond	298	0	750	^{13}C-saturation, ^{13}C 90-acquire
Trityl/TEMPO	100	5.0	10	^{1}H-saturation, ^{1}H 90-acquire
NMe_3-BDPA	95	6.0	60	^{1}H-saturation, ^{1}H 90-acquire
GNNQQNY	95	7.0	30	^{1}H-saturation, {^{1}H}^{13}C-CP, 83 kHz TPPM decoupling during acquisition

Table 2.1: Details of DNP-NMR experiments.

AMUPol sample (Figure 2.7(A)): AMUPol and ^{13}C-urea were dissolved in 6:3:1 (vol.) glycerol-d_8:D_2O:H_2O to yield 10 mM and 1 M concentrations, respectively, and the solution pipetted into a 4 mm sapphire rotor. The mixed radical sample (Figure 2.8) was prepared similarly to yield 15 mM trityl-OX063 and 30 mM 4-amino TEMPO, as was the water-soluble 45 mM NMe_3-BDPA (Figure 2.9(A)); none of these latter samples contained ^{13}C-urea.

BDPA and Phe-d_5-BDPA in ortho-terphenyl (OTP) samples (Figure 2.7(B)) were prepared as described in [81]: a mixture of 95:5 mol. % OTP-d_{14}/OTP was doped with 2.5 wt. % of the radical, dissolved in $CDCl_3$, the chloroform allowed to evaporate yielding a thin film, and the film finely ground and packed into a 4 mm rotor as a powder. To ensure the formation of a glassy matrix, the samples were warmed to 60 °C for 5 min and then quenched in liquid nitrogen until just before insertion into the probe.

The trityl-OX063 sample (Figure 2.7(C)) was prepared as a 100 mM solution in 6:3:1 (vol.) DMSO-d_6:D_2O:H_2O; the high concentration is needed to observe a prominent cen-

tral feature in the enhancement profile.

The diamond powder sample (Figure 2.7(D)) was acquired from Element Six; it is type Ib and prepared by high pressure, high temperature (HPHT) synthesis, then ground to a powder of particle size 15 to 25 µm. The powder was packed as-is into a 4 mm rotor.

The degassing procedure[1] for the NMe_3-BDPA sample (Figure 2.9(A)) included the following additional steps: the solution was first prepared in a 5 mL pear-shaped flask and put through five cycles of freeze-pump-thaw degassing, at which point minimal bubbling was observed. The flask was sealed and moved to a nitrogen glovebox to transfer the solution to the 4 mm rotor. The rotor was kept frozen in liquid nitrogen until just before insertion into the probe.

The GNNQQNY sample (Figure 2.9(B)) was prepared by taking ~20 mg of nanocrystals of 20% uniformly ^{13}C,^{15}N-labeled GNNQQNY, prepared as described previously[100], washing the crystals several times with D_2O, then pipetting off as much D_2O as possible before wetting the crystals with a small amount of the degassed 45 mM NMe_3-BDPA solution in the nitrogen glovebox. The resulting mixture was scooped into a 4 mm rotor and again kept frozen in liquid nitrogen until use.

2.5 Conclusions

This chapter has documented a solid-state 250 GHz microwave source capable of arbitrary phase, frequency, and amplitude waveform modulation that will be essential for high-field pulsed DNP. We have highlighted some of our considerations in constructing the system, hopefully benefitting DNP spectroscopists planning to assemble similar instruments. We also report a selection of results which remain notable despite the low ω_{1S} available. In particular, we showed that CW frequency profiles could easily and efficiently be recorded, of which we make extensive use in the work described in Chap-

[1] More recently, we have found that using gas-permeable tubing made of materials such as fluorinated ethylene propylene in an oxygen-free atmosphere makes for a more straightforward degassing process.

ters 3 and 4. We have also shown early indications of the benefits of frequency-chirped irradiation and the prospects for using similar lower power sources in conjunction with water-soluble OE polarizing agents for high-field investigations of biological systems.

At present, this system is not able to achieve enhancement comparable to that using a gyrotron, but one can achieve increased ω_{1S} while maintaining the arbitrary modulation in two ways: 1) a secondary amplification step, and 2) improved efficiency of Rabi field generation in MAS stators. For amplifiers, both gyroamplifiers[70] and more compact slow-wave devices such as traveling wave tubes (TWTs) and klystrons offer the potential of 100 to 1000 W output pulses amplified from our 160 mW input source. Ongoing research in the field should soon make these amplifiers available at frequencies relevant to high-field DNP. Regarding stator efficiency, the model of pulsed EPR spectrometers is a relevant waypoint for the potential of resonant cavities: a TE_{011} resonator can achieve efficiencies of $\sim$35 MHz/$\sqrt{\text{W}}$[101], so only 20 mW incident microwave power would achieve $\omega_{1S}/2\pi = 5$ MHz for pulsed DNP, and our system could be used as-is for pulsed DNP in such a resonator. As for MAS, typical 3.2 mm MAS stators are estimated to achieve a microwave efficiency of $\sim$0.56 MHz/$\sqrt{\text{W}}$[66], requiring 80 W for the same electron B_1. A smaller rotor size and optimized design achieved 1.8 MHz/$\sqrt{\text{W}}$[66], which would require only 8 W for pulsed DNP. It seems inevitable that a combination of microwave amplifiers and improved microwave coupling will lead to high-field pulsed DNP under MAS.

Chapter 3

Investigations of Overhauser DNP

Since the observation that the Overhauser effect (OE) could be observed in insulating solids and particularly that the enhancement *increased* with increasing magnetic field[29], there has been considerable interest in OE DNP as a viable alternative to the cross effect (CE) with biradicals at high fields. Emsley and colleagues have also investigated the field dependence and corroborated these findings along with observing enhancements at relatively high temperatures[102] and, again encouragingly, finding that OE enhancement increases with MAS frequency[103].

While the OE has favorable properties for high field DNP, it is still the case that CE DNP with biradicals remains generally more efficient, particularly in terms of time savings thanks to allowing much shorter recycle delays. However, the radicals employed for CE DNP are carefully synthesized for that purpose, based on years of iteration and theoretical understanding of the relationship between molecular structure, EPR properties, and CE performance. Meanwhile, for OE DNP in solids, almost all studies to date have employed 1,3-bisdiphenylene-2-phenylallyl (BDPA) or variants thereof, where the effect was observed unexpectedly. To enable the same type of radical design and iteration for OE DNP, a greater understanding of the properties of BDPA which make it favorable is required. In this chapter, I start with an overview of our understanding of the OE in solu-

tion, which will provide a framework for the remainder of the chapter, a series of projects aiming to contribute to our understanding of the OE in solids. *Some of the content of this chapter has been published in "Overhauser dynamic nuclear polarization with selectively deuterated BDPA radicals" by Delage-Laurin, Palani, and Golota et al.[81] and "Amplified Overhauser DNP with selective deuteration: Attenuation of double-quantum cross-relaxation" by Palani and Mardini et al.[82].*

3.1 Introduction

In Section 1.2.2, we characterized the OE as due to the presence of zero-quantum (ZQ) and/or double-quantum (DQ) cross-relaxation between an electron and nucleus. In Figure 3.1, the four electron-nuclear spin states are depicted along with the corresponding transitions between them.

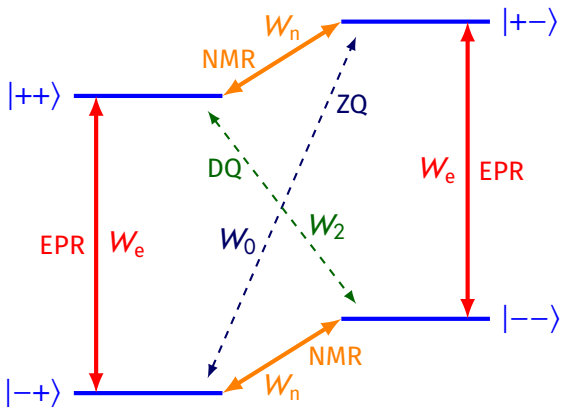

Figure 3.1: Description of OE DNP via Zeeman energy levels in an electron-nucleus system (states are labeled in the order $|SI\rangle$).

From this diagram, one can follow the procedure of Solomon[104] and a set of differential equations for the occupation numbers of the four states $|SI\rangle$ can be written

as,

$$\frac{\mathrm{d}}{\mathrm{d}t}\begin{pmatrix} N_{++} \\ N_{+-} \\ N_{-+} \\ N_{--} \end{pmatrix} = \left[\begin{pmatrix} -W_2 & W_\mathrm{n} & W_\mathrm{e} & W_2 \\ W_\mathrm{n} & -W_0 & W_0 & W_\mathrm{e} \\ W_\mathrm{e} & W_0 & -W_0 & W_\mathrm{n} \\ W_2 & W_\mathrm{e} & W_\mathrm{n} & -W_2 \end{pmatrix} - (W_\mathrm{n} + W_\mathrm{e})\mathbf{1}\right]\begin{pmatrix} N_{++} - N_{++}^{(\mathrm{eq})} \\ N_{+-} - N_{+-}^{(\mathrm{eq})} \\ N_{-+} - N_{-+}^{(\mathrm{eq})} \\ N_{--} - N_{--}^{(\mathrm{eq})} \end{pmatrix}, \tag{3.1}$$

where the various relaxation rates W are as shown in Figure 3.1 and the equilibrium occupancy from Boltzmann statistics. From $\langle I_\mathrm{z}\rangle \propto (N_{++} + N_{-+} - N_{+-} - N_{--})$, we have

$$\frac{\mathrm{d}\langle I_\mathrm{z}\rangle}{\mathrm{d}t} = -(W_0 + W_2 + 2W_\mathrm{n})(\langle I_\mathrm{z}\rangle - \langle I_\mathrm{z}\rangle^\mathrm{eq}) - (W_2 - W_0)(\langle S_\mathrm{z}\rangle - \langle S_\mathrm{z}\rangle^\mathrm{eq}) \tag{3.2}$$

for the nuclear magnetization.

To find the DNP enhancement, we can assume complete saturation of the electron spin transitions with on-resonance microwaves, such that $\langle S_\mathrm{z}\rangle = 0$, and then set $\frac{\mathrm{d}I_\mathrm{z}}{\mathrm{d}t} = 0$ for the steady state solution, which occurs when

$$\langle I_\mathrm{z}\rangle - \langle I_\mathrm{z}\rangle^{(\mathrm{eq})} = -\frac{W_2 - W_0}{W_0 + W_2 + 2W_\mathrm{n}}\langle S_\mathrm{z}\rangle^{(\mathrm{eq})}. \tag{3.3}$$

This leads us to the OE coupling factor ξ described in the literature[105],

$$\xi = \frac{W_2 - W_0}{W_0 + W_2 + 2W_\mathrm{n}}. \tag{3.4}$$

There are additional factors which contribute to the OE enhancement in practice: the leakage factor f accounts for nuclear relaxation not due to the electron, and the saturation factor s accounts for incomplete saturation of the electron spin, for a total enhancement

$$\varepsilon_\mathrm{OE} = \xi f s\frac{\gamma_\mathrm{S}}{\gamma_\mathrm{I}}. \tag{3.5}$$

The relaxation rates W depend on the mechanism of relaxation; these have been calculated for 1) fluctuation of the dipole-dipole component of the hyperfine coupling due to translational or rotational motion, 2) fluctuation of the scalar component of the hyperfine interaction due to exchange processes (scalar relaxation of the first kind), and 3) fluctuation of the scalar component of the hyperfine interaction due to fast electron relaxation (scalar relaxation of the second kind). The exact expressions determined for liquids may not be suitable for use in solids, but the following "pure cases" in the limit of fast-motion ($\omega_S \tau \ll 1$) can be identified:

1. A pure dipolar relaxation leads to $\xi = +\frac{1}{2}$.
2. Pure scalar relaxation of the first kind leads $\xi = -1$.
3. Pure scalar relaxation of the second kind leads to $\xi = -\frac{1}{2}$.

As $\omega_S \tau$ increases (practically, as the magnetic field increases or the correlation time τ increases, particularly relevant for solids), (1) and (3) above decay towards zero, but (2) remains field and τ independent and always yields $\xi = -1$.

As ^{1}H and the electron have opposite sign gyromagnetic ratios, Equation (3.5) implies that a negative coupling factor leads to a positive enhancement and vice-versa. That a strong positive enhancement is observed for BDPA[29] suggests that some form of scalar relaxation is dominant. Moreover, both in 2014[29] and the work of this chapter, negative OE enhancements have been observed for heavily deuterated variants of BDPA. These must be due to dipolar relaxation of nuclei not on the radical molecule. With these observations, we can start to rationalize the field dependence of the OE in BDPA with some hypotheses:

1. The observed OE in BDPA is dominated by scalar relaxation, contributing to a positive OE.
2. There is also a contribution from (potentially intermolecular) dipolar relaxation which leads to a negative OE.

3. The scalar contribution to ξ is largely field-independent (dominated by exchange-type processes) while the dipolar contribution decreases towards zero.

4. Due to (3), a larger positive OE is observed at higher fields.

This chapter documents a series of efforts to investigate the OE by modifying the hyperfine couplings of both trityl and BDPA radicals. For trityl, strong isotropic hyperfine couplings were introduced under the hypothesis that their presence would lead to an OE. For BDPA, we grouped the radicals by their observed isotropic hyperfine couplings and determined the effects of selective deuteration on each group, culminating in a modification with improved OE enhancements relative to BDPA.

3.2 Impact of isotropic hyperfine couplings for trityl

In looking for the properties of BDPA that enable the OE, one may initially note that BDPA has many isotropically hyperfine-coupled protons, with eight isotropic couplings of magnitude $\sim$5 MHz and another eight of magnitude $\sim$1 MHz[106]. Other monoradicals often used for DNP are substituted tetrathiatriarylmethyls (trityls), which share with BDPA a narrow EPR line and long electron relaxation times[107]. However, the most widely-used of these (CT-03 and OX063) are specifically designed to keep any ^{1}H nuclei far from the center of the molecule where the electron is highly localized, minimizing the magnitudes of any hyperfine couplings. Indeed, trityls are known to interact more strongly with solvent protons than with intramolecular protons [108] – an interesting property which makes sense in light of these weak intramolecular couplings. In this study we make use of substitutions of CT-03 (sometimes called Finland trityl) to generate a series of radicals with minimal differences except in the number of isotropic hyperfine couplings. We use high-field DNP and EPR to characterize these radicals, with the anticipation that an Overhauser effect like that of BDPA would be observed.

3.2.1 Introduction and verification of hyperfine couplings

In collaboration with Prof. Yangping Liu and Weixiang Zhai at Tianjin Medical University, we received four radicals: CT-03, CT-02, CT-01, and CT-00, each with a different number of substituent hydrogens (for strong isotropic couplings) or carboxylic acid groups (no strong couplings). The different radicals are presented in Figure 3.2.

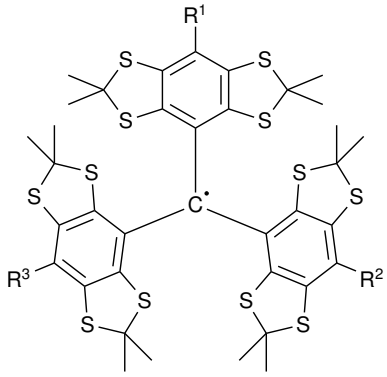

	R^1	R^2	R^3
CT-03	COOH	COOH	COOH
CT-02	COOH	COOH	H
CT-01	COOH	H	H
CT-00	H	H	H

Figure 3.2: Structures of the radicals examined in this section. Left is a generic trityl structure; right is a table specifying each R group for each different radical.

We will not discuss the synthesis of these radicals, but Prof. Liu's group also provided X-band EPR spectra of the radicals in solution, shown in Figure 3.3. From these we could observe a splitting of ∼2.3 G or ∼6.4 MHz for each additional ^{1}H substitution. These couplings are of comparable magnitude to the strongest couplings present in BDPA, so we might predict an OE if comparable relaxation mechanisms exist as well.

3.2.2 High-field EPR under DNP conditions

We started by measuring EPR spectra for each of the samples we would use for DNP using a 140 GHz pulsed EPR spectrometer[68] to obtain results more relevant to high-field DNP. These EPR lines from e.g. solution X-band EPR to characterize the radicals as the concentration of each sample was 15 mM, a more typical value for DNP, as opposed to the very low concentrations for measuring g-tensor and hyperfine parameters. Furthermore, they were acquired under cryogenic conditions and in various glass-forming

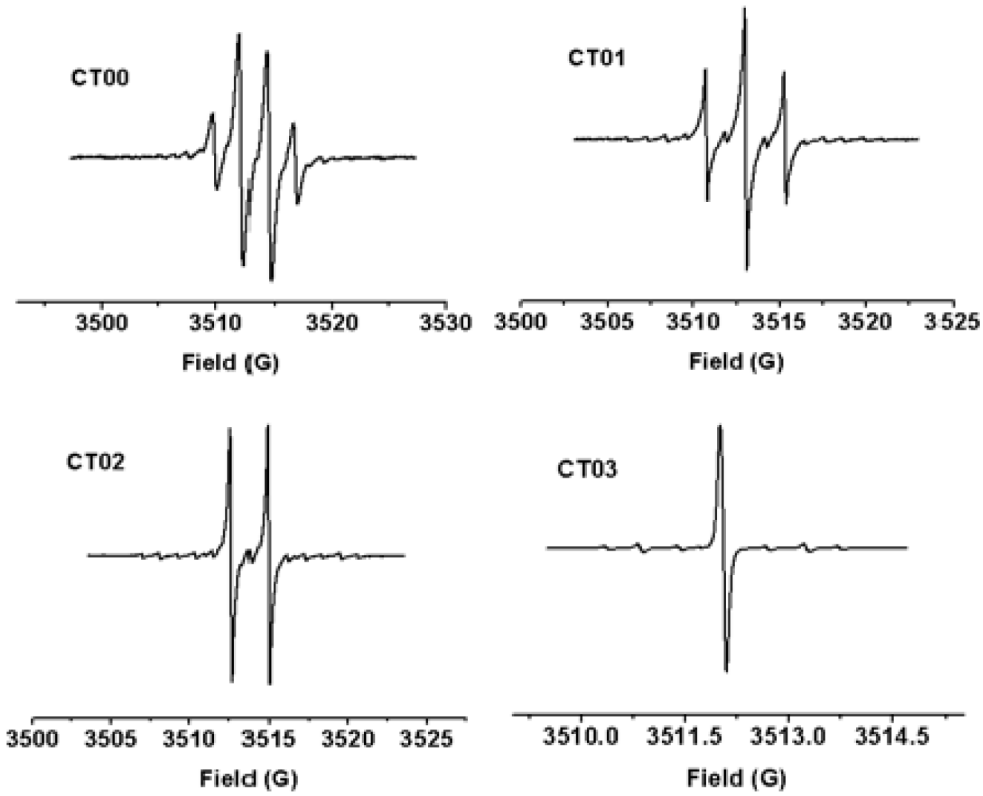

Figure 3.3: X-band EPR spectra of each of the prepared trityl radicals.

matrices appropriate for the solubility properties of each radical. The spectra are plotted in Figure 3.4. Assessing the spectra, we observe a slight overall broadening with each additional strong ^{1}H coupling. The CT-00 spectrum in particular has a pronounced shoulder, probably a result of the convolution of the more pronounced hyperfine splittings with the slight g-anisotropy of trityl that manifests more perceptibly at higher fields. None of these are sufficiently broadened to preclude observing a SE or enable observing a ^{1}H CE, and we have no reason from these spectra to disqualify an OE either.

It has been suggested[109] that in BDPA and trityl samples, radical clusters and a subsequent truncated cross effect (qualitatively somewhere between a pure CE and thermal mixing) leads to Overhauser-like enhancement profiles; this topic will be discussed in more detail in Chapter 4. That a distinct shoulder is observed in the CT-00 spectrum as well as the more mild broadening of the other three radicals could be indicative of

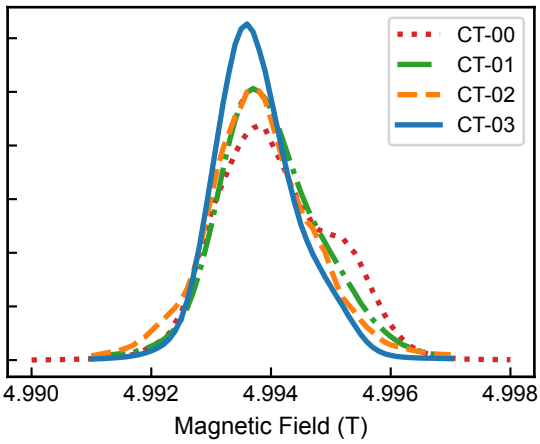

Figure 3.4: Solid state echo-detected EPR spectra at 140 GHz; samples were as described in Section 3.4 and at 80 K under static conditions.

such clustering (an asymmetrically broadened EPR line was considered a hallmark of such). However, we observe that the broadening appears to be a clear result of the introduced hyperfine couplings; in radical clusters, the primary source of broadening is electron-electron dipole couplings. With that said, the four spectra are also in three different matrices (again, due to the solubility limitations), and one would certainly expect clustering behaviors to differ in different environments.

3.2.3 High field DNP

The main question, of course, is how these spectral properties translate to high field DNP. We measured a series of enhancement profiles for three[1] of the radicals at 5 T (140 GHz/211 MHz $e^-/^1H$ Larmor frequency) using a fixed frequency gyrotron as the microwave source and varying the static magnetic field. The profiles are shown in Figure 3.5. A modest SE was observed for CT-00 and CT-03, but not in CT-02 or CT-01. No Overhauser-like features were observed in any of the enhancement profiles.

We decided to examine CT-00, with the greatest number of isotropic couplings, at higher fields to determine if perhaps the favorable scaling of the OE with magnetic field

[1]A full profile was not collected for CT-01 after quickly confirming minimal enhancement at the SE and OE conditions. See Section 2.3.2 for a brief discussion of the problems with field sweeps.

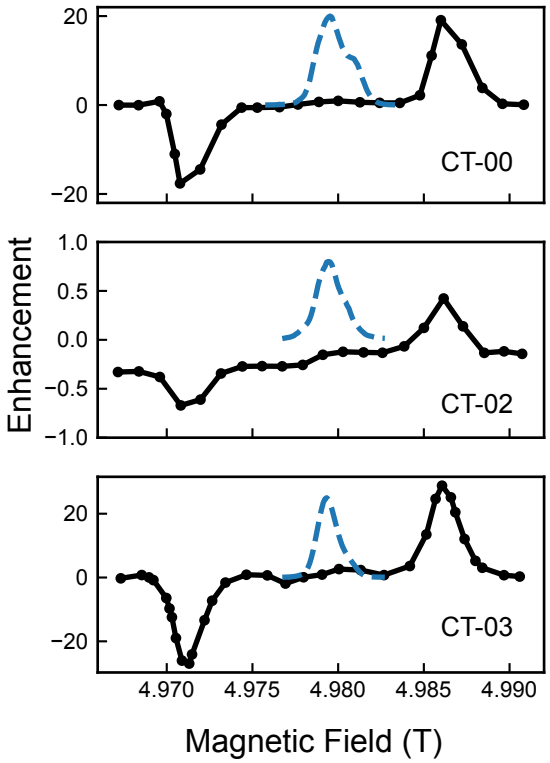

Figure 3.5: DNP enhancement profiles at 211 MHz (black), temperature 85 K and MAS frequency 5 kHz. As a visual aid, the EPR spectra in Figure 3.4 are plotted for each profile (dashed blue), slightly scaled and shifted to account for the small difference in microwave frequency between the instruments.

would render it observable. The profiles are plotted in Figure 3.6 with a common x-axis for ease of comparison between fields.

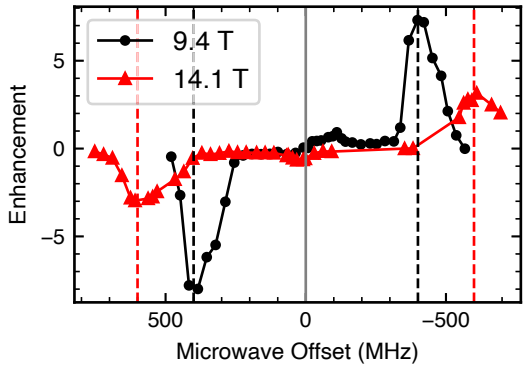

Figure 3.6: Enhancement profiles of CT-00 at 9.4 T and 14.1 T; positions of the SE extrema (dashed vertical lines) were used as internal references for a common frequency offset axis. For these profiles, the temperature was 100 K and samples spun at 8 kHz.

The SE enhancement approximately follows the $1/\omega_{0I}^2$ predicted dependence. Near zero offset, we see small fluctuations seeming to shift from an asymmetric profile at 9.4 T to a more symmetric and negative profile at 14.1 T. The enhancement is small, so perhaps further discussion is not warranted, but we might assume it to be a negative OE. A negative OE would run contrary to the notion that the introduction of strongly isotropically coupled protons would lead to a positive OE thanks to cross-relaxation via a scalar relaxation mechanism. Speculating, it *could* be the case that both dipolar relaxation and scalar relaxation of the second kind are active (of comparable magnitude and opposite sign) and that these fields are an intermediate regime ($\omega_S\tau \sim 1$) for both; the specific field dependence for each contribution to the OE could render one or the other slightly larger and thus plausibly yield a slight negative OE (due to the dipolar contribution) at some fields.

Revisited with the AMC

The results in the previous sections present an interesting negative conclusion regarding the role of scalar hyperfine couplings in MAS DNP insofar as they are not singly sufficient for an OE. But our selection of samples, and particularly the decision to analyze only one sample at 9.4 T and 14.1 T, rendered it difficult to deconvolute the effects of the glassing matrix, known to be critical for the OE in BDPA, and the radical itself. To address this, we prepared a new set of samples, again 15 mM in suitable glassing matrices, but for each matrix two radicals were analyzed. This resulted in six samples; for each we collected a frequency profiles with the 250 GHz/380 MHz spectrometer (Chapter 2) and these are plotted in Figure 3.7.

The low magnitudes of the SE enhancements are primarily due to the low power of the microwave source. Moreover, the SE enhancements for CT-01 and CT-02 were low even at 140 GHz, so the particularly low enhancements here are expected. Regarding the center regions of the profiles, the enhancements are also small; from what we have

seen of the OE it produces comparable enhancement both with 160 mW from our AMC and several watts from a gyrotron. We can make a general observation for each matrix about the effect of including one additional isotropic coupling on the central profile:

1. In 1,1,2,2-tetrachloroethane (TCE), the dispersive profile of CT-01 shifts towards an absorptive profile for CT-00 with an additional coupling.

2. In 6:3:1 (vol.) DMSO-d_6:D_2O:H_2O, the mostly absorptive profile of CT-02 becomes essentially zero for CT-01.

3. In 6:3:1 (vol.) glycerol-d_8:D_2O:H_2O, the asymmetrical, mostly negative CT-03 profile shifts towards zero for CT-02.

Observations (1) and possibly (3) are consistent with the notion that the additional coupling *does* contribute to scalar relaxation and thus a slight positive OE. Observation (2) is strange and might indicate a problem with the CT-01 radical itself or the sample preparation in DMSO, but this was not investigated further. Ultimately, these results bolster our conclusion that one cannot "convert" an arbitrary narrow-line radical such as CT-03 to a radical suitable for OE DNP exclusively by introducing additional isotropically coupled protons.

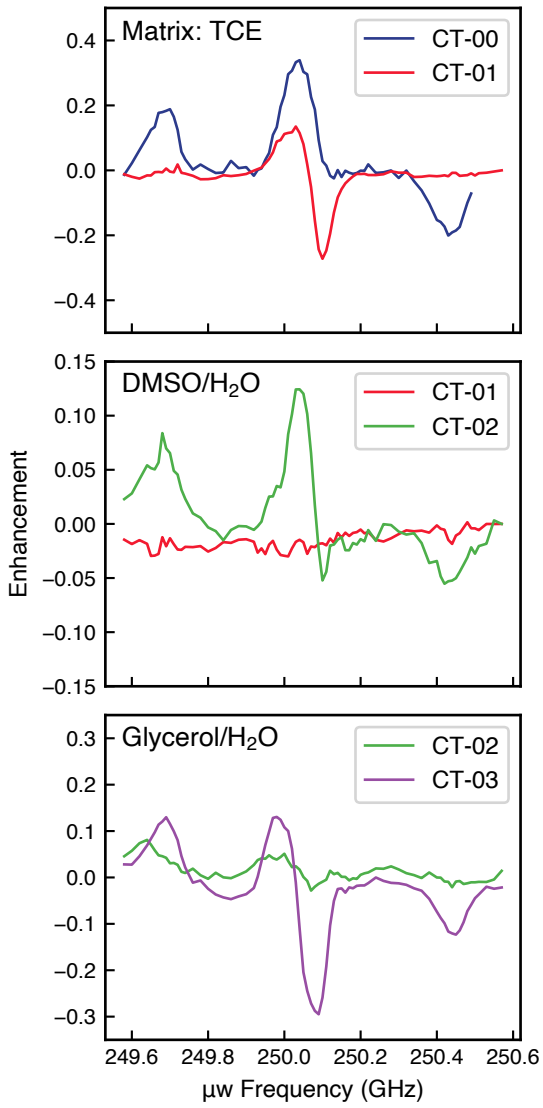

Figure 3.7: Enhancement profiles of 15 mM at 250 GHz/380 MHz, matrices are as described in the text. All experiments performed at 100 K and 5 kHz MAS.

3.3 Investigation of OE in BDPA via selective deuteration

Another angle from which to approach the question of why BDPA was unique among polarizing agents in terms of generating an OE in solids was to modify BDPA and alter the OE in that way. In particular, we aimed to observe the effect of removing each group of protons from BDPA to identify which of those protons are most involved in the OE and potentially other aspects of DNP such as spin diffusion processes.

3.3.1 The role of each set of hyperfine couplings

The central carbon atom of BDPA has three attached groups: two fluorene moieties and one phenyl ring. On the fluorenes, there four unique hydrogen atoms, marked [α, β, γ, δ] in Figure 3.8(a), while the phenyl ring has three unique hydrogens (*ortho*, *meta*, and *para*). The isotropic hyperfine couplings to each ^{1}H (i.e., for h_{21}-BDPA) have been measured via ENDOR[106]: in MHz these are -5.54 and -5.29 for α and γ, +1.38 and +1.09 for β and δ, -0.5 for *ortho* and *para*, and -0.15 for *meta*. More succinctly, the α and γ protons have *strong* isotropic couplings, the β and δ protons have *weak* isotropic couplings, and the protons on the phenyl ring have *very weak* isotropic couplings.

In collaboration with Prof. Swager and Léo Delage-Laurin in the organic chemistry division at MIT, we were able to obtain, through their novel synthetic scheme[81], three new variants of BDPA: 1,3-[d_{16}]-BDPA, 1,3-[α, γ-d_8]-BDPA, and 1,3-[β, δ-d_8]-BDPA, shown in Figure 3.8 along with X-band EPR spectra confirming the predicted hyperfine coupling parameters for each.

These radicals have been designed to isolate the role of each group of protons in the OE. Each radical was doped into OTP at 2.5 wt. %, degassed (see Section 3.4), and DNP enhancement profiles measured at 250 GHz/380 MHz using the solid-state source. The resultant profiles are shown in Figure 3.9.

The enhancement of ∼70 for h_{21}-BDPA, achieved with only the 160 mW solid state mi-

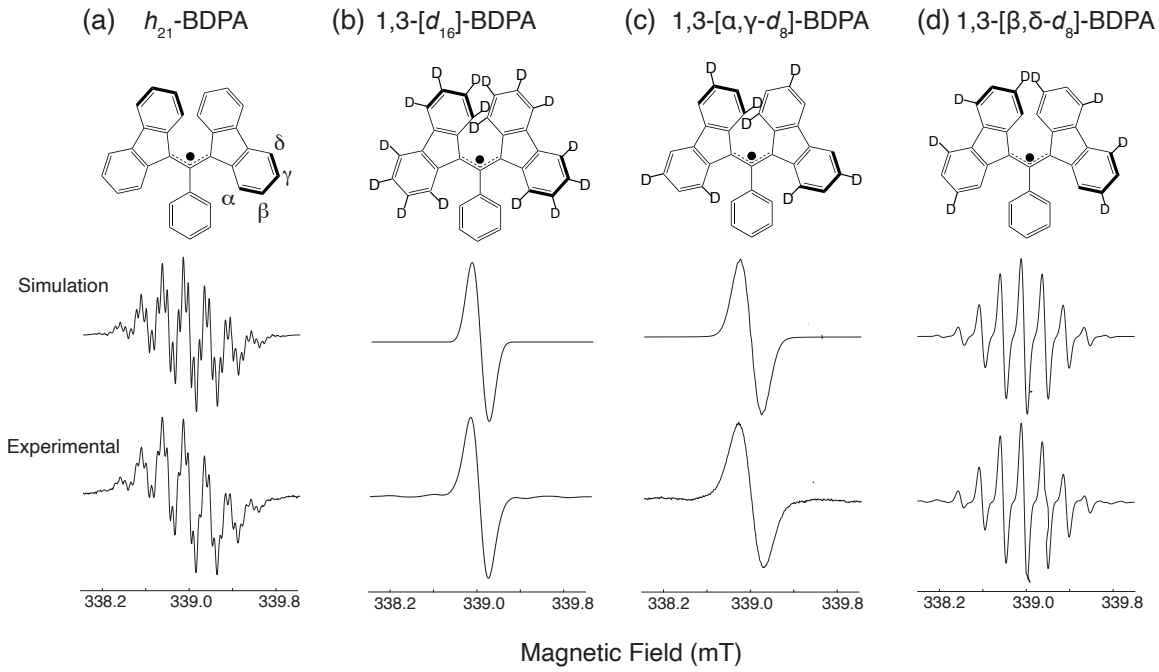

Figure 3.8: Molecular structures and room-temperature solution X-band EPR spectra (simulated and experimental) of (a) h_{21}-BDPA, (b) 1,3-[d_{16}]-BDPA, (c) 1,3-[α, γ-d_8]-BDPA, and (d) 1,3-[β, δ-d_8]-BDPA. Parameters for simulations come from literature values[106], with couplings to deuterium scaled by $\gamma_D/\gamma_H = 1/6.51$. See Table 1 of Delage-Laurin et al.[81].

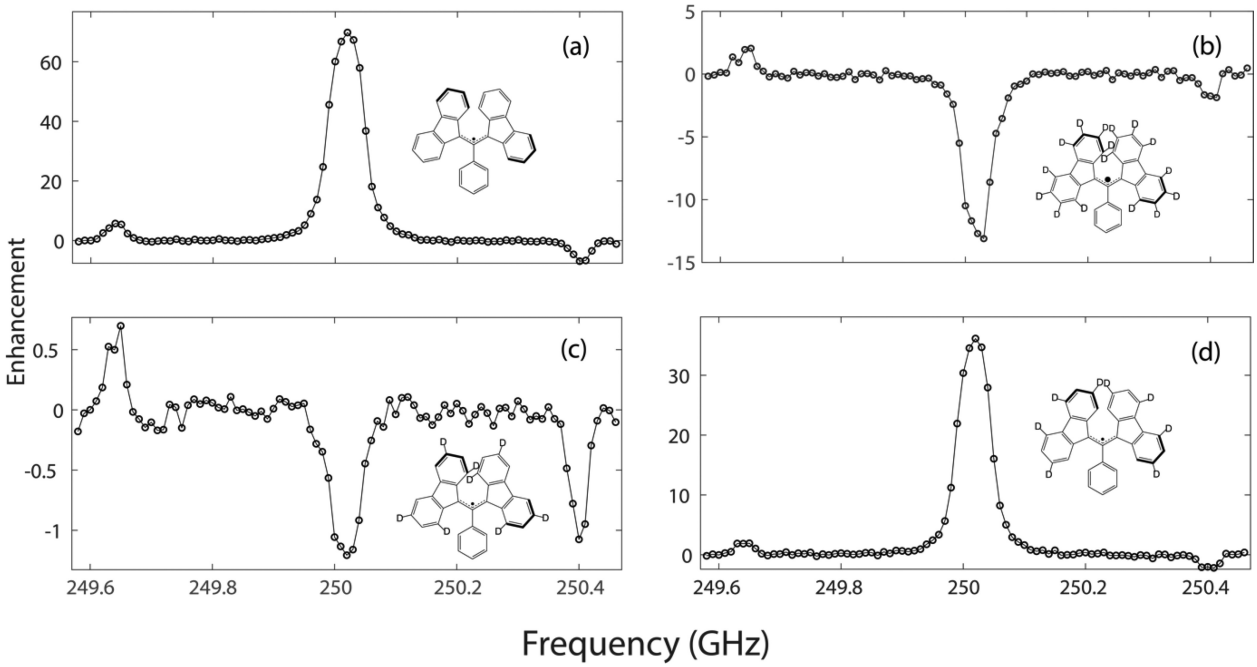

Figure 3.9: DNP enhancement profiles for samples containing (a) h_{21}-BDPA, (b) 1,3-[d_{16}]-BDPA, (c) 1,3-[α, γ-d_8]-BDPA, and (d) 1,3-[β, δ-d_8]-BDPA.

crowave source, is itself notable as a demonstration of the impact of degassing on OE performance. We might understand this in a couple ways, going back to Equation (3.5): dissolved O_2 (paramagnetic) both shortens relaxation times for the BDPA radical, decreasing the saturation factor s, and contributes to relaxation pathways for the nucleus, decreasing the leakage factor f. Indeed, we routinely use a significant increase in the nuclear T_1 as an indication that degassing was successful.

Deuteration of all hydrogens on the fluorene moieties in 1,3-[d_{16}]-BDPA results in an enhancement of -13 (Figure 3.9(b)), indicating that the remaining nearby ^{1}H nuclei (those on the phenyl ring and in the OTP matrix) primarily experience dipolar relaxation, resulting in a positive coupling factor ξ and thus a negative OE. Deuterating only the strongly-coupled [α, γ] sites leads to an enhancement of -1 (Figure 3.9(c)), essentially eliminating the OE. This result confirms our expectations that the strongly coupled protons are the primary contribution to the observed positive OE of BDPA. By comparison with 1,3-[d_{16}]-BDPA in Figure 3.9(b), we can also infer the role of the [β, δ] protons:

they must contribute a positive OE in order for an enhancement of −1 and not −13 to be observed. Indeed, in the enhancement profile of 1,3-[β, δ-d_8]-BDPA in Figure 3.9(d), an enhancement of +36 is observed – about half the magnitude of fully protonated BDPA. Evidently, these [β, δ] protons are needed for maximum OE enhancements. Their contribution is somehow complicated, though: from Figure 3.9(b) and (c) we might naively predict their effect to be a "net" 12, while from (a) and (d) we might predict 34. That is, alone they contribute only a small OE (12), but when the [α, γ] protons are present their effect is large (34). We suggest that this indicates the role of the [β, δ] protons in enabling efficient spin diffusion from the [α, γ] protons to the bulk.

Finally, we measured spin-lattice relaxation times (T_1) and OE buildup times (T_B) for each of these radicals, shown in Table 3.1. As long as the [α, γ] protons are present, the T_1 is comparable: ∼43 and 37 s for h_{21}- and 1,3 – [β, δ-d_8]-BDPA, respectively. When these protons are absent, the nuclear T_1 is much longer. In all cases, T_B is comparable to T_1; in conjunction with the minimal power dependence of the OE (*vide infra*) we can reasonably assume that the observed buildup rate is primarily the spin diffusion rate and not the DNP polarization transfer rate[75].

Radical	T_1 (s)	T_B (s)	ε_{OE}
h_{21}-BDPA	42.7 ± 3.3	43.6 ± 2.3	70 ± 3
1,3-[d_{16}]-BDPA	66.4 ± 4.0	74.0 ± 5.8	−13 ± 1
1,3-[α, γ-d_8]-BDPA	66.7 ± 4.9	71.6 ± 6.4	−1.0 ± 0.2
1,3-[β, δ-d_8]-BDPA	36.8 ± 1.2	41.3 ± 2.0	36 ± 4

Table 3.1: Relaxation times T_1, DNP buildup times T_B, and observed Overhauser enhancements for BDPA and the three deuterated variants.

3.3.2 Attenuation of DQ cross-relaxation with deuteration

The only remaining group of intramolecular protons to examine are those on the phenyl ring. Already from Figure 3.9 we can draw some initial hypotheses, but only for the effect of the phenyl protons in combination with the bulk. Again, we observed that the phenyl

and bulk protons together contribute a modest negative OE via dipolar cross-relaxation. We could therefore reasonably expect an increase in the OE upon deuteration of the phenyl ring. But to what extent was unknown, and in particular we had observed that deuteration of certain groups can potentially influence non-OE aspects of DNP such as spin diffusion.

We again received radicals from our collaborators, this time a pair to essentially complete the dataset of Section 3.3.1: one fully deuterated d_{21}-BDPA, and the other 2-[d_5]-BDPA (which we will refer to as Phe-d_5-BDPA). To start, we compared the DNP enhancement profiles of d_{21}-BDPA and 1,3-[d_{16}]-BDPA, shown in Figure 3.10. Compared to the enhancement of −13 obtained when only the phenyl protons are present, the additional deuteration of these protons *increases* the OE enhancement to −6.4. This is clear evidence that these phenyl protons are indeed experiencing relaxation via a predominantly dipolar mechanism and thus contributing a negative OE.

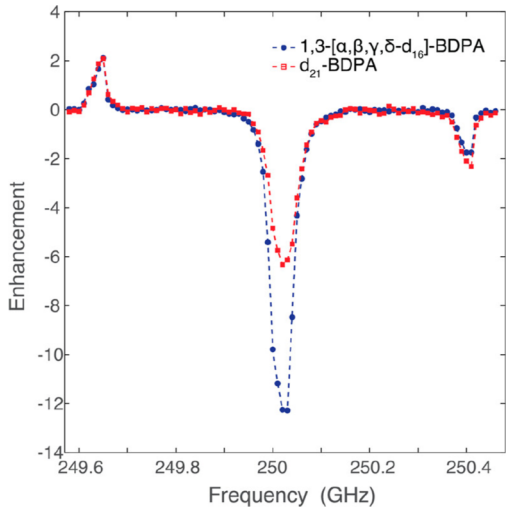

Figure 3.10: DNP frequency profiles of 1,3-[d_{16}]-BDPA (blue) and d_{21}-BDPA (red) acquired at 8.9 T, both spinning at a MAS frequency of 5 kHz and at temperature 90 K.

By comparing Phe-d_5-BDPA to fully protonated h_{21}-BDPA, we can observe the effect of deuterating the phenyl ring while all other protons are present. Figure 3.11 shows a series of enhancement profiles observed for non-degassed h_{21}-BDPA and Phe-d_5-BDPA with several spectrometers. There are a few key instrumental differences between the

spectrometers beyond the field: profiles were recorded as field sweeps with gyrotrons (at 5 and 14.1 T) and frequency sweeps with solid-state sources (8.9 and 9.4 T); in 4 mm rotors at 90 K (5 and 8.9 T) and 3.2 mm rotors at 100 K (9.4 and 14.1 T); using microwave powers of 2 W at 5 T, 160 mW at 8.9 T, 280 mW at 9.4 T, and 30 W at 14.1 T. Overall, Phe-d_5-BDPA consistently exhibits a higher OE DNP enhancement than h_{21}-BDPA, at least up to a field strength of 14.1 T.

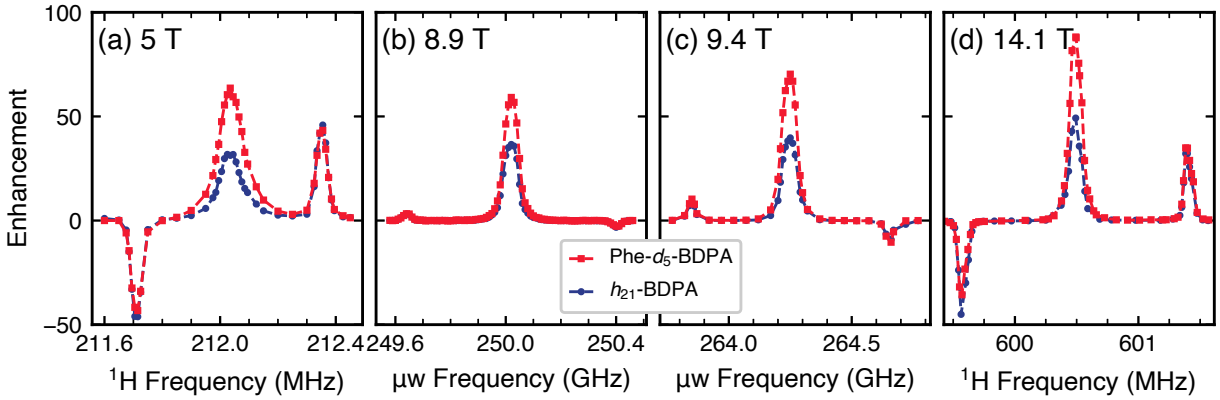

Figure 3.11: Enhancement profiles of Phe-d_5- and h_{21}-BDPA recorded at several fields. (a) Field profile obtained at 5 T, (b) frequency profile obtained at 8.9 T, (c) frequency profile obtained at 9.4 T, and (d) field profile obtained at 14.1 T. Samples were at 90 K (a,b) or 100 K (c,d) and spinning at 3.5 kHz (a) or 5 kHz (b–d).

We also measured spin-lattice relaxation times (T_1) and DNP buildup times (T_B), presented in Table 3.2. The T_1 increases upon deuteration of the phenyl ring, which we can easily rationalize by the fact that there are now fewer ^{1}H nuclei on the radical in direct contact with the rapidly relaxing electron: without microwave irradiation driving them towards hyperpolarization, the phenyl protons act as a polarization sink for the bulk nuclei. By comparison with Table 3.1, it is interesting to note that deuteration of the more strongly coupled [β, δ] protons did *not* lead to an increase in T_1. Perhaps this is due to the presence of the [α, γ] protons dominating relaxation via the same scalar mechanisms, while relaxation via the phenyl protons manifests in other terms (dipolar mechanism). T_B remains comparable to T_1 for Phe-d_5-BDPA but might be evaluated as slightly faster, suggesting that spin diffusion may not be the only factor in the effective

buildup rate, but a more systematic study may be warranted.

	h_{21}-BDPA		Phe-d_5-BDPA	
	T_1	T_B	T_1	T_B
8.9 T	32.1 ± 2.2	37.5 ± 1.5	38.0 ± 0.4	29.6 ± 0.3
14.1 T	31.9 ± 1.5	30.1 ± 1.5	37.1 ± 3.9	28.9 ± 2.0

Table 3.2: Relaxation times and OE buildup times for (non-degassed) h_{21}-BDPA and Phe-d_5-BDPA measured at 8.9 and 14.1 T. T_1 is measured without microwave irradiation, while T_B is measured for microwave irradiation at the OE maximum.

The observed field scaling of Phe-d_5-BDPA makes it an appealing choice for high field DNP, especially compared to other monoradicals. Also of import for high-field use are its MAS and microwave power dependence, shown in Figure 3.12. Up to the maximum possible spinning frequency of the 3.2 mm rotor at 100 K of 12.5 kHz, we observe a slight increase in OE enhancement with spinning frequency, consistent with previous studies[32, 103]. For the power, only 280 mW appears sufficient to saturate the OE at this field; the minimal power requirement has also been reported previously[29] though at higher fields it seems at least a few watts are required for complete saturation[32].

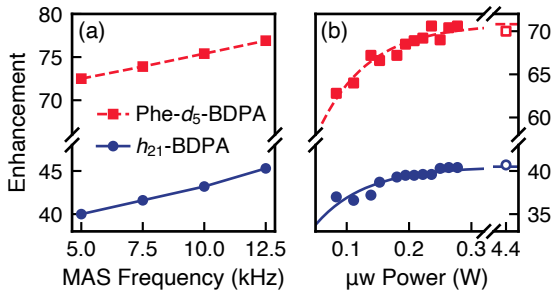

Figure 3.12: Experimental ^{1}H DNP enhancements of h_{21}-BDPA and Phe-d_5-BDPA as a function of (a) MAS frequency and (b) incident microwave power obtained at the 9.4 T DNP spectrometer with a maximum power of 280 mW. The empty circle and square in (b) are data points obtained on the 8.9 T DNP spectrometer with an incident microwave power of 4.4 W from a gyrotron. All data were obtained at a nominal temperature of 100 K, with some variation in sample heating due to MAS in (a); data in (a) were obtained with incident microwave power 280 mW and data in (b) were obtained at MAS frequency 5 kHz.

3.4 Materials and methods

This section describes the sample preparation and experimental protocols for high-field EPR and DNP.

3.4.1 Sample preparation

Modified trityls

For the initial preparations of the trityl radicals (data in Figures 3.4 to 3.6), a 15 mM solution was prepared in an appropriate (for the radical's solubility properties) cryoprotectant matrix. CT-03 and CT-02 were prepared in 6:3:1 (vol.) glycerol-d_8:D_2O:H_2O, CT-01 was prepared in 6:3:1 (vol.) dimethyl sulfoxide (DMSO)-d_6:D_2O:H_2O, and CT-00 in 95:5 ^2H:^1H OTP. For OTP, a solid at room temperature, the solution was prepared by first dissolving both the radical and OTP into $CDCl_3$ and allowing the chloroform to evaporate; the resultant solid was scraped from the watchglass, finely ground, and packed into a rotor as a powder. Before inserting into the probe, the CT-00/OTP samples were heated to $\sim$60 °C to melt the matrix and ensure proper glass formation. For high-field EPR the same samples were used but rather than a rotor, they were drawn into a small capillary vial (0.55 mm OD).

For the later preparations examined with the AMC (Figure 3.7), new 15 mM solutions were prepared of CT-03 and CT-02 in 6:3:1 (vol.) glycerol-d_8:D_2O:H_2O, CT-02 and CT-01 in 6:3:1 (vol.) DMSO-d_6:D_2O:H_2O, and CT-01 and CT-00 in 1,1,2,2-tetrachloroethane (TCE). Note that because of its low ^1H density, TCE can be used at natural abundance while retaining favorable spin diffusion characteristics.

BDPA and deuterated variants

All radicals were doped at 2.5% by weight into 95:5 ^{2}H:^{1}H OTP in a process like that described above and in Section 2.4, with initial dissolution in $CDCl_3$, evaporation to yield a thin film, and finally packing as a powder into an appropriate 4 mm or 3.2 mm rotor. Melting prior to insertion into the probe was again performed for all samples.

For degassed samples, a freeze-pump-thaw process was performed directly on the sample in the rotor using a 3D printed adapter (details in Supporting Information of Delage-Laurin et al.[81]). Briefly, the adapter sealed the rotor from atmosphere with an O-ring and connected the top of the rotor to a three-way valve which could connect the rotor contents either to vacuum or nitrogen purge gas. Following five freeze-pump-thaw cycles, the rotor was kept immersed in liquid nitrogen while being transferred to a glove bag, then removed from the adapter and the endcap inserted in the nitrogen atmosphere. The rotor was again kept frozen in liquid nitrogen until insertion into the precooled DNP probe.

Purity and effective radical concentrations

Following some concern of possible degradation of BDPA and the deuterated derivatives, we used UV-vis experiments to estimate the concentration of commercially available h_{21}-BDPA. More specifically, we prepared solutions of different nominal concentrations of stock h_{21}-BDPA, collected UV-vis spectra, and used these to measure the extinction coefficient of BDPA. Our value for the extinction coefficient was only about half that found in the literature[110], prompting investigation with matrix assisted laser desorption ionization-time of flight mass spectrometry (MALDI-TOF MS) which determined that the primary degradation product was hydroxylated BDPA. This and a minor product of hydroperoxylated BDPA could be removed with silica gel chromatography but would quickly reappear without the addition of 1:1 benzene.

The electron spin concentration of each sample was determined by spin counting

experiments in a Magnettech ESR5000 spectrometer and comparison to a known standard. The entire 4 mm rotor was used as the sample, so the sample volume could be determined from the rotor ID and the sample length. The determined relative concentrations for the h_{21}:1,3 – [d_{16}]:1,3 – [α, γ-d_8]:1,3 – [β, δ-d_8] samples were ∼2.2 : 3.1 : 1 : 3.4; we do not believe this affects any general conclusions we have drawn.

The data for UV-vis, MALDI-TOF, and ESR spin counting experiments are available in the Supporting Information of Delage-Laurin et al[81].

Subsequent deuterated BDPA variants, particularly Phe-d_5, were immediately stored as a 1:1 complex with benzene, similar to commercial samples, to slow the hydroxylation process. We used UV-vis to determine the relative concentrations of our preparations of h_{21}-BDPA and Phe-d_5-BDPA, and found them nearly equal, 1.0:1.2 (Supporting Information, Palani and Mardini et al.[82]). Even assuming that the enhancement is linear with radical concentration, Phe-d_5-BDPA still outperforms h_{21}-BDPA by around 50% at all fields.

3.4.2 Methods for high-field EPR

Echo-detected EPR spectra in Figure 3.4 were acquired at 80 K using a 140 GHz pulsed EPR spectrometer[68]. Each spectrum is the average of at least 20 repeated field sweeps, with a field point spacing of 1 G. For each point, 400 echo intensities were averaged using a 4-step phase cycle. Typical pulse widths of the $\pi/2$ pulses for the Hahn echoes ∼100 ns, though they vary between samples due to variations in the cavity tuning, as do the inter-pulse delay times τ due to differing T_2 values. Specific details of the experimental parameters for each sample are given in Table 3.3.

Sample	Field Range (T)	N_{averages}	$t_{\pi/2}$ (ns)	τ (ns)
CT-03	4.991–4.997	50	120	500
CT-02	4.991–4.997	24	60	600
CT-01	4.991–4.997	60	60	200
CT-00	4.990–4.998	50	260	150

Table 3.3: Details of 140 GHz EPR experiments.

3.4.3 Methods for DNP-NMR

5 T/140 GHz

DNP field profiles of modified trityls (Figure 3.5) were conducted using a home-built DNP spectrometer equipped with a 139.6 GHz gyrotron[61] outputting ~5 W microwave power and a RNMR console (courtesy Dr. David J. Ruben). Samples were spun at 5 kHz in 4 mm Varian-style rotors, and cooled to 85 K using a home-built liquid nitrogen heat exchanger and cryogenic MAS probe. The ^{1}H NMR signal was measured with a Hahn echo after a recycle delay of 10 s and 2 dummy scans to establish the equilibrium polarization.

Profiles of h_{21}- and Phe-d_5-BDPA (Figure 3.11(a)) were collected on the same spectrometer, but with the gyrotron outputting less power, about 2 W. Samples were spun at 3.5 kHz and cooled to 90 K. The ^{1}H NMR signal was measured with a solid echo following a train of 48 saturation pulses and a recovery delay of 40 s ($\sim 1.3T_1$).

8.9 T/250 GHz

All DNP frequency profiles at this field were acquired with the 380 MHz equipped with the AWG-AMC solid state source (Chapter 2).

Frequency profiles of the modified trityls (Figure 3.7) were acquired at MAS frequency 5 kHz and temperature 100 K. NMR signals were measured via a simple 90-acquire following saturation pulses and a recovery delay set to approximately $1.3 \times T_1$ for each sample, which varied for different radicals in different matrices. The recovery delays

were 40 s for CT-00/TCE, 55 s for CT-01/TCE, 26 s for CT-01/DMSO, 15 s for CT-02/DMSO, 18 s for CT-02/glycerol, and 50 s for CT-03/glycerol.

DNP frequency profiles of BDPA and deuterated variants (Figures 3.9, 3.10, and 3.11(b)) were collected at MAS frequency 5 kHz and temperature 90 K. The ^{1}H NMR signal was measured with a solid echo following saturation pulses and a recovery delay of 40 s ($\sim 1.3T_1$).

The gyrotron data (empty points in Figure 3.12(b)) were collected with the 250 GHz tuned to the frequency of the OE maximum[99, 111].

9.4 T/263 GHz and 14.1 T/395 GHz

We gratefully acknowledge the support of Drs. James Kempf, Daniel Banks, Ivan Sergeyev, and the late Melanie Rosay in conducting these experiments at Bruker BioSpin in Billerica, MA. DNP enhancement profiles of CT-00 at 9.4 and 14.1 T (Figure 3.6) were conducted as field sweeps with gyrotrons outputting ~20 W microwave power; samples were spun at 8 kHz in 3.2 mm Bruker rotors at 100 K. Matching the experiments at 5 T, the ^{1}H NMR signal was measured with a Hahn echo after a recycle delay of 10 s.

For the profiles of h_{21}- and Phe-d_5-BDPA at 9.4 and 14.1 T (Figure 3.11(c–d)), the 400 MHz spectrometer was equipped with a 280 mW solid state source at 263 GHz similar to our own at 250 GHz (but without an AWG). As such, these profiles were performed as frequency sweeps. The 395 GHz/600 MHz profile was a field sweep with a gyrotron outputting ~30 W. For these profiles, the 3.2 mm rotor was spun at 5 kHz and at 100 K. The NMR experiments were again a train of saturation pulses followed by a solid-echo sequence.

The MAS and power dependencies (Figure 3.12) were measured at 9.4 T using otherwise identical experiments as those of the frequency profile, but with the microwave frequency set to that of the OE maximum.

3.5 Conclusions

In the work described in this chapter we have gained some key insights into the nature of the Overhauser effect and particularly the role of hyperfine couplings on the mechanism. By systematically introducing additional hyperfine couplings to a narrow line radical which does not exhibit, we have seen that merely possessing a few strong isotropic hyperfine couplings is not sufficient for the OE to be active in solids. This result is consistent with other studies on the mechanism of the OE in BDPA, ascribing it to the mixed-valence character of BDPA[32, 112, 113]: the unpaired electron is not truly delocalized but rather hops between the two fluorene moieties, with concomitant changes in the hyperfine couplings. Such a process is not possible in Finland trityl or OX063: the electron is too strongly localized to the single central carbon. The additional hyperfine couplings do seem to have some impact on cross-relaxation but the effects are small, probably because they do not experience cross-relaxation due to exchange.

As for BDPA, we have identified the contribution of each group of intramolecular protons to the overall OE. For the strongly coupled [α, γ] protons, these are critical to the OE, as predicted. The modestly coupled [β, δ] protons seem to contribute a weak OE on their own but are also crucial in maximizing the OE from the [α, γ] protons, probably by enabling efficient spin diffusion. Finally, the very weakly coupled protons on the phenyl ring contribute a negative OE, and their removal via deuteration substantially increases the OE for Phe-d_5-BDPA, indicating a direction for further developments in OE radicals.

Overall, through this work and others, the field is well on its way to iterative rational design of OE polarizing agents for use in a wider variety of glassing matrices[2]. In conjunction with compact, low-cost microwave sources, which we have shown to be sufficient for OE DNP, these will make DNP more accessible without a large investment in, for example, a gyrotron.

[2]Though, the role of the glassing matrix and why BDPA in OTP seems to exhibit a particularly large OE is not completely understood.

Chapter 4

New Mechanisms: Three-Spin Solid Effect and Resonant Mixing

The previous chapters have described research motivated by very practical factors: more flexible microwave sources to enable pulsed DNP (Chapter 2) and an understanding of the Overhauser effect which seems like a good mechanism for high-field DNP (Chapter 3). But working at the intersection of NMR and EPR, we sometimes encounter unexplained results with no apparent applicability but which nevertheless drive our curiosity. This chapter describes two such projects in which I participated. The first began with observation of a highly forbidden three-spin solid effect: we explained the physics involved, in particular the sensitivity to electron-nuclear distance, and subsequently compared simulation to experiment to better understand spin diffusion in glycerol-water. The second was sparked by an unexpected enhancement profile of trityl at low power (e.g. Figure 2.7(c)) and a search for explanations in known mechanisms before ultimately finding it best explained by a new mechanism termed Resonant Mixing. *The contents of this chapter are published in "Three-spin solid effect and the spin diffusion barrier in amorphous solids" by Tan et al.[114], "Dynamic nuclear polarization with trityl radicals" by Palani et al.[92], and "Resonant mixing dynamic nuclear polarization" by Quan et al.[93].*

4.1 Three-spin solid effect

In Section 1.2.2, we derived the solid effect arising from the pseudosecular $\hat{S}_z\hat{I}_\pm$ terms in the hyperfine coupling Hamiltonian. The matching condition was that the microwave offset frequency should match the nuclear Larmor frequency, $\Omega_S = \pm\omega_{0I}$. The observation of a higher-order SE, at $\Omega_S = \pm 2\omega_{0I}$, was also made by de Boer et al.[115, 116] but without further investigation except to comment that the result was consistent with the interaction of a single electron with two nuclei, hence a three-spin solid effect (TSSE). Smith et al. characterized the condition using indirectly, measuring the loss of electron polarization via EPR in SA-BDPA[76]. They did not observe nuclear enhancement at these conditions, concluding that the nuclei polarized were very close to the radical center i.e. within the spin diffusion barrier, and thus did not contribute to the observable (bulk) nuclear polarization.

At low field (0.35 T) we are actually able to observe directly the enhancement due to the TSSE. Moreover, due to its additional sensitivity to the electron-nuclear coupling compared to the (two-spin) SE, we can use a series of experiments to localize exactly which protons can be polarized; the coupling can then be read off from an electronic structure calculation, verified with DNP simulation, and then interpreted as an upper bound for the size of the spin diffusion barrier.

4.1.1 Theory

The Hamiltonian, in the electron rotating frame, for a spin system consisting of an electron and two nuclei, is

$$\hat{H}_0 = \Omega_S\hat{S}_z - \omega_{0I}\left(\hat{I}_{1z} + \hat{I}_{2z}\right) + \hat{S}_z\left(A_1\hat{I}_{1z} + A_2\hat{I}_{2z}\right) + \hat{S}_z\left(B_1\hat{I}_{1x} + B_2\hat{I}_{2x}\right), \qquad (4.1)$$

where Ω_S is the electron offset frequency, ω_{0I} is the nuclear Larmor frequency, A_k are the secular components of the hyperfine couplings, and B_k are the nonsecular components. Following the protocol of Hu et al.[90], we define polarization operators

$$\begin{aligned} \hat{S}^{\alpha} &= \frac{1}{2}\hat{\mathbf{1}} + \hat{S}_z \\ \hat{S}^{\beta} &= \frac{1}{2}\hat{\mathbf{1}} - \hat{S}_z \end{aligned}. \tag{4.2}$$

If we rewrite Equation (4.1) in terms of the polarization operators we have

$$\begin{aligned} \hat{H}_0 = \frac{1}{2}\Omega_S\left(\hat{S}^{\alpha} - \hat{S}^{\beta}\right) + \frac{1}{2}\sum_{k=1}^{2}\Big\{ & S^{\alpha}\left[(A_k - 2\omega_{0I})\hat{I}_{kz} + B_k\hat{I}_{kx}\right] \\ & - S^{\beta}\left[(A_k + 2\omega_{0I})\hat{I}_{kz} + B_k\hat{I}_{kx}\right]\Big\} \end{aligned} \tag{4.3}$$

so diagonalization ($\hat{H}_0^{\wedge} = \hat{U}\hat{H}_0\hat{U}^{-1}$) is accomplished via

$$\begin{aligned} \hat{U} &= \exp\left\{-i\sum_{k=1}^{2}\left(\eta_{k\alpha}\hat{S}^{\alpha}\hat{I}_{ky} + \eta_{k\beta}\hat{S}^{\beta}\hat{I}_{ky}\right)\right\} \\ \text{with } \eta_{k\alpha} &= \tan^{-1}\frac{B_k}{A_k - 2\omega_{0I}};\ \eta_{k\beta} = \tan^{-1}\frac{B_k}{A_k + 2\omega_{0I}}. \end{aligned} \tag{4.4}$$

From the diagonalized Hamiltonian we can identify the matching conditions for each individual SE (that is, the ZQ and DQ transition for each electron-nuclear pair) and the triple quantum (TQ, $\left|\alpha\alpha\alpha^{\wedge}\right\rangle \leftrightarrow \left|\beta\beta\beta^{\wedge}\right\rangle$) and single quantum (SQ, $\left|\alpha\beta\beta^{\wedge}\right\rangle \leftrightarrow \left|\beta\alpha\alpha^{\wedge}\right\rangle$) TSSE transitions by setting the eigenvalues of the relevant states equal to one another and solving. For the TSSE transitions this yields

$$\Omega_S = \pm\frac{1}{4}\sum_{k=1}^{2}\left(\sqrt{B_k^2 + (A_k + 2\omega_{0I})^2} + \sqrt{B_k^2 + (A_k - 2\omega_{0I})^2}\right) \approx \pm 2\omega_{0I} \tag{4.5}$$

where for the last approximation we assume $\omega_{0I} \gg A_k, B_k$, a condition which is still satisfied even at low field.

Finally, we introduce the microwave irradiation $\hat{H}_{\mathrm{mw}} = \omega_{1\mathrm{S}}\hat{S}_{\mathrm{x}}$ (in the electron rotating frame, to be transformed via $\hat{U}$) to calculate the transition amplitude for each transition

$$a_{ij} = \left\langle \psi_i^{\wedge} \middle| \hat{U}\omega_{1\mathrm{S}}\hat{S}_{\mathrm{x}}\hat{U}^{-1} \middle| \psi_j^{\wedge} \right\rangle \tag{4.6}$$

where $\left|\psi^{\wedge}\right\rangle$ are the eigenstates of $\hat{H}^{\wedge}$. For the TSSE, these are

$$a_{\mathrm{TQ}} = a_{\mathrm{SQ}} \approx \frac{B_1 B_2 \omega_{1\mathrm{S}}}{8\omega_{0\mathrm{I}}^2} \tag{4.7}$$

while for the SE these are

$$a_{k,\mathrm{DQ}} = -a_{k,\mathrm{ZQ}} = \frac{B_k \omega_{1\mathrm{S}}}{4\omega_{0\mathrm{I}}} \tag{4.8}$$

where we have made the assumption $\omega_{0\mathrm{I}} \gg A_k, B_k, \omega_{1\mathrm{S}}$. The transition probabilities, using Fermi's golden rule, are then

$$\begin{aligned} P_{ij} &= \left|a_{ij}\right|^2 \\ P_{\mathrm{SE}} &= \frac{B^2\omega_{1\mathrm{S}}^2}{16\omega_{0\mathrm{I}}^2} \\ P_{\mathrm{TSSE}} &= \frac{B_1^2 B_2^2 \omega_{1\mathrm{S}}^2}{64\omega_{0\mathrm{I}}^4}. \end{aligned} \tag{4.9}$$

Here we see the increased sensitivity of the TSSE to the magnitudes of the hyperfine couplings that we have alluded to, as well as the field dependence $\omega_{0\mathrm{I}}^{-4}$, as opposed to the $\omega_{0\mathrm{I}}^{-2}$ of the two-spin SE. The field dependence explains why previous studies have only observed small TSSE enhancements.

4.1.2 Results and discussion

Hyperpolarization of the bulk ^{1}H nuclei was observed at both the SE and TSSE conditions in enhancement profiles of both trityl OX063 and Finland trityl radicals, plotted in

Figure 4.1A. The enhancement for OX063 is ∼±220 for the SE and ∼±100 for the TSSE with $\omega_{1S}/2\pi = 2$ MHz and a polarization build-up time 8 s.

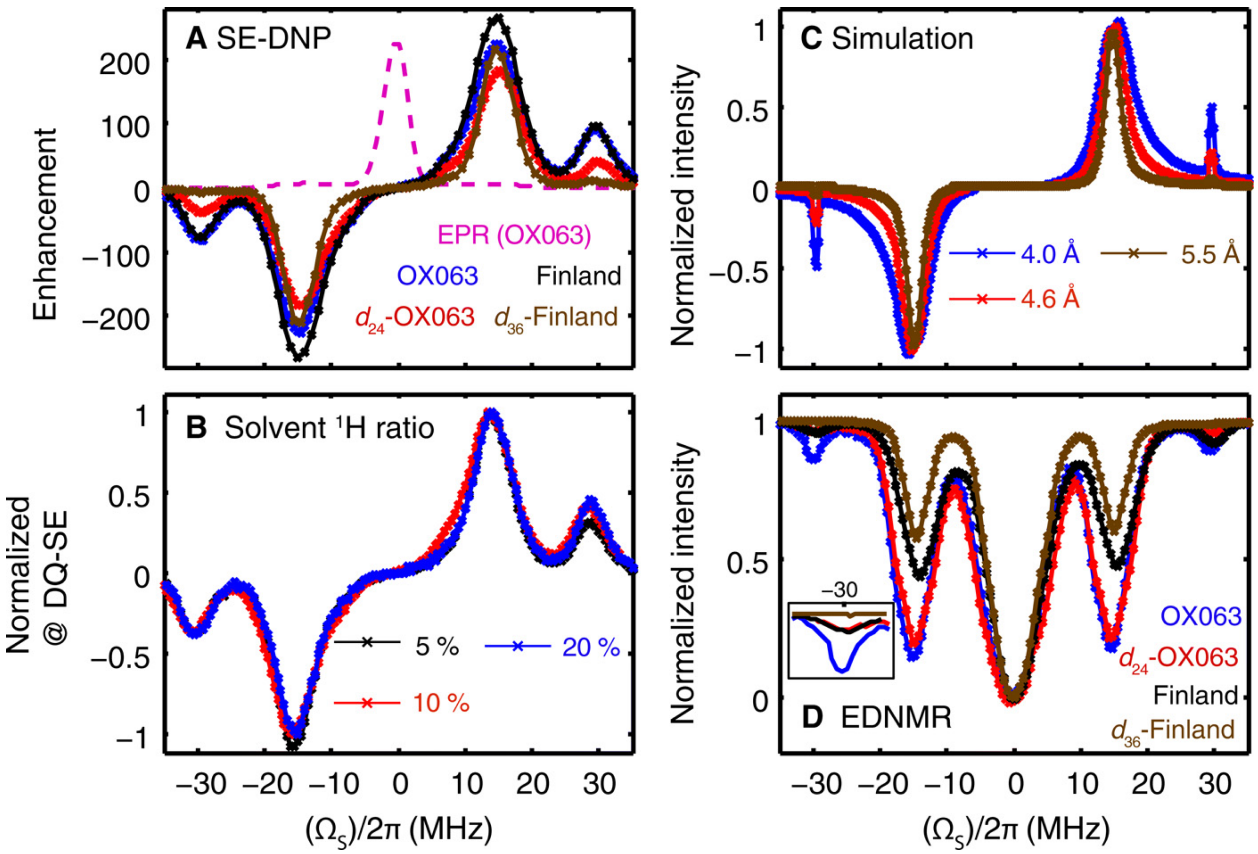

Figure 4.1: (A–C): DNP enhancement profiles with $\omega_{1S}/2\pi = 2$ MHz and buildup time $\tau = 8$ s for (A) various trityl radicals, (B) trityl-OX063 with solvents of different H_2O ratios, and (C) three-spin simulations for different e^--^{1}H distances r_{eff}. (D): Normalized ELDOR (electron-electron double resonance)-detected NMR (EDNMR) using a saturating pulse length of 3 ms.

An initial hypothesis was that the TSSE essentially requires intramolecular protons by virtue of requiring two relatively strong hyperfine couplings B_1 and B_2. One experiment probing this is shown in Figure 4.1B, wherein the OX063 enhancement profile is measured for different levels of solvent deuteration. The effect of solvent deuteration is in principle complicated, changing the number of nuclei per radical and also affecting spin diffusion, but by normalizing the enhancements to those at the two-spin SE condition we can see if the solvent deuteration impacts the TSSE more than the SE. Specifically, if the SE depends on the probability p that a nucleus is close to the radical (to have

a sufficient B value for an observable enhancement), then the TSSE depends on p^2; if those nuclei are coming from the solvent, then we should see the TSSE vary relative to the SE. That the TSSE enhancements, normalized to SE, are largely unchanged in Figure 4.1B implies that the TSSE is *not* mediated by the solvent protons, leaving only the intramolecular protons.

From another angle, we can use deuterated radicals to push the intramolecular protons further away from the radical center; in this case we should see a drop in the TSSE relative to the SE. Figure 4.1A shows enhancement profiles for d_{24}-OX063, which has the nearest 24 methylene $-CH_2$ groups deuterated, and d_{36}-Finland trityl, which has all intramolecular protons deuterated. In the case of d_{24}-OX063 the TSSE drops by 50% while the SE drops by only 18%, suggesting that the remaining protons on d_{24}-OX063 are close enough to enable the TSSE. In contrast, for d_{36}-Finland the TSSE is almost completely extinguished, in accordance with our hypothesis that the TSSE requires intramolecular protons.

To quantify the differences, we use numerical simulations of a three-spin system. The account for the large number of protons required for a realistic simulation (up to 48), we adopt the effective distance[108, 117, 118] $r_{\text{eff}} = (N/2)^{-1/6} \langle R \rangle$ where $\langle R \rangle$ is the average electron-nucleus distance of the N nuclei; the factor 2 is included as the simulation includes two protons rather than only one. Values of r_{eff} were obtained for three systems: OX063, d_{24}-OX063, and d_{36}-Finland. Protonated Finland was neglected as the methyl group dynamics are not included in the simulation model. For d_{36}-Finland, the value of 5.5 Å is intermediate among reported values for solvent protons in trityl systems[108, 119, 120], while we used an electronic structure calculation for the geometry and hyperfine couplings of trityl-OX063 to compute r_{eff} for OX063 and d_{24}-OX063; the values are reported in Table 4.1.

The simulation profiles are in Figure 4.1C and enhancements reported in Table 4.1; they show generally good agreement with experiment, but the TSSE lines are particu-

	OX063	d_{24}-OX063	d_{36}-Finland
$\langle R \rangle$ (Å)	5.98	6.96	5.5
N	24	24	2
r_{eff} (Å)	3.96	4.60	5.5
Expt. $\varepsilon_{\text{TSSE}}$	93	40	11
Expt. $\varepsilon_{\text{TSSE}}$ (re-norm.)	$93/93 = 1$	$40/93 \approx 0.43$	$11/93 \approx 0.12$
Sim. $\varepsilon_{\text{TSSE}}$ (norm.)	0.498	0.218	0.059
Sim. $\varepsilon_{\text{TSSE}}$ (re-norm.)	$0.498/0.498 = 1$	$0.218/0.498 \approx 0.44$	$0.059/0.498 \approx 0.12$

Table 4.1: Values of the parameter r_{eff} used and enhancement factors extracted from Figure 4.1. All "re-normalized" values are relative to the values for OX063 in the first column.

larly narrow. This may reflect that a more accurate simulation would need to include a distribution of hyperfine couplings and perhaps also relaxation parameters. With that said, the results overall support our hypothesis that the TSSE in trityl is mediated via intramolecular protons; polarization then diffuses to the observed bulk. That is, the protons and particularly the methylene $-CH_2$ protons in OX063 must be *outside* the spin diffusion barrier, or their polarization would not contribute the bulk. From the DFT calculations we take $\langle R \rangle$ to be ~6 Å for this group (Table 4.1), concluding that the radius of the spin diffusion barrier must be less than 6 Å. This is in agreement with a 2017 study on a series of vanadyl complexes which used EPR relaxation times to place the spin diffusion barrier between 4 and 6 Å[121] and a 2021 study which used hyperpolarization resurgence (HypRes) experiments to demonstrate that nuclei as close as 3 Å, "hidden" from the bulk signal, can still exchange polarization with the bulk nuclei and thus contribute to the observed signal[122].

As an additional verification of the DNP enhancement profile, we performed ELDOR (electron-electron double resonance)-detected NMR (EDNMR) experiments (Figure 4.1D). EDNMR[123] is essentially a DNP enhancement profile but rather than monitor the increase in nuclear polarization via the NMR signal, one monitors the decrease in electron polarization via the EPR signal at $\Omega_S = 0$, hence the need for two microwave frequen-

cies. In principle, any gain we see in the nuclear polarization must be compensated by a loss of electron polarization. Alternatively, a loss of electron polarization without concomitant enhancement in the DNP profile suggests the presence of nearby "hidden" nuclei, or at least that the rate of polarization transfer via DNP severely outpaces the rate of spin diffusion to the bulk.

Finally, we sought to determine which solvent nuclei were more likely to be involved in the TSSE and spin diffusion. We recorded ^{1}H ENDOR (electron nuclear double resonance) spectra of d_{36}-Finland trityl in three different solvents: our standard 6:3:1 (vol.) glycerol-d_8:D_2O:H_2O, 6:4 (vol) glycerol-h_8:D_2O, and 6:4 (vol) glycerol-h_8:H_2O, shown in Figure 4.2. Most notably, the presence of protonated glycerol renders the full width at half maximum about twice as broad, indicating that the glycerol $-CH_2$ groups couple more strongly, i.e., get closer, to the radical center. That is, the glycerol molecules (deuterated in most experiments) may do a better job solvating the radical molecule and partially prevent the water protons from being polarized directly.

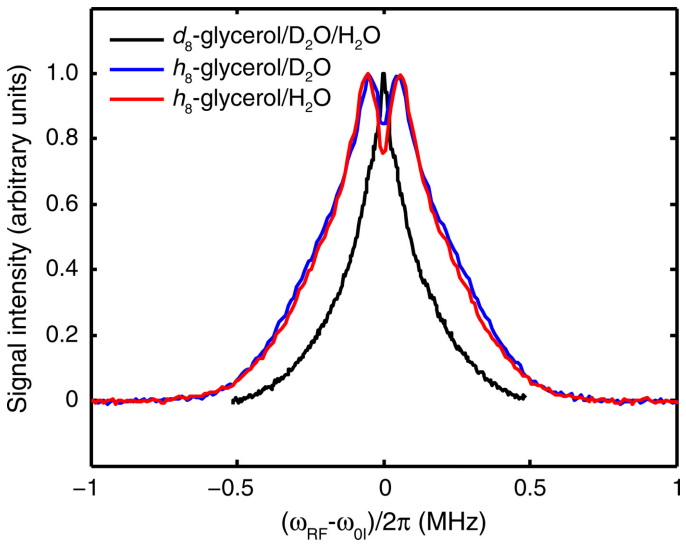

Figure 4.2: Normalized ^{1}H ENDOR spectra at 80 K recorded on 0.5 mM d_{36}-Finland trityl in 6:4 (vol.) glycerol:water mixtures with either deuterated or protonated components. The mixtures are 6:3:1 (vol.) glycerol-d_8:D_2O:H_2O (black), ^{1}H glycerol with 99.9% D_2O (blue), and ^{1}H glycerol with 99.9% H_2O (red).

If we interpret full width of the ENDOR line at the base of the peak (1% of the max-

imum intensity) as the parallel principal value of a dipolar coupling tensor between the most strongly coupled solvent proton and the radical, we can estimate the closest possible distance that a solvent proton can approach the radical. For 6:3:1 (vol.) glycerol-d_8:D_2O:H_2O, our standard matrix, that width is $\sim$0.9 MHz which yields an estimated lower limit of 5.6 Å. These might indeed be closer than some intramolecular protons, but these also represent a tiny fraction of the total number of solvent nuclei, insufficient for a reasonable TSSE enhancement (and matching our observations for d_{36}-Finland in Figure 4.1A).

4.1.3 Materials and methods

Sample preparation

Four trityl radicals, OX063, deuterated d_{24}-OX063, Finland[124], and perdueterated d_{36}-Finland were obtained from GE Healthcare (Amersham, UK). Samples of 5 mM trityl were prepared in 6:3:1 (vol.) glycerol-d_8:D_2O:H_2O, with the exception of the solvent deuteration analysis (Figure 4.1B) and the ENDOR measurements (Figure 4.2) which used a concentration of 0.5 mM.

DNP-NMR and EPR spectroscopy

Experiments were conducted at temperatures of 80 K and $B_0 = 0.35$ T on a Bruker ElexSys E580 X-band EPR spectrometer equipped with an ENDOR probe containing a dielectric microwave resonator. NMR signals were acquired using an iSpin-NMR system (SpinCore Technologies, Inc., Gainesville, FL); the pulse sequence was a saturation recovery followed by signal measurement with a solid echo, with microwave irradiation during the recovery period τ. EDNMR experiments were conducted with a high-turning angle pulse length of 3 ms and with a Rabi frequency of 2 MHz. Mims ENDOR experiments used 25 W RF pulses of length 160 µs to excite NMR transitions, and the sequence delay

$d = 300$ ns was chosen so blind spots in the ENDOR spectrum would occur well outside the range of couplings observed.

DFT calculations

The OX063 starting geometry for the DFT calculations was generated with Avogadro[125]. The structure was optimized using the ORCA package[126] with methods previously found to be reasonable for structural optimizations of trityl radicals[119] (DFT, B3LYP functional, 6-31G basis set, RI approximation for Coulomb integrals with def2/J auxiliary basis). The final optimized structure is shown in Figure 4.3. From there, we used the Gabedit software[127] to set up a single-point calculation at the optimized structure using the same functional but with the IGLO-III basis set[128, 129], which is tailored for calculation of EPR parameters, to calculate the ^{1}H hyperfine couplings. This set of methods has been shown to provide reasonably accurate ^{1}H hyperfine coupling calculations in main-group radicals[130]. For the purpose of the calculations, we treated carboxyl groups as protonated rather than associated with Na^+ or other counterion. From each computed hyperfine coupling tensor, the isotropic component was subtracted and the resulting traceless tensor was converted to a distance assuming a point-dipole interaction. Finally, we calculated the mean electron-nuclear distance for 1) the 24 proximal CH_2 protons in the R groups, which we report as $\langle R \rangle$ for fully protonated OX063, and 2) the distal CH_2 protons in the R groups for d_{24}-OX063. The individual protons are listed in Table 4.2 for protonated OX063 and in Table 4.3 for d_{24}-OX063, where the numbers refer to the atom number in the structure and can be compared to the `.xyz` file available in the Supporting Information of Tan et al.[114] and the electron spin densities (not used, but perhaps informative) are calculated using the Mulliken population analysis.

Proton #	Spin Density	A_{iso} (MHz)	d (MHz)	r (Å)
49	3.1E−4	0.0230	0.862	4.51
50	−1.1E−4	0.217	0.402	5.82
57	−4.1E−4	0.0280	0.328	6.22
58	−7.5E−5	−0.105	0.224	7.06
66	−7.4E−5	−0.154	0.226	7.04
67	2.8E−5	0.0470	0.307	6.36
71	−4.1E−4	−0.0320	0.785	4.65
72	−3.6E−4	0.394	0.531	5.30
79	−5.2E−4	−0.003 00	0.638	4.99
81	4.5E−4	0.0170	0.282	6.55
85	4.1E−5	0.0180	0.309	6.35
87	−9.3E−5	0.0170	0.316	6.30
91	1.3E−4	−0.0560	0.743	4.74
92	−1.9E−4	0.0770	0.444	5.63
97	−2.0E−4	−0.003 00	0.297	6.44
98	−3.3E−5	−0.108	0.206	7.27
107	−1.0E−4	0	0.529	5.31
108	2.5E−5	−0.0920	0.267	6.67
113	8.0E−5	0.0880	0.353	6.07
114	−7.5E−5	−0.0260	0.326	6.23
121	2.3E−4	0	0.699	4.84
122	−1.5E−4	0.112	0.471	5.51
128	−3.6E−5	−0.0650	0.205	7.28
129	1.1E−5	0.0150	0.283	6.54

Table 4.2: Electron spin densities, hyperfine couplings, and distances from the DFT calculation for the proximal CH_2 protons in the trityl OX063 molecule.

Proton #	Spin Density	A_{iso} (MHz)	d (MHz)	r (Å)
52	−1.7E−4	−0.0320	0.232	6.98
53	9.6E−5	0.001 00	0.238	6.93
59	2.4E−5	−0.0500	0.366	6.00
61	−1.2E−5	0.009 00	0.286	6.51
68	−3.8E−4	−0.006 00	0.315	6.31
69	2.2E−5	−0.0180	0.180	7.60
74	−2.3E−4	0.120	0.219	7.12
76	3.6E−5	0.006 00	0.202	7.31
82	2.8E−4	0.0260	0.590	5.12
83	3.2E−5	0.0500	0.273	6.61
89	1.5E−5	0.005 00	0.161	7.89
90	2.1E−5	0.0440	0.130	8.47
94	−1.5E−4	0.0870	0.217	7.14
96	1.9E−5	0.0550	0.182	7.57
100	0.00	−0.006 00	0.262	6.70
102	−3.0E−6	0.0120	0.173	7.71
110	−1.4E−4	0.0540	0.61	5.06
111	5.9E−5	0.0410	0.289	6.49
116	9.9E−5	−0.0110	0.159	7.93
118	−9.0E−6	0.009 00	0.157	7.96
124	−1.3E−4	0.0720	0.202	7.31
126	−1.9E−5	0.0120	0.180	7.61
130	−1.9E−4	−0.0320	0.259	6.73
132	1.2E−4	0.0250	0.368	5.99

Table 4.3: Electron spin densities, hyperfine couplings, and distances from the DFT calculation for the proximal CH_2 protons in the d_{24}-OX063 molecule.

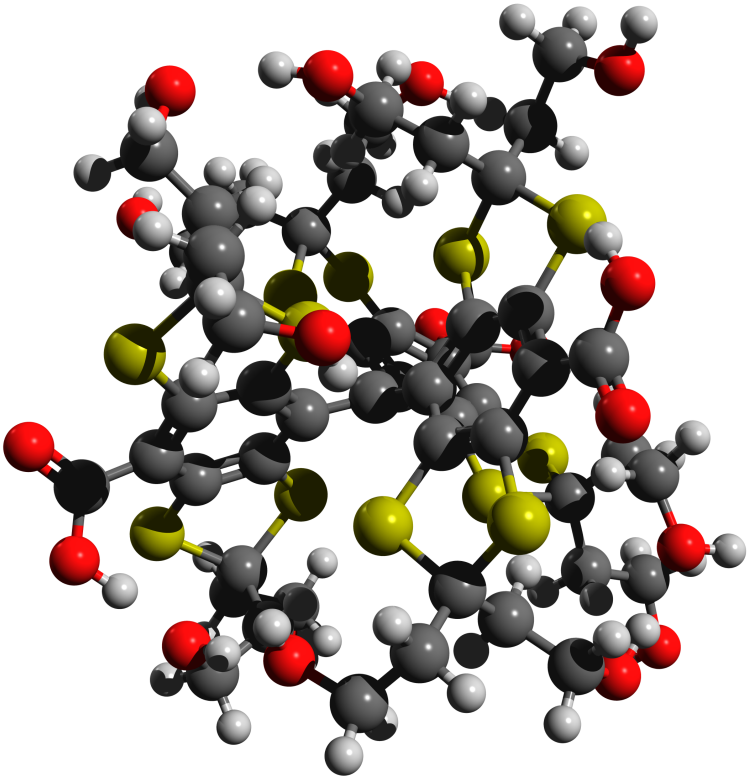

Figure 4.3: Optimized structure of trityl OX063 from DFT calculations.

Numerical simulations

Numerical simulations were performed using MATLAB (MathWorks) code previously used for simulation of TOP-DNP[55]. The electron g-tensor had principal values [2.0040, 2.0038, 2.0036], and the Euler angles for the g-tensor and the two hyperfine coupling tensors are set to $[0°, 40°, 0°]$, $[0°, 0°, 0°]$, and $[30°, 90°, 70°]$ respectively. Relaxation was incorporated via relaxation operators in Liouville space[131], with relaxation times $T_{1e} = 0.6$ ms and $T_{2e} = 5$ µs for the electron and $T_{1n} = 13$ s and $T_{2n} = 1$ ms for both of the ^{1}H nuclei. The relaxation superoperators have the form $\hat{\hat{\Gamma}}\hat{\sigma} = \sum_{\chi=x,y,z} k_\chi \left[\hat{S}_\chi \left[\hat{S}_\chi, \hat{\sigma}\right]\right]$, where σ is the density operator and k_χ incorporates the relaxation rates.

4.1.4 Conclusions

A large enhancement for a higher-order solid effect was observed at 0.35 T and 80 K. A theoretical analysis and subsequent investigation via experiment and simulation showed that the TSSE is sensitive to the radical structure and particularly the electron-^{1}H distance. We demonstrated that TSSE is mediated by intramolecular protons, and used electronic structure calculations to more specifically identify the electron-proton distance, placing an upper bound of 6.0 Å on the size of the spin diffusion barrier for trityl in glycerol-water. This was the first direct measurement of the spin diffusion barrier for a bulky organic radical in a glassy matrix. We also show ENDOR results demonstrating that the protons in glycerol molecules in the matrix are much closer to the trityl radical center than the water protons, suggesting that these glycerol molecules are involved in spin diffusion from the radical to the bulk.

Further development of DNP will rely on understanding not only the direct DNP dynamics but also critical factors leading to observable polarization including spin diffusion pathways. Trityl is unique among stable free radicals currently employed for DNP due to the high degree of electron localization and the lack of strongly hyperfine-coupled protons: investigations of how spin diffusion differs for other polarizing agents such as BDPA and nitroxides will offer interesting comparisons and potential insights for the design of new radicals and experiments.

4.2 Resonant mixing

Conventionally, e.g. in the DNP enhancement profiles of Figure 4.1A, trityl radicals are considered a SE polarizing agent for ^{1}H in solids, especially under MAS[85]. As a narrow-line radical, trityl-OX063 has also been used to demonstrate pulsed DNP mechanisms at fields $<$3.4 T[55, 56, 132, 133]. Its linewidth is apparently sufficient to support either a cross effect (CE) or thermal mixing (TM) mechanism to ^{2}H, with its lower nuclear Lar-

mor frequency, at 5 T[134]. Interestingly, ^{1}H DNP has been reported even with microwave irradiation near the EPR frequency[75, 97], an unexpected result assuming only the SE should be active. When Equbal et al.[97] investigated the central dispersive profile, they observed a maximum enhancement over 100 at 7.4 T, 20 K, and for a static sample. With pump-probe ELDOR experiments, they identified an asymmetrically broadened EPR line and electron hyperpolarization as hallmarks of TM. Borghini et al.[115] made similar observations for BDPA 2.5 T and 0.7 K and also explained the feature as TM.

We investigate the ^{1}H DNP mechanisms exhibited by trityl OX063 and the partially deuterated OX071 (i.e., d_{24}-OX063) under MAS at several radical concentrations. The impacts of different cryoprotectant matrices are probed by studying samples in both glycerol and DMSO. Finally, we use multinuclear NMR, comparing the hyperpolarization of ^{1}H, ^{2}H, and ^{13}C, to directly test for the presence of a densely coupled electron network. An unexpected observation of spontaneous double-quantum transfer between ^{1}H and ^{13}C nuclei and subsequent characterization leads us to conclude that TM is not the dominant mechanism leading to ^{1}H hyperpolarization in the center of the trityl enhancement profile. To explain the mechanism, we propose a new DNP mechanism termed “resonant mixing.”

We derive the Hamiltonian for the mechanism, mediated by state mixing of microwaves and hyperfine interactions. We further investigate it high fields, and suggest that RM can explain the observed trityl data without the potentially unphysical requirements to observe TM.

4.2.1 DNP at 8.9 T

For this section, DNP experiments were performed on an 8.9 T DNP spectrometer equipped with a frequency-swept solid-state microwave source generating 160 mW of microwave power as well as frequency-tunable gyrotron operated at 5 W of output power. Unless otherwise stated, the experiments used samples packed in 4 mm sapphire rotors spin-

ning at $\omega_r/2\pi = 6$ kHz and at 100 K.

The ^{1}H DNP enhancement profiles of trityl-OX063 in 6:3:1 (vol.) DMSO-d_6:D_2O:H_2O at different concentrations in the range of 20 to 100 mM are shown in Figure 4.4A. The saturation recovery times for both microwave on and off experiment were set to $3 \cdot T_1$ (times in figure). DNP buildup times T_B at 249.70 GHz (SE maximum) and 250.05 GHz (center profile maximum) were similar to T_1 for all concentrations. With the modest incident microwave power from the solid-state source, the SE enhancements are also predictably modest, with a maximum enhancement of $\sim$1. The maximum SE enhancement occurs at a concentration of $\sim$60 mM, in contrast to a previous study for static samples at 20 K with 350 mW incident microwave power, where the SE enhancement began to drop at only $\sim$20 mM[97]. The concentration at which this inflection point is likely due to both the relaxation parameters and the incident microwave power, among other factors.

The central feature in the profile, corresponding to direct excitation of the EPR transitions of the radical, grows in intensity with increasing concentration. The shape appears distinctly asymmetric in contrast to prior observations on static samples; we might ascribe it as a superposition of an absorptive component and a dispersive component. In reference to the concentration, the dispersive component scales more strongly, as we see the magnitude of the negative peak quickly increase relative to that of the positive peak at the higher concentrations. Scaling with concentration appears to suggest the manifestation of electron-electron interactions, and indeed trityl-OX063 is known to aggregate in solution, forming dimers even at a concentration as low as 2 mM[135].

Seeking to ascertain the role of the glassing agent, which should be a large contributor to any propensity of trityl to form dimers and other multi-electron clusters, we performed a similar study of the concentration dependence in 6:3:1 (vol.) glycerol-d_8:D_2O:H_2O (DNP juice). The results are shown in Figure 4.4B. The SE remains the same, in regards to the turning point appearing at 60 mM. However, the behavior of the central feature is different: a higher concentration of the radical in glycerol was needed

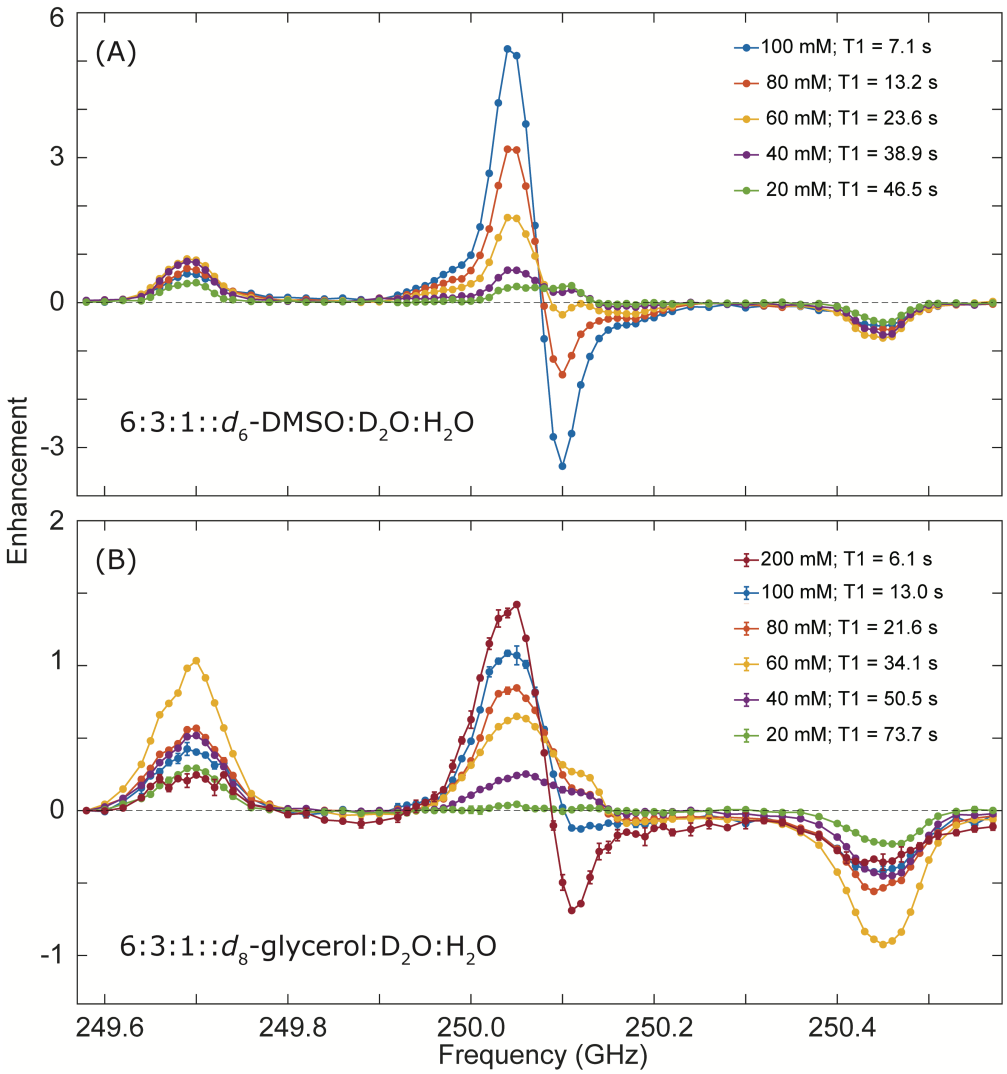

Figure 4.4: Experimental ^{1}H DNP enhancement profiles of glassing matrices (A) 6:3:1 (vol.) DMSO-d_6:D_2O:H_2O and (B) 6:3:1 (vol.) glycerol-d_8:D_2O:H_2O doped with different concentrations of trityl OX063, obtained with 160 mW of microwave irradiation at 100 K, $\omega_r/2\pi = 6$ kHz.

to produce a profile similar to that obtained in DMSO. This observation also manifests in the spin-lattice relaxation times. If the central feature is a consequence of radical aggregation, then it is evident that such aggregation is more prone to happen, at lower concentrations, in DMSO- rather than glycerol-based matrices. Alternatively, there may be more general differences in relaxation parameters for these two systems, which could plausibly explain the different observed profiles.

We decided to introduce a more direct study of the effect of aggregation by preparing two 10 mM samples of trityl OX063 in DNP juice: one prepared directly at 10 mM and the other initially prepared at 100 mM and subsequently diluted. We compared the DNP enhancement profiles, shown in Figure 4.5. The SE enhancement is reproducibly lower for the diluted sample compared to the natively prepared sample, suggesting that the aggregation induced by the higher concentration is not easily resolved by dilution. The SE primarily occurs to intramolecular nuclei and a small percentage of bulk nuclei which can get very close to the radical. Assuming the diluted sample has a larger number of clustered radicals, we can understand the effect on the SE in two ways. First, the ^{1}H spins near these clustered radicals are highly shifted and experience very rapid paramagnetic relaxation, more so than near an isolated radical molecule. That is, these protons, even if they are polarized via the SE, are less efficient at contributing that polarization to the bulk via spin diffusion – an extreme case would be that more of these nuclei are actually *in* the larger spin diffusion barrier of these aggregates. Second, as each cluster of radicals effectively acts like a single electron, there is a lower effective concentration of DNP sources, lowering the amount of polarization the electrons can contribute. This latter point is also supported in the nuclear spin-lattice relaxation times T_1 for these systems: (67.6 ± 1.1) s for the natively prepared sample and (74.9 ± 2.2) s for the diluted sample – the bulk nuclei, which do not experience the rapid relaxation the intra-cluster nuclei do, only see the lower effective radical concentration and thus exhibit (modestly) longer relaxation times. The central profile does not change nearly as dramatically as

the SE region. At face value, we might interpret this result as suggesting that the mechanism of polarization transfer active for this central profile neither requires a radical cluster nor is it majorly inhibited by their presence. But, we must also consider that the enhancements are quite low, and any actual differences might simply be too small to resolve.

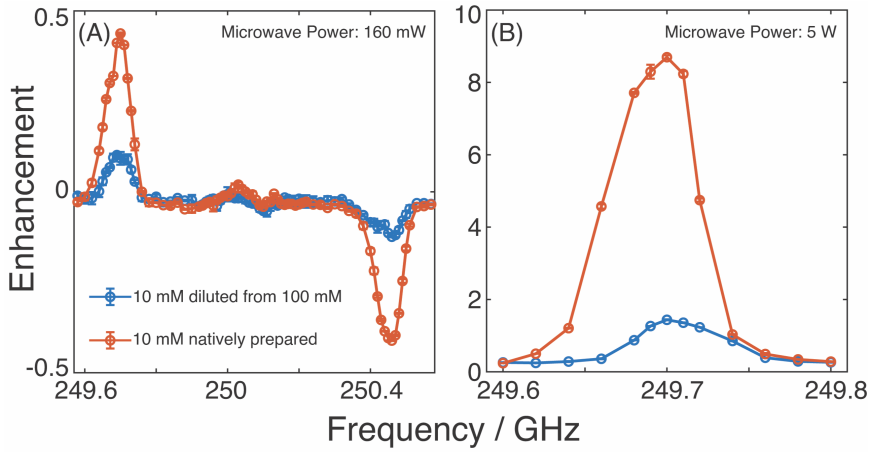

Figure 4.5: Experimental ^{1}H DNP enhancement profiles of 10 mM trityl-OX063 in DNP juice, prepared directly at 10 mM (red) and diluted from a 100 mM stock solution (blue). (A): Profiles collected with 160 mW microwave irradiation. (B): Profiles near positive SE region collected with 5 W microwave irradiation from the gyrotron.

For the central profile to be due to CE, then the EPR linewidth of trityl OX063 must encompass the ^{1}H Larmor frequency, which in our case is 380 MHz. Lumata et al.[107] reported a field-swept EPR spectrum of 15 mM trityl-OX063 at 100 K at 8.6 T/240 GHz, quite close to our field. Their spectrum has a full-width at the base of the lineshape of at most 170 MHz, much less than the ^{1}H Larmor frequency. We measured the field-swept EPR spectrum of 80 mM trityl OX063 at 5 T/140 GHz (plotted in Figure 4.6); we observed a linewidth of 110 MHz, again less than the ^{1}H Larmor frequency of 211 MHz at this field. TM can be supported for an EPR line with homogeneous broadening $D < \omega_{0I}$, but not too small[136] – the minimal increase in linewidth from 8 to 80 mM in Figure 4.6 suggests that the homogeneous linewidth due to the presence of multielectron clusters is still small here. Moreover, as the dipolar couplings among electrons are field-independent, we

expect D to be an even smaller fraction of ω_{0I} at 380 MHz and higher.

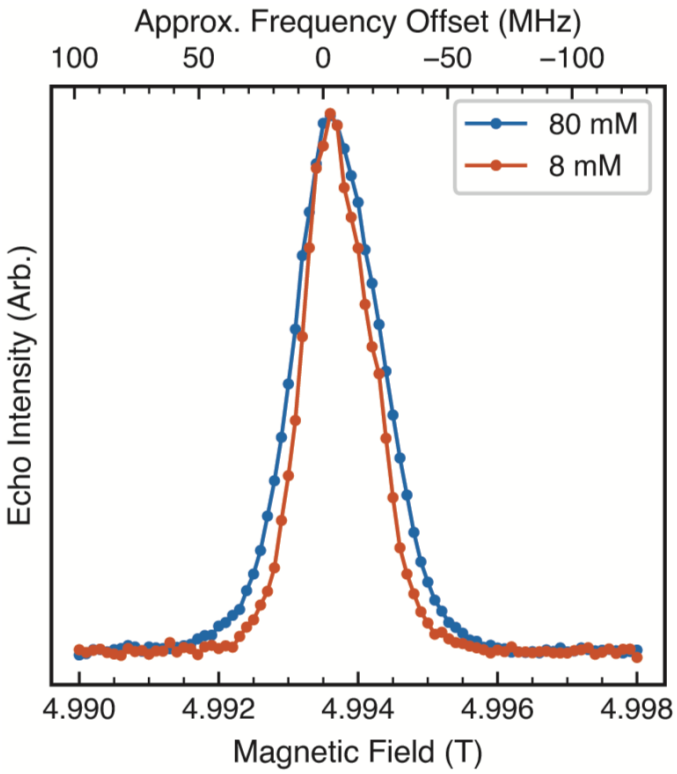

Figure 4.6: Echo detected EPR field profiles collected at 5 T/140 GHz of 80 and 8 mM trityl-OX063 in 6:3:1 (vol.) DMSO-d_6:D_2O:H_2O. Spectra were collected by observing the Hahn echo intensity at each field point, with pulse lengths of 25 and 50 ns, an interpulse delay of 200 ns, a repetition rate of 1 kHz, a constant microwave frequency of 139.997 GHz, and the sample temperature maintained at 80 K.

To determine the origin of the dispersive central profile, we first tested the hypothesis that the DNP enhancement of ^{2}H nuclei, whose Larmor frequency comfortably fits within the EPR linewidth of OX063, is relayed to ^{1}H nuclei via the strongly coupled electron network at high radical concentrations. The hypothesis was based on the observation that the two lobes of the central feature in the ^{1}H DNP profile are approximately $2 \times \omega_0^{2H}$ separated from one another. To test this, we performed two experiments: 1) we applied a train of ^{2}H saturation pulses during the ^{1}H buildup time in the 80 mM sample dispersed in deuterated DMSO and still observed the same dispersive central feature in the ^{1}H frequency profile (data not shown), and 2) we prepared a sample of 80 mM trityl-OX063 in a fully protonated DMSO matrix, i.e. 6:4 (vol.) DMSO-h_6:H_2O, and again

still observed the dispersive feature in the frequency profile (Figure 4.7). Of course, in the protonated matrix there is a larger ratio of ^{1}H:electron spins, so the enhancement is lower, but the existence of the central profile under these conditions rules out the possibility of relayed transfer from ^{2}H spins, as none are present in the sample.

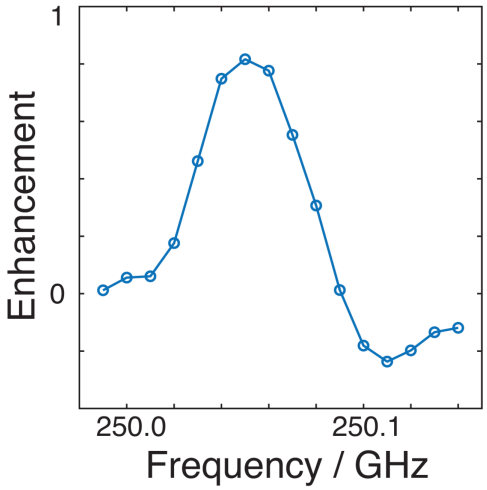

Figure 4.7: ^{1}H DNP frequency profile of 80 mM trityl-OX063 in 6:4 (vol.) DMSO-h_6:H_2O.

To more directly probe the TM mechanism, we collected enhancement profiles of multiple nuclei (^{1}H, ^{13}C, and ^{2}H) both with the 160 mW source and the gyrotron operating at 5 W; the profiles are plotted in Figure 4.8. These samples were prepared in a DMSO-d_6 matrix with a fraction of $^{13}C_3$-glycerol to serve as a ^{13}C probe. The first sample once again employed 80 mM trityl-OX063 as the polarizing agent, in Figure 4.8(a,c,e). For ^{1}H, the enhancement at the central profile in Figure 4.8(a) increases only marginally with additional power. In contrast, the ^{1}H SE increases from ~1.5 to 10. A similar result is observed for ^{13}C DNP in Figure 4.8(c): the CE/TM enhancement at 250.04 GHz is largely the same at both powers, while the SE enhancement at 249.98 GHz increases from ~20 to 160. The ^{2}H profile in Figure 4.8(e) exhibits unresolved CE/TM and SE effects and overall weak enhancement compared to ^{13}C, likely owing to the high molar concentration of ^{2}H spins per electron in the sample.

We also collected profiles of the same three nuclei with 80 mM trityl-OX071, a partially

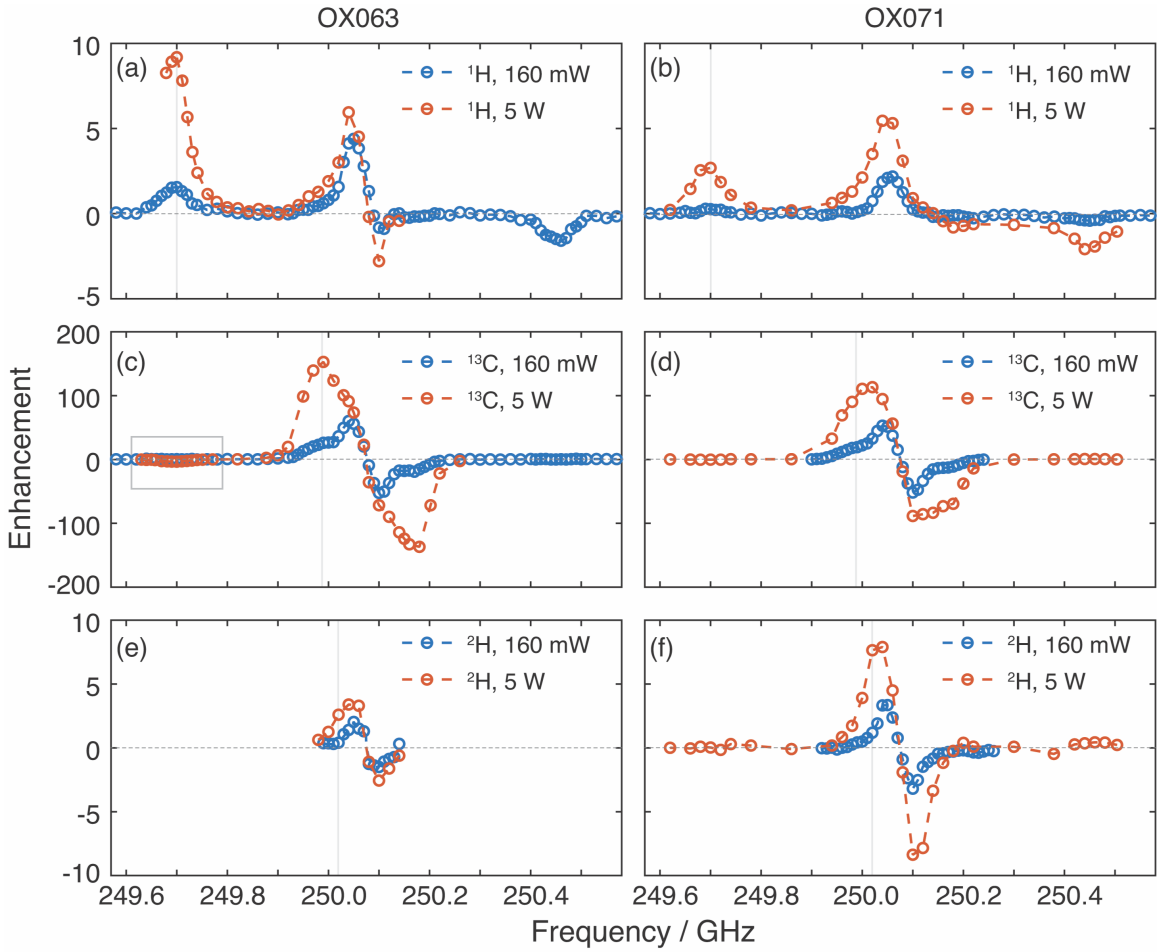

Figure 4.8: Experimental ^{1}H (a–b), ^{13}C (c–d), and 2 H (e–f) DNP frequency profiles of trityl-OX063 (a,c,e) or trityl-OX071 (b,d,f) at 80 mM concentration in 4:2:3:1 (vol.) DMSO-d_6:$^{13}C_3$-glycerol:D_2O:H_2O. The vertical gray lines indicate the microwave frequency satisfying the positive SE condition for the corresponding nucleus. The gray box in (c) indicates the NOE experienced by ^{13}C nuclei at the ^{1}H SE condition.

deuterated analog (referred to as d_{24}-OX063 in Section 4.1), in the same 4:2:3:1 (vol.) DMSO-d_6:$^{13}C_3$-glycerol:D_2O:H_2O matrix. These will help resolve the DNP effects due to nuclei on the radical and those in the matrix surrounding it; the profiles are plotted in Figure 4.8(b,d,f). In Figure 4.8(b), the SE enhancement is attenuated by a factor of $\sim$3 compared to OX063 in (a), owing to the direct dependence of the SE on the number and strength of hyperfine couplings between the radical center and the surrounding spins. However, the central feature is still present and comparable to that of the OX063 sample – this enhancement must occur substantially via ^{1}H spins in the surrounding matrix. The ^{13}C enhancement in Figure 4.8(d) shows comparable enhancements for both the CE/TM and SE conditions, unlike for OX063 in (c) where the SE was stronger. At similar radical concentrations, the two samples should exhibit largely similar DNP profiles since the deuterated radical in principle has no effect for direct ^{13}C DNP. The observed difference could be due to a slight difference in true radical concentration due to degradation over time – UV-vis spectroscopy indicated that the active radical concentration was about 10% lower in the somewhat older OX071 sample. The ^{2}H DNP profile in Figure 4.8(f) exhibits stronger enhancements than for OX063 in (e), as expected now that the radical has intramolecular ^{2}H nuclei. The central profiles of all three nuclei have their positive and negative lobes separated by about 60 MHz, perhaps an indication of TM but overall hard to rationalize.

A further interesting observation is that of the direct ^{13}C DNP enhancement upon strong microwave irradiation at the ^{1}H SE condition, highlighted by the gray box in Figure 4.8(c). The ^{13}C nuclear enhancement was -3 under a ^{1}H SE enhancement of +10 – a striking result as the thermodynamic argument of TM generally suggests that the electron network is in thermal contact with the different nuclear spins. That is, under TM all nuclear spins tend towards the same spin temperature (defined as the temperature at which the polarization would be at thermal equilibrium given the local field). The expanded profile is shown in Figure 4.9(A), and ^{13}C spectra with and without microwave

irradiation at 249.7 GHz are shown in Figure 4.9(B). This is not a three-spin solid effect involving electron-^{1}H-^{13}C, which would occur around 249.8 GHz ($\Omega \approx -\omega_0^{1H} + \omega_0^{13C}$). In the OX071 sample the ^{13}C enhancement at this condition is about -1, consistent with the lower ^{1}H SE.

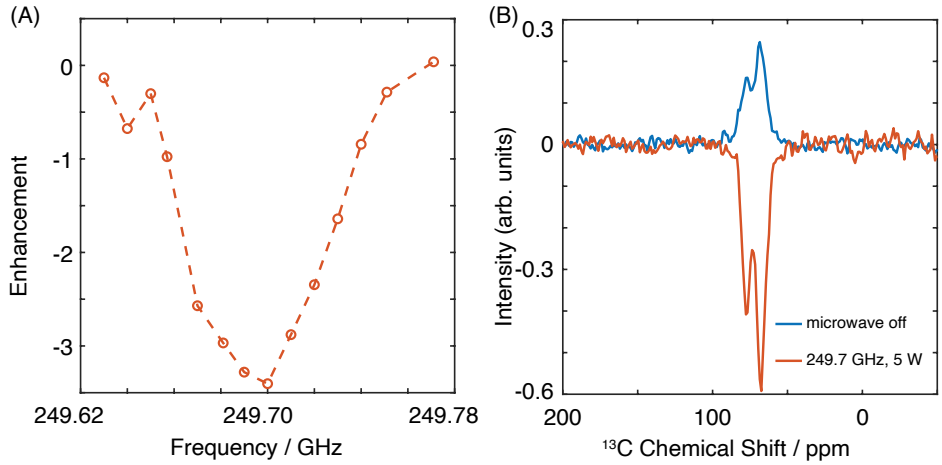

Figure 4.9: (A) Experimental ^{13}C enhancement when irradiated about the ^{1}H SE condition. (B) The ^{13}C sepctra with and without microwave irradiation at the ^{1}H SE condition. The sample is 80 mM trityl-OX063 in 4:2:3:1 (vol.) DMSO-d_6:$^{13}C_3$-glycerol:D_2O:H_2O.

Again, the negative enhancement of ^{13}C spins here is not consistent with a strongly coupled electron network equilibrating the spin temperatures of the ^{1}H and ^{13}C nuclear spin reservoirs – ^{1}H and ^{13}C have the same sign gyromagnetic ratio, so both should exhibit the same sign of enhancement. To investigate this, we performed the experiment shown in Figure 4.10(A) where during the ^{13}C buildup, the ^{1}H nuclear spins are saturated with four pulses per ms. The sample was 50 mM trityl-OX063 in 4:2:3:1 (vol.) DMSO-d_6:$^{13}C_3$-glycerol:D_2O:H_2O. Without any microwave irradiation, the ^{13}C-glycerol signals are improved by 20% with ^{1}H saturation pulses, as seen by comparing Figure 4.10(B) and (C). In a separate experiment (data not shown) of the same matrix without *any* radical, the same effect is observed, proving that the communication between spins is independent of the electron network. The conditions of Figure 4.10(D), with microwave irradiation at the ^{1}H SE, mimic those of the previous experiments and reproduce the observed negative enhancement. When we also saturate the ^{1}H spins during the buildup period, the

negative enhancement is completely nullified (Figure 4.10(E)). These experiments prove that the negative ^{13}C enhancement is directly related to the ^{1}H spin polarization and does not rely on the electron network or microwave irradiation.

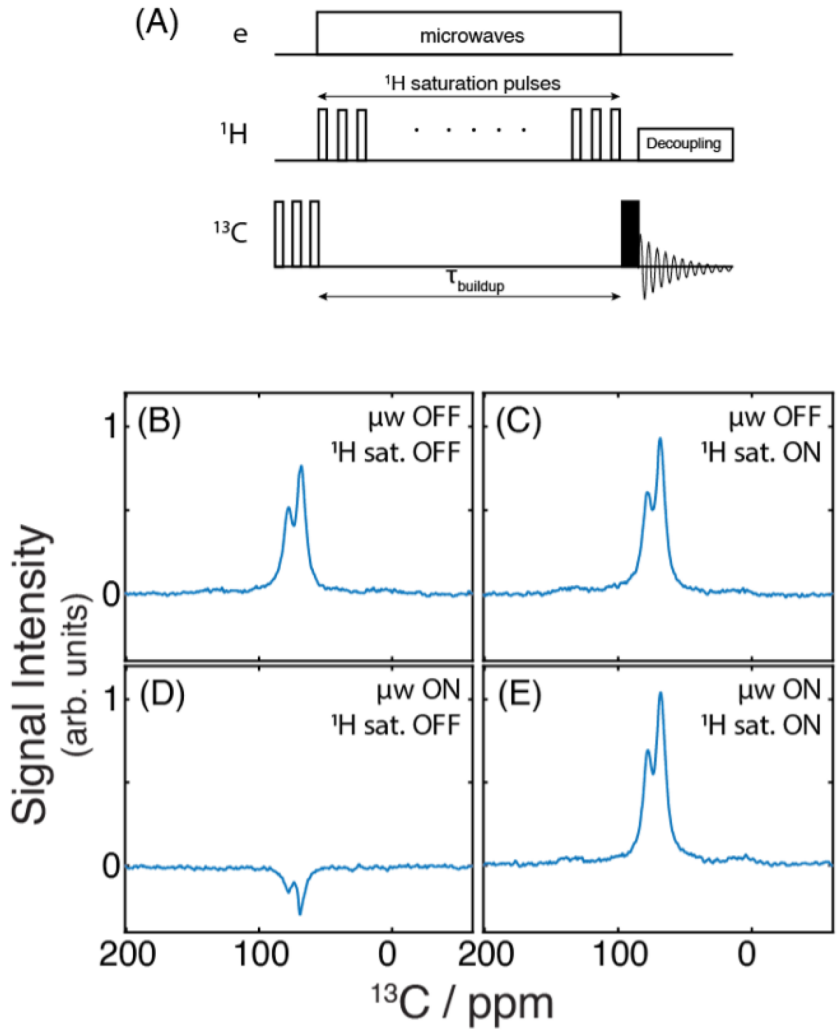

Figure 4.10: (A) Pulse sequence for the experiment establishing NOE between the ^{1}H and ^{13}C nuclei in the sample of 50 mM trityl-OX063 in 4:2:3:1 (vol.) DMSO-d_6:$^{13}C_3$-glycerol:D_2O:H_2O. The direct ^{13}C spectra showing glycerol carbons in (B) the absence of both microwave irradiation and ^{1}H saturation pulses, (C) without microwave irradiation but with ^{1}H saturation, (D) with microwave irradiation but without ^{1}H saturation, and (E) with both microwave irradiation and ^{1}H saturation.

The observation of a 20% improvement in the ^{13}C signal with ^{1}H saturation and that the ^{13}C polarization is negatively correlated to the ^{1}H signal rules out any electron network mediated TM effect as that would tend to equilibrate the spin temperatures, and

the polarizations would be positively correlated. We hypothesize the effect to be due to the nuclear Overhauser effect (NOE), which arises as a consequence of longitudinal cross-relaxation driven by random fluctuations of the ^{1}H-^{13}C dipolar interaction on the fast (nanosecond–picosecond) timescale. Such fast dynamics are commonly observed in liquids but rarely in solids where the dynamics are on the slow (second–millisecond) timescale. In solids it can be observed in the presence of methyl groups with fast dynamics (rotational hopping) about the C_3 axes[137–139], and has also been observed in solids without methyl motions[140]. These effects have been observed even under DNP conditions near 100 K with motions that include methyl rotation[141, 142], ring conformational exchange[143], and in surfactants both with and without methyl groups[144].

The hypothesis that the central dispersive feature in the ^{1}H DNP profiles of trityl can be attributed to TM is countered by the observations in Figure 4.10 – a strongly coupled electron network, required for TM, should equilibrate the spin temperatures of ^{13}C and ^{1}H. Moreover, we have seen evidence that the glycerol molecules, our primary source of ^{13}C nuclei in these samples, are able to approach the trityl radicals and even shield them from water molecules in the bulk (*vide supra*). Even at the ^{1}H SE condition, the proximity of all these spins to the potentially clustered radicals should lead to polarization exchange and spin temperature equilibration. However, a weak NOE which occurs independently of the electron network and the microwave irradiation still dominates in producing a negative enhancement of ^{13}C when ^{1}H nuclei are positively enhanced. This result calls into question the TM hypothesis for the central dispersive feature.

4.2.2 Theory of resonant mixing

At this point, dispersive DNP profiles had been observed at relatively high fields for trityl radicals by several groups[85, 89, 90, 97, 136, 145]. The types of strong electron-electron couplings required are unlikely in the case of trityl: trityl molecules are bulky, and the coupling between a pair of radicals cannot be much larger than about 50 MHz[135, 146].

Our previous observations have shown that even in concentrated samples, the spin temperature of ^{13}C is completely decoupled from that of ^{1}H, completely contrary to the conceptual picture of TM.

We rationalize these observations with a new mechanism termed resonant mixing (RM). The mechanism involves only a single electron spin, rather than any multielectron network, and the "resonant mixing" refers to the state mixing induced by microwave irradiation near the electron resonance frequency. The analytic treatment begins as follows: we consider the Hamiltonian of a coupled electron-nuclear spin pair under microwave irradiation and without relaxation in the electron rotating frame:

$$\hat{H} = \Omega_S \hat{S}_z + \omega_{1S} \hat{S}_x - \omega_{0I} \hat{I}_z + A_{zz} \hat{S}_z \hat{I}_z + \frac{1}{2} \hat{S}_z \left(A_{z-} \hat{I}_+ + A_{z+} \hat{I}_- \right) \tag{4.10}$$

where we have now split the pseudosecular part of the hyperfine interaction by the raising and lowering operators $\hat{I}_\pm = \hat{I}_x \pm i \hat{I}_y$. As before only the pseudosecular term will be needed – we can neglect the $A_{zz} \hat{S}_z \hat{I}_z$ term as it only results in slightly shifting the energies of the Zeeman states.

We can tilt the frame of reference for the electron spin operators by θ, with $\tan\theta = \omega_{1S}/\Omega_S$:

$$\hat{H}' = \omega_{\text{eff}} \hat{S}'_z - \omega_{0I} \hat{I}_z + \frac{1}{2} \left(\hat{S}'_z \cos\theta - \hat{S}'_x \sin\theta \right) \left(A_{z-} \hat{I}_+ + A_{z+} \hat{I}_- \right) \tag{4.11}$$

where the primes indicate operators in the tilted frame, and we have gone ahead and removed the secular hyperfine coupling. The matrix representation of the Hamiltonian using the basis states

$$|m_S, m_I\rangle = \{|1\rangle, |2\rangle, |3\rangle, |4\rangle\} = \left\{ \left| +\frac{1}{2}, -\frac{1}{2} \right\rangle, \left| -\frac{1}{2}, -\frac{1}{2} \right\rangle, \left| +\frac{1}{2}, +\frac{1}{2} \right\rangle, \left| -\frac{1}{2}, +\frac{1}{2} \right\rangle \right\} \tag{4.12}$$

of the z'-component of S' in the tilted rotating frame and the z-component of I in the

laboratory frame is:

$$\frac{1}{2}\begin{pmatrix} \omega_{\text{eff}}+\omega_{0\text{I}} & 0 & \frac{1}{2}A_{\text{z}+}\cos\theta & -\frac{1}{2}A_{\text{z}-}\sin\theta \\ 0 & -\omega_{\text{eff}}+\omega_{0\text{I}} & -\frac{1}{2}A_{\text{z}-}\sin\theta & -\frac{1}{2}A_{\text{z}+}\cos\theta \\ \frac{1}{2}A_{\text{z}-}\cos\theta & -\frac{1}{2}A_{\text{z}+}\sin\theta & \omega_{\text{eff}}-\omega_{0\text{I}} & 0 \\ -\frac{1}{2}A_{\text{z}+}\sin\theta & -\frac{1}{2}A_{\text{z}-}\cos\theta & 0 & -\omega_{\text{eff}}-\omega_{0\text{I}} \end{pmatrix}, \tag{4.13}$$

where $\omega_{\text{eff}} = \sqrt{\Omega_{\text{S}}^2 + \omega_{1\text{S}}^2}$ as we have seen before.

For polarization transfer we need only consider the ZQ and DQ transitions, i.e. the $|1\rangle \leftrightarrow |4\rangle$ and the $|2\rangle \leftrightarrow |3\rangle$ submatrices. The $\pm\frac{1}{2}A_{\text{z}\pm}\cos\theta$ terms are outside these submatrices, but these will not affect polarization transfer between the electron and nucleus, but rather only result in a slight mixing of nuclear spin states. Diagonalizing the 2×2 submatrices is straightforward via the angles $\tan^{-1}\left(\frac{1}{2}A_{\text{z}+}\sin\theta/(\omega_{\text{eff}}\pm\omega_{0\text{I}})\right)$ for effective fields

$$\alpha_{\pm} = \sqrt{(\omega_{\text{eff}}\pm\omega_{0\text{I}})^2 + \left|\frac{1}{2}A_{\text{z}+}\right|^2\sin^2\theta}. \tag{4.14}$$

Applying evolution under these two separately to the initial density operator, tilted by θ, yields opposite signs of polarization transfer. Combining the two by subtracting one from the other results in a final nuclear polarization

$$P_{\text{I}}(t) = -P_0\cos\theta\sin^2\theta\left|\frac{1}{2}A_{\text{z}+}\right|^2\left(\frac{1}{\alpha_-^2}(1-\cos\alpha_- t) - \frac{1}{\alpha_+^2}(1-\cos\alpha_+ t)\right), \tag{4.15}$$

where P_0 is the initial electron polarization.

In the SE and related mechanisms like NOVEL and ISE, the nuclear polarization occurs at $\omega_{\text{eff}} \approx \pm\omega_{0\text{I}}$, but we are interested in polarization transfer with relatively weak microwave irradiation near the electron resonance, i.e. $\omega_{\text{eff}} \ll \omega_{0\text{I}}$. In addition, by taking $\left|\frac{1}{2}A_{\text{z}+}\right| \ll \omega_{0\text{I}}$, which is generally true at high fields, we can truncate $\alpha_{\pm}$ to only those

terms involving ω_{0I}:

$$\alpha_{\pm} \approx \sqrt{\omega_{0I}^2 \pm 2\omega_{0I}\omega_{\text{eff}}}, \tag{4.16}$$

further yielding

$$\begin{aligned} \frac{1}{\alpha_-^2} - \frac{1}{\alpha_+^2} &\approx \frac{4\omega_{\text{eff}}}{\omega_{0I}^3} \\ \frac{1}{\alpha_-^2} - \frac{1}{\alpha_+^2} &\approx \frac{2}{\omega_{0I}^2} \\ \alpha_- + \alpha_+ &\approx 2\omega_{0I} \\ \alpha_- - \alpha_+ &\approx -2\omega_{\text{eff}}. \end{aligned} \tag{4.17}$$

With some rearrangements of Equation (4.15) we have

$$P_I(t) = -P_0 \cos\theta \sin^2\theta \left|\frac{1}{2}A_{z+}\right|^2 \left\{\frac{2}{\omega_{0I}^2}\sin\omega_{\text{eff}}t \sin\omega_{0I}t + \frac{4\omega_{\text{eff}}}{\omega_{0I}^3}(2 - \cos\omega_{\text{eff}}t\cos\omega_{0I}t)\right\}. \tag{4.18}$$

In a real sample, the ESR transition is broadened by g-tensor anisotropy, multiple hyperfine interactions, and potential electron-electron interactions, implying a distribution in the values of ω_{eff} according to the ESR lineshape. After integration over this lineshape, the oscillating terms average to zero with a characteristic time on the order of $1/\Delta_{\text{ESR}}$ where Δ_{ESR} is the ESR linewidth. Averaging the $\sin\omega_{\text{eff}}t$ and $\cos\omega_{\text{eff}}t$ in Equation (4.18) and inserting the definitions of θ and ω_{eff}, we have an enhanced nuclear polarization

$$\Delta P_I^{\infty} = -P_0 \frac{2|A_{z+}|^2\omega_{1S}^2}{\omega_{0I}^3}\frac{\Omega_S}{\Omega_S^2 + \omega_{1S}^2}. \tag{4.19}$$

By the same process the component of the electron polarization along the effective field is reduced by an amount

$$\Delta P_S^{\infty} = -P_0 \frac{2|A_{z+}|^2\omega_{1S}^2}{\omega_{0I}^2}\frac{\Omega_S}{\left[\Omega_S^2 + \omega_{1S}^2\right]^{3/2}}. \tag{4.20}$$

Finally, we incorporate the ESR lineshape by convolution with Equation (4.19), assuming

the lineshape is a Lorentzian with width D. The final expression is

$$\Delta P_I^{\infty} = -P_0 \frac{2|A_{z+}|^2 \omega_{1S}^2}{\omega_{0I}^3} \frac{\Omega_S}{\Omega_S^2 + (\omega_{1S} + D)^2}. \tag{4.21}$$

As a function of the microwave offset, the final polarization P_I^{∞} has the shape of the derivative of a Lorentzian. It has extrema at $\Omega_S = \pm(\omega_{1S} + D)$. At these extrema,

$$\Delta P_I^{\infty} = \mp P_0 \frac{|A_{z+}|^2 \omega_{1S}^2}{\omega_{0I}^3 (\omega_{1S} + D)}. \tag{4.22}$$

Thus, the analytical treatment yields a dispersive profile, consistent with our data and others. Moreover, the enhancement is due to the mixing the electron and nuclear spin states induced by the microwave field when it is tuned near the resonance frequency of the electron spins. It is also a differential effect: the resulting nuclear polarization is the difference between the contributions of the ZQ and DQ sub-matrices.

It should be noted that not all electron polarization is transfered to the nuclear spin (compare Equations (4.19) and (4.20)). Furthermore, the transfer of polarization is almost instantaneous upon switching on the microwave field: a stationary nuclear polarization is achieved coherently after a time on the order of $1/\Delta_{ESR}$. Together, these effects lead to repeatable polarization transfer: the transverse components of the electron magnetization (off-diagonal coherences in the density matrix) decay to zero due to transverse relaxation during this time, while the magnitude of the polarization remains almost unchanged. Continued evolution can then re-create these coherences and then lead to buildup of an appreciable nuclear polarization.

4.2.3 Experiments and simulations of resonant mixing

With this theoretical background, we sought new experimental data which could provide evidence that this mechanism is indeed active for trityl at high fields. We examined

the ^{1}H DNP enhancement profile of 80 mM trityl-OX063 in 6:3:1 (vol.) DMSO-d_6:D_2O:H_2O at $\omega_{0I}/2\pi = 600$ MHz, shown in Figure 4.11. We observe the characteristic dispersive profile near the center, with a maximum enhancement ~5. That we observe the profile at this high field (higher than previous observations) further suggests that TM is not responsible for this enhancement – the electron-electron couplings that enable TM are field-independent and become smaller relative to ω_{0I} at higher fields.

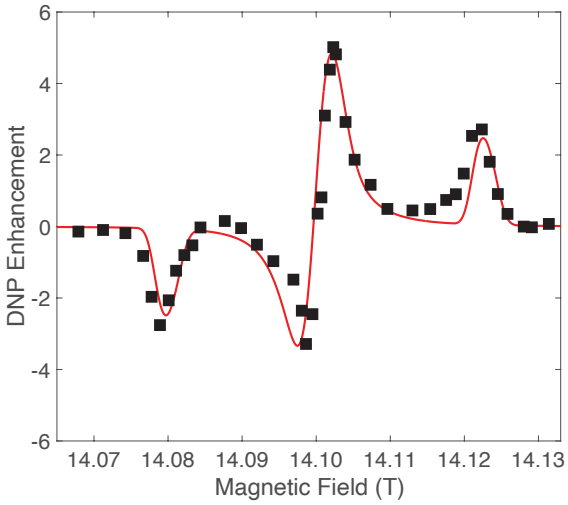

Figure 4.11: ^{1}H DNP enhancement profile for 80 mM trityl-OX063 in 6:3:1 (vol.) DMSO-d_6:D_2O:H_2O at $\omega_{0I}/2\pi = 600$ MHz, 95 K, and $\omega_r/2\pi = 8$ kHz. The sample was irradiated with a 17 W gyrotron. The solid line is the SpinEvolution simulation of a dipolar-coupled electron-nuclear spin pair using the following parameters: $\omega_{1S}/2\pi = 1.6$ MHz, $T_{1e} = 1$ ms, $T_{2e} = 0.2$ µs, and the cross-relaxation times $T_{1,ZQ} = 0.999\,75$ ms, $T_{1,DQ} = 1$ ms, $T_{2,ZQ} = T_{2,DQ} = 0.2$ µs.

Using the EPR spectrum recorded at 140 GHz (Figure 4.6), we can attempt a more detailed analysis of the strength of the dipolar couplings. The extra broadening from 8 to 80 mM is ~11 MHz, quite consistent with a simple assumption of a homogeneous distribution of radicals leading to an inter-electron distance of 2.7 nm which corresponds to a dipolar interaction of 8 MHz. The effect of "clustering" is simply not dramatic enough on the EPR line to support the claims of intense electron-electron interactions leading to TM.

Along with the experimental data, we have used the SpinEvolution software[147] to

simulate a model system of a simple dipolar-coupled electron-nuclear spin pair. In Figure 4.11 we include the simulation results, and show the same for the profile of 100 mM OX063 at $\omega_{0I}/2\pi = 380$ MHz in Figure 4.12. For the simulations, we plot the static nuclear polarization under CW microwave irradiation with typical T_{1e} and T_{2e} values for samples at these concentrations. We do include phenomenological ZQ and DQ cross-relaxation to fit the magnitude and slight asymmetry of the profiles. In SpinEvolution, the transverse cross-relaxation rates are the relaxation of the off-diagonal elements of the density matrix as in the Solomon equations[104].

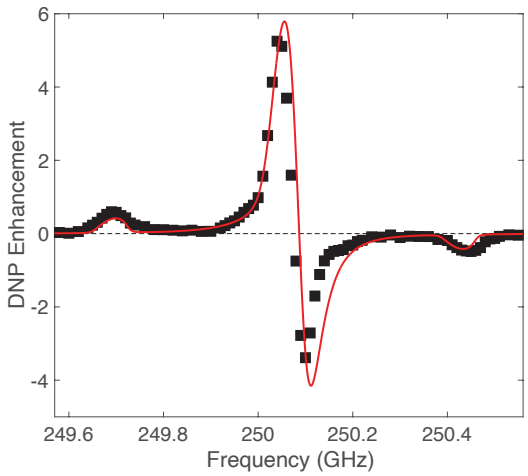

Figure 4.12: ^{1}H DNP field profile for 100 mM trityl-OX063 in 6:3:1 (vol.) DMSO-d_6:D_2O:H_2O at $\omega_{0I}/2\pi = 380$ MHz, 100 K with MAS frequency 6 kHz and irradiated with 160 mW microwaves, also shown in Figure 4.4(A). The solid line is the SpinEvolution simulation of a dipolar-coupled electron-nuclear spin pair using the following parameters: $\omega_{1S}/2\pi = 0.25$ MHz, $T_{1e} = 4$ ms, $T_{2e} = 0.05$ µs, and the cross-relaxation times $T_{1,ZQ} = 1.9995$ ms, $T_{1,DQ} = 2$ ms, $T_{2,ZQ} = T_{2,DQ} = 0.5$ µs.

To further understand the dispersive shape of the DNP profile, we performed additional simulations and also compared these to the analytical solution in Equation (4.15), shown in Figure 4.13. Again, the spin system is a single $S = 1/2$ electron and a single $I = 1/2$ nucleus. As RM and SE involve the same spin interactions, Equation (4.15) predicts both effects, illustrated in the red curve in Figure 4.13 which also matches the numerical simulation. Even without any relaxation effects, we observe a weak dispersive DNP profile at the EPR resonance. Without any cross-relaxation we cannot attribute

the enhancement to the OE, and as the simulation only includes a single electron both CE and TM are precluded. We also see that the introduction of *equal* cross-relaxation rates leads to a large antisymmetric profile – note that the OE relies specifically on the difference between the ZQ and DQ relaxation rates.

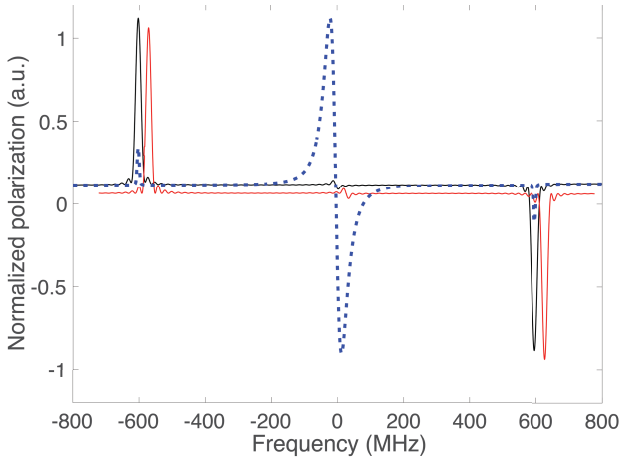

Figure 4.13: ^{1}H DNP enhancement profile from a SpinEvolution simulation (black) and an analytical calculation using Equation (4.15) (red) for one electron and one nucleus. The red trace is offset from the simulation for clarity. The following parameters are used: $\omega_{0I}/2\pi = 600$ MHz, $\omega_{1S}/2\pi = 0.5$ MHz, polarization evaluated at $t = 50$ ns (on the order of T_{2e}). The dotted blue line shows the SpinEvolution in the case of CW irradiation using the following relaxation times: $T_{1e} = 1$ ms, $T_{2e} = 0.2$ µs, and the cross-relaxation times $T_{1,ZQ} = T_{1,DQ} = 1$ ms, $T_{2,ZQ} = T_{2,DQ} = 0.5$ µs.

Simulation details

The SpinEvolution script used for Figure 4.11 is

```
****** The System ***********************************
spectrometer (MHz) 600
spinning_freq(kHz) *
channels           e H1
nuclei             e H1
atomic_coords      *
cs_isotropic       *
csa_parameters     *
g_tensor           1 2.0032 2.0032 2.0026 0 0 0
j_coupling         *
spin-spin_coupling 1 2 868 -2125 0 0 10 0
quadrupole         *
dip_switchboard    *
csa_switchboard    *
```

```
exchange_nuclei     *
bond_len_nuclei     *
bond_ang_nuclei     *
tors_ang_nuclei     *
groups_nuclei       *
******* Pulse Sequence ******************************
CHN 1
timing(usec)        10000000
power(kHz)          1600
phase(deg)          0
freq_offs(kHz)      0
CHN 2
timing(usec)        10000000
power(kHz)          0
phase(deg)          0
freq_offs(kHz)      0
******* Variables ***********************************
spin_temp=100
scan_par1d x/-2:0.0001:2/
freq_1_1=x*600000
T2ZQ=0.0002
T2DQ=0.0002
T1ZQ=0.99975
T1DQ=1
T2e=0.0002
T1e=1
T1ZQ_1_2=T1ZQ
T1DQ_1_2=T1DQ
T2ZQ_1_2=T2ZQ
T2DQ_1_2=T2DQ
T1SQ_1_1=T1e
T2SQ_1_1=T2e
******* Options **************************************
rho0                Ieq
observables         I2z
EulerAngles         zcw233
n_gamma             *
line_broaden(Hz)    *
zerofill            *
FFT_dimensions      *
options             -ns1 -dp -re -vclk -v0 -lv -rmz -scheck16 -id5e6
```

4.3 Conclusions

In this chapter, two new or previously unexplored mechanisms have been observed experimentally and justified theoretically. In the case of the three-spin solid effect, the mechanism was known, but new techniques enabled observation of large enhance-

ments. By combining experimental results on a series of different radicals with electronic structure calculations of the hyperfine couplings, we demonstrated which particular nuclei are involved in the TSSE process in trityl, and used these results to claim an upper bound on the spin diffusion barrier – *using only DNP data*. Further research on polarization transfer and spin diffusion pathways in other radical systems, possibly exploiting TSSE, hyperpolarization resurgence[122], direct EPR measurements, and new tools yet to be uncovered will all aid in the design of better DNP radicals and experiments.

Resonant mixing was originally an unexplained fluctuation in the DNP profiles of trityl, with most under the assumption that it was thermal mixing becoming prevalent at high concentrations. However, noting that TM is also conventionally not considered likely at high fields, we investigated further. With several DNP profiles at 380 MHz, we elucidated some role of both concentration and also the glassing matrix. An unexpected ^{1}H–^{13}C NOE at the ^{1}H SE condition countered the possibility of the dominance of the electron-electron network and thus TM; turning back to the Hamiltonian of a single electron-nuclear system with weak on-resonance microwave irradiation led us to RM. The physical origin of RM is a state mixing process induced by the microwave and the hyperfine interaction, similar to the SE, but with nuclear polarization resulting when the microwaves are on-resonance. RM predicts the dispersive enhancement profile that we and others have observed, with amplitude and asymmetry now functions of cross-relaxation rates, but not necessarily requiring fast or largely different cross-relaxation as in the case of the Overhauser effect. With that said, there is clearly a need for further investigation of the relaxation mechanisms, both for RM and OE DNP. Under the right conditions, large enhancements can be observed even in the limit of very low microwave power, which may well be of great use as we continue to bring DNP to ever higher fields.

Chapter 5

Conclusions

One might see the research of the previous chapters of this thesis as disparate: we built a new microwave source to do pulsed DNP one day (Chapter 2), then we looked at different radicals to further investigate the Overhauser effect (Chapter 3), and then we ventured into new territory with the three-spin solid effect and resonant mixing DNP mechanisms (Chapter 4). But every project I have worked on has had an eye towards the question of "*How should we be doing DNP at high fields?*"

Pulsed DNP is one answer as its mechanisms do not inherently decline in efficiency at higher fields, but the instrumental demands are very strict. Constructing the AWG-based microwave source was a needed step towards implementing pulsed DNP at our 250 GHz DNP spectrometer – in principle all that's left is either a probe with a resonant cavity or an amplifier with sufficient power for pulsed DNP under MAS, and efforts towards both are already underway. Moreover, it is my hope that by documenting not only the final results but also our initial efforts and rejected design, we can demonstrate for the DNP community how to go about building solid-state sources even for routine CW DNP. We have certainly made extensive use of the AWG source even in CW mode, and as the solid-state sources continue to climb higher in power it seems likely that many groups will prefer the compact and relatively inexpensive devices over gyrotrons. I would ar-

gue that the solid-state source has enabled us to investigate DNP mechanisms more routinely: both Chapters 3 and 4 demonstrate heavy use of the system in conjunction with systematic sample modifications to observe their implications on DNP.

As for those mechanistic studies, the Overhauser effect in particular has always been of interest for high-field use since Cody et al. initially showed that the BDPA enhancement went *up* with increasing magnetic field. We showed that the [α, γ] protons of BDPA are critical to the OE, that the [β, δ] protons are of secondary importance, possibly contributing to spin diffusion, and finally that the phenyl protons actually contribute *negatively* to the OE, ending up with a radical that achieves even larger OE enhancements than BDPA, that being Phe-d_5-BDPA. We also showed that more is at play in the OE than the mere existence of large scalar couplings with the modified trityls. That is, there is something about BDPA, perhaps the mixed valence character that Pylaeva and colleagues have suggested, which leads to rapid scalar cross-relaxation. The more we understand the OE, the more likely we are to be able to use it routinely for high-field DNP; it may indeed be the best choice for high fields if microwave power is going to be a limiting factor.

Our study of resonant mixing was driven by scientific curiosity – an unexpected but recurrent effect in DNP profiles of trityl that drove us, especially Ravi, to look much deeper. The central dispersive feature depended on the radical concentration and also were sensitive to the glassing matrix. Certainly, aggregation of the trityl molecules was likely occurring at high concentration, but it was unclear if that was enough to lead to true thermal mixing or if some other mechanism was at play. A startling result came about in the ^{13}C enhancement profile: a negative enhancement at the ^{1}H SE condition. We read this as an indication that the dense electron network needed for TM was not really there, and we looked elsewhere for an explanation of that central dispersive profile. Yifan was instrumental in putting together the RM theory, which showed that a dispersive profile could be the result of even an isolated electron-nuclear spin pair and

even without invoking phenomenological relaxation. With that said, relaxation did seem a critical parameter in determining the final enhancement profile in simulations. Understanding the fluctuations leading to the relaxation and incorporating the relaxation into the quantum mechanical derivation of RM will further bolster our ability to explain observed enhancement profiles, which are our main tool in distinguishing polarizing agents.

The odd one out, in a way, is the three-spin solid effect study. Unlike the others, all the experiments for the TSSE were done at 0.35 T rather than high fields. Certainly the mechanism itself is not practical for higher fields, considering it scales even more poorly than the solid effect which is already mostly disqualified. But we demonstrated how a DNP parameter can also be a probe of the radical environment, using electronic structure calculations, sequential sample modifications, and numerical simulations to draw conclusions about the polarization transfer pathway and the spin diffusion barrier. Even if the TSSE mechanism is not suited for high fields, the construction of that study is potentially a useful model for future studies, and the conclusions we were able to draw still have implications for higher fields as well.

Circling back to the main question of "*How should we be doing DNP at high fields?*", I can offer a few insights into an answer that many will still be seeking for a while to come. First, solid-state sources and especially easily manipulable ones equipped with an AWG should be a part. The diodes are getting better all the time, and the ease of use even for routine CW work cannot be overstated. Pulsed DNP will also be a possibility with these sources, and adopting it will be a boon to the field. Second, we can make the Overhauser effect work. We now have information on what's special about BDPA: structural motifs to favor and avoid in the selection of new radicals for DNP. All that's needed now is one that works well in aqueous matrices; we have seen one candidate in NMe_3-BDPA and there are no doubt more on the way. Finally, we should stay curious and keep exploring the many unexpected results that might seem easy to write off: we often

operate in uncharted waters with new samples at ever higher fields, and we don't know what an unexpected result might lead to. We might find them useful probes of certain parameters, or maybe they will lead to new theory; in any case our understanding of DNP will improve for our next venture.

Bibliography

[1] W. Gerlach and O. Stern. Der experimentelle nachweis des magnetischen moments des silberatoms. *Zeitschrift für Physik*, 8(1):110–111, Dec 1922.

[2] R. Frisch and O. Stern. Über die magnetische ablenkung von wasserstoffmolekülen und das magnetische moment des protons. i. *Zeitschrift für Physik*, 85(1–2):4–16, Jan 1933.

[3] I. Estermann and O. Stern. Über die magnetische ablenkung von wasserstoffmolekülen und das magnetische moment des protons. ii. *Zeitschrift für Physik*, 85(1–2):17–24, Jan 1933.

[4] L. W. Alvarez and F. Bloch. A quantitative determination of the neutron moment in absolute nuclear magnetons. *Physical Review*, 57(2):111–122, Jan 1940.

[5] P. Zeeman. On the influence of magnetism on the nature of the light emitted by a substance. *The London, Edinburgh, and Dublin Philosophical Magazine and Journal of Science*, 43(262):226–239, Mar 1897.

[6] M. Hong. Advanced NMR Spectroscopy, course notes, 2018.

[7] I. I. Rabi, J. R. Zacharias, S. Millman, and P. Kusch. A new method of measuring nuclear magnetic moment. *Physical Review*, 53(4):318–318, Feb 1938.

[8] E. M. Purcell, H. C. Torrey, and R. V. Pound. Resonance absorption by nuclear magnetic moments in a solid. *Physical Review*, 69(1–2):37–38, Jan 1946.

[9] F. Bloch. Nuclear induction. *Physical Review*, 70(7–8):460–474, Oct 1946.

[10] R. R. Ernst and W. A. Anderson. Application of Fourier transform spectroscopy to magnetic resonance. *Review of Scientific Instruments*, 37(1):93–102, Jan 1966.

[11] W. P. Aue, E. Bartholdi, and R. R. Ernst. Two-dimensional spectroscopy. Application to nuclear magnetic resonance. *The Journal of Chemical Physics*, 64 (5):2229–2246, Mar 1976.

[12] M. H. Levitt. *Spin Dynamics: Basics of nuclear magnetic resonance*. Wiley, 2015.

[13] E. R. Andrew, A. Bradbury, and R. G. Eades. Nuclear magnetic resonance spectra from a crystal rotated at high speed. *Nature*, 182(4650):1659, December 1958.

[14] I. J. Lowe. Free induction decays of rotating solids. *Phys. Rev. Lett.*, 2:285–287, Apr 1959.

[15] J. Herzfeld and A. E. Berger. Sideband intensities in NMR spectra of samples spinning at the magic angle. *The Journal of Chemical Physics*, 73(12):6021–6030, Dec 1980.

[16] A. E. Bennett, C. M. Rienstra, M. Auger, K. V. Lakshmi, and R. G. Griffin. Heteronuclear decoupling in rotating solids. *The Journal of Chemical Physics*, 103 (16):6951–6958, Oct 1995.

[17] B. Fung, A. Khitrin, and K. Ermolaev. An improved broadband decoupling sequence for liquid crystals and solids. *Journal of Magnetic Resonance*, 142(1): 97–101, Jan 2000.

[18] A. Detken, E. H. Hardy, M. Ernst, and B. H. Meier. Simple and efficient decoupling in magic-angle spinning solid-state NMR: the XiX scheme. *Chemical Physics Letters*, 356(3-4):298–304, Apr 2002.

[19] T. Gullion and J. Schaefer. Rotational-echo double-resonance NMR. *Journal of Magnetic Resonance (1969)*, 81(1):196–200, Jan 1989.

[20] D. Raleigh, M. Levitt, and R. Griffin. Rotational resonance in solid state NMR. *Chemical Physics Letters*, 146(1–2):71–76, Apr 1988.

[21] K. Takegoshi, S. Nakamura, and T. Terao. 13C-1H dipolar-assisted rotational resonance in magic-angle spinning NMR. *Chemical Physics Letters*, 344(5–6): 631–637, Aug 2001.

[22] L. Liang, Y. Ji, K. Chen, P. Gao, Z. Zhao, and G. Hou. Solid-state NMR dipolar and chemical shift anisotropy recoupling techniques for structural and dynamical studies in biological systems. *Chemical Reviews*, 122(10):9880–9942, Jan 2022.

[23] A. W. Overhauser. Polarization of nuclei in metals. *Physical Review*, 92(2):411–415, Oct 1953.

[24] T. R. Carver and C. P. Slichter. Polarization of nuclear spins in metals. *Physical Review*, 92(1):212–213, Oct 1953.

[25] A. Abragam and W. G. Proctor. Une nouvelle méthode de polarisation dynamique des noyaux atomiques dans les solides. *Comp. Rend. Acad. Sci*, 246:2253–2256, 1958.

[26] C. F. Hwang and D. A. Hill. Phenomenological model for the new effect in dynamic polarization. *Physical Review Letters*, 19(18):1011–1014, Oct 1967.

[27] A. Abragam and M. Goldman. Principles of dynamic nuclear polarisation. *Reports on Progress in Physics*, 41(3):395–467, Mar 1978.

[28] I. Kuprov. Spin Dynamics, lecture notes, 2013.

[29] T. V. Can, M. A. Caporini, F. Mentink-Vigier, B. Corzilius, J. J. Walish, M. Rosay, W. E. Maas, M. Baldus, S. Vega, T. M. Swager, and R. G. Griffin. Overhauser effects in insulating solids. *The Journal of Chemical Physics*, 141(6), Aug 2014.

[30] C. Ramanathan. Dynamic nuclear polarization and spin diffusion in nonconducting solids. *Applied Magnetic Resonance*, 34(3–4), Aug 2008.

[31] O. Haze, B. Corzilius, A. A. Smith, R. G. Griffin, and T. M. Swager. Water-soluble narrow-line radicals for dynamic nuclear polarization. *Journal of the American Chemical Society*, 134(35):14287–14290, Aug 2012.

[32] A. Gurinov, B. Sieland, A. Kuzhelev, H. Elgabarty, T. D. Kühne, T. Prisner, J. Paradies, M. Baldus, K. L. Ivanov, and S. Pylaeva. Mixed-valence compounds as polarizing agents for overhauser dynamic nuclear polarization in solids. *Angewandte Chemie International Edition*, 60(28):15371–15375, Jun 2021.

[33] A. S. L. Thankamony, J. J. Wittmann, M. Kaushik, and B. Corzilius. Dynamic nuclear polarization for sensitivity enhancement in modern solid-state NMR. *Progress in Nuclear Magnetic Resonance Spectroscopy*, 102-103:120–195, Nov 2017.

[34] C. Song, K.-N. Hu, C.-G. Joo, T. M. Swager, and R. G. Griffin. TOTAPOL: A biradical polarizing agent for dynamic nuclear polarization experiments in aqueous media. *Journal of the American Chemical Society*, 128(35):11385–11390, Aug 2006.

[35] A. Lund, G. Casano, G. Menzildjian, M. Kaushik, G. Stevanato, M. Yulikov, R. Jabbour, D. Wisser, M. Renom-Carrasco, C. Thieuleux, F. Bernada, H. Karoui, D. Siri, M. Rosay, I. V. Sergeyev, D. Gajan, M. Lelli, L. Emsley, O. Ouari, and A. Lesage. TinyPols: a family of water-soluble binitroxides tailored for dynamic nuclear polarization enhanced NMR spectroscopy at 18.8 and 21.1 t. *Chemical Science*, 11(10):2810–2818, 2020.

[36] G. Mathies, M. A. Caporini, V. K. Michaelis, Y. Liu, K.-N. Hu, D. Mance, J. L. Zweier, M. Rosay, M. Baldus, and R. G. Griffin. Efficient dynamic nuclear polarization at 800 MHz/527 GHz with trityl-nitroxide biradicals. *Angewandte Chemie International Edition*, 54(40):11770–11774, Aug 2015.

[37] F. Mentink-Vigier. Optimizing nitroxide biradicals for cross-effect MAS-DNP: the role of g-tensors' distance. *Physical Chemistry Chemical Physics*, 22(6):3643–3652, 2020.

[38] G. Menzildjian, J. Schlagnitweit, G. Casano, O. Ouari, D. Gajan, and A. Lesage. Polarizing agents for efficient high field DNP solid-state NMR spectroscopy under magic-angle spinning: from design principles to formulation strategies. *Chemical Science*, 14(23):6120–6148, 2023.

[39] K. R. Thurber and R. Tycko. Theory for cross effect dynamic nuclear polarization under magic-angle spinning in solid state nuclear magnetic resonance: The importance of level crossings. *The Journal of Chemical Physics*, 137(8), Aug 2012.

[40] F. Mentink-Vigier, S. Paul, D. Lee, A. Feintuch, S. Hediger, S. Vega, and G. D. Paëpe. Nuclear depolarization and absolute sensitivity in magic-angle spinning cross effect dynamic nuclear polarization. *Physical Chemistry Chemical Physics*, 17(34): 21824–21836, 2015.

[41] A. Equbal, A. Leavesley, S. K. Jain, and S. Han. Cross-effect dynamic nuclear polarization explained: Polarization, depolarization, and oversaturation. *The Journal of Physical Chemistry Letters*, 10(3):548–558, Jan 2019.

[42] S. Goertz. The dynamic nuclear polarization process. *Nuclear Instruments and Methods in Physics Research Section A: Accelerators, Spectrometers, Detectors and Associated Equipment*, 526(1-2):28–42, Jun 2004.

[43] K. O. Tan, S. Jawla, R. J. Temkin, and R. G. Griffin. *Pulsed Dynamic Nuclear Polarization*, pages 339–352. John Wiley & Sons, Ltd, 2019. ISBN 9780470034590.

[44] R. A. Wind, L. Li, H. Lock, and G. E. Maciel. Dynamic nuclear polarization in the nuclear rotating frame. *Journal of Magnetic Resonance (1969)*, 79(3):577–582, Oct 1988.

[45] C. Farrar, D. Hall, G. Gerfen, M. Rosay, J.-H. Ardenkjær-Larsen, and R. Griffin. High-frequency dynamic nuclear polarization in the nuclear rotating frame. *Journal of Magnetic Resonance*, 144(1):134–141, May 2000.

[46] V. Weis, M. Bennati, M. Rosay, and R. G. Griffin. Solid effect in the electron spin dressed state: A new approach for dynamic nuclear polarization. *The Journal of Chemical Physics*, 113(16):6795–6802, Oct 2000.

[47] A. Henstra, P. Dirksen, J. Schmidt, and W. Wenckebach. Nuclear spin orientation via electron spin locking (NOVEL). *Journal of Magnetic Resonance (1969)*, 77(2): 389–393, Apr 1988.

[48] S. K. Jain, G. Mathies, and R. G. Griffin. Off-resonance NOVEL. *The Journal of Chemical Physics*, 147(16), Oct 2017.

[49] A. Henstra, P. Dirksen, and W. Wenckebach. Enhanced dynamic nuclear polarization by the integrated solid effect. *Physics Letters A*, 134(2):134–136, Dec 1988.

[50] A. Henstra, T.-S. Lin, J. Schmidt, and W. Wenckebach. High dynamic nuclear polarization at room temperature. *Chemical Physics Letters*, 165(1):6–10, Jan 1990.

[51] T. V. Can, R. T. Weber, J. J. Walish, T. M. Swager, and R. G. Griffin. Frequency-swept integrated solid effect. *Angewandte Chemie*, 129(24):6848–6852, May 2017.

[52] K. O. Tan, R. T. Weber, T. V. Can, and R. G. Griffin. Adiabatic solid effect. *The Journal of Physical Chemistry Letters*, 11(9):3416–3421, Apr 2020.

[53] Y. Quan, J. Steiner, Y. Ouyang, K. O. Tan, W. T. Wenckebach, P. Hautle, and R. G. Griffin. Integrated, stretched, and adiabatic solid effects. *The Journal of Physical Chemistry Letters*, 13(25):5751–5757, Jun 2022.

[54] Y. Quan, M. V. H. Subramanya, Y. Ouyang, M. Mardini, T. Dubroca, S. Hill, and R. G. Griffin. Coherent dynamic nuclear polarization using chirped pulses. *The Journal of Physical Chemistry Letters*, 14(20):4748–4753, May 2023.

[55] K. O. Tan, C. Yang, R. T. Weber, G. Mathies, and R. G. Griffin. Time-optimized pulsed dynamic nuclear polarization. *Science Advances*, 5(1), Jan 2019.

[56] V. S. Redrouthu and G. Mathies. Efficient pulsed dynamic nuclear polarization with the x-inverse-x sequence. *Journal of the American Chemical Society*, 144(4): 1513–1516, Jan 2022.

[57] N. Wili, A. B. Nielsen, L. A. Völker, L. Schreder, N. C. Nielsen, G. Jeschke, and K. O. Tan. Designing broadband pulsed dynamic nuclear polarization sequences in static solids. *Science Advances*, 8(28), Jul 2022.

[58] V. S. Redrouthu, S. Vinod-Kumar, and G. Mathies. Dynamic nuclear polarization by two-pulse phase modulation. *The Journal of Chemical Physics*, 159(1), Jul 2023.

[59] I. Scholz, B. H. Meier, and M. Ernst. Operator-based triple-mode floquet theory in solid-state NMR. *The Journal of Chemical Physics*, 127(20), Nov 2007.

[60] I. Scholz, J. D. van Beek, and M. Ernst. Operator-based floquet theory in solid-state NMR. *Solid State Nuclear Magnetic Resonance*, 37(3-4):39–59, May 2010.

[61] L. R. Becerra, G. J. Gerfen, R. J. Temkin, D. J. Singel, and R. G. Griffin. Dynamic nuclear polarization with a cyclotron resonance maser at 5 t. *Physical Review Letters*, 71(21):3561–3564, Nov 1993.

[62] M. Blank and K. L. Felch. *Millimeter-Wave Sources for DNP-NMR*, pages 155–166. John Wiley & Sons, Ltd, 2018. ISBN 9780470034590.

[63] F. J. Scott, E. P. Saliba, B. J. Albert, N. Alaniva, E. L. Sesti, C. Gao, N. C. Golota, E. J. Choi, A. P. Jagtap, J. J. Wittmann, M. Eckardt, W. Harneit, B. Corzilius, S. T. Sigurdsson, and A. B. Barnes. Frequency-agile gyrotron for electron decoupling and pulsed dynamic nuclear polarization. *Journal of Magnetic Resonance*, 289: 45–54, Apr 2018.

[64] C. Gao, N. Alaniva, E. P. Saliba, E. L. Sesti, P. T. Judge, F. J. Scott, T. Halbritter, S. T. Sigurdsson, and A. B. Barnes. Frequency-chirped dynamic nuclear polarization with magic angle spinning using a frequency-agile gyrotron. *Journal of Magnetic Resonance*, 308:106586, Nov 2019.

[65] J. L. Hesler and T. Crowe. High-power solid-state terahertz sources. *SPIE Newsroom*, 2015.

[66] I. V. Sergeyev, F. Aussenac, A. Purea, C. Reiter, E. Bryerton, S. Retzloff, J. Hesler, L. Tometich, and M. Rosay. Efficient 263 GHz magic angle spinning DNP at 100 K using solid-state diode sources. *Solid State Nuclear Magnetic Resonance*, 100: 63–69, Aug 2019.

[67] V. Weis, M. Bennati, M. Rosay, J. Bryant, and R. Griffin. High-field DNP and ENDOR with a novel multiple-frequency resonance structure. *Journal of Magnetic Resonance*, 140(1):293–299, Sep 1999.

[68] A. A. Smith, B. Corzilius, J. A. Bryant, R. DeRocher, P. P. Woskov, R. J. Temkin, and R. G. Griffin. A 140 GHz pulsed EPR/212 MHz NMR spectrometer for DNP studies. *Journal of Magnetic Resonance*, 223:170–179, Oct 2012.

[69] A. V. Soane, M. A. Shapiro, S. Jawla, and R. J. Temkin. Operation of a 140-GHz gyro-amplifier using a dielectric-loaded, severless confocal waveguide. *IEEE Transactions on Plasma Science*, 45(10):2835–2840, Oct 2017.

[70] E. A. Nanni, S. M. Lewis, M. A. Shapiro, R. G. Griffin, and R. J. Temkin. Photonic-band-gap traveling-wave gyrotron amplifier. *Physical Review Letters*, 111 (23), Dec 2013.

[71] C. D. Joye, A. M. Cook, J. P. Calame, K. T. Nguyen, E. L. Wright, J. M. Hanna, D. E. Pershing, and D. K. Abe. Development of a 233 GHz high-gain traveling wave amplifier. In *IEEE International Vacuum Electronics Conference*. IEEE, Apr 2014.

[72] C. D. Joye, A. M. Cook, J. P. Calame, K. T. Nguyen, E. L. Wright, B. S. Albright, D. K. Abe, J. Atkinson, and T. Kimura. Microfabricated 233 GHz traveling wave amplifier. In *2016 IEEE International Vacuum Electronics Conference (IVEC)*. IEEE, Apr 2016.

[73] C. M. Armstrong, R. Kowalczyk, A. Zubyk, K. Berg, C. Meadows, D. Chan, T. Schoemehl, R. Duggal, N. Hinch, R. B. True, R. Tobin, M. Sweeney, and B. Weatherford. A compact extremely high frequency MPM power amplifier. *IEEE Transactions on Electron Devices*, 65(6):2183–2188, Jun 2018.

[74] M. Mardini, R. S. Palani, I. M. Ahmad, S. Mandal, S. K. Jawla, E. Bryerton, R. J. Temkin, S. T. Sigurdsson, and R. G. Griffin. Frequency-swept dynamic nuclear polarization. *Journal of Magnetic Resonance*, 353:107511, Aug 2023.

[75] A. A. Smith, B. Corzilius, A. B. Barnes, T. Maly, and R. G. Griffin. Solid effect dynamic nuclear polarization and polarization pathways. *The Journal of Chemical Physics*, 136(1), Jan 2012.

[76] A. A. Smith, B. Corzilius, O. Haze, T. M. Swager, and R. G. Griffin. Observation of strongly forbidden solid effect dynamic nuclear polarization transitions via electron-electron double resonance detected NMR. *The Journal of Chemical Physics*, 139(21), Dec 2013.

[77] I. Kaminker, R. Barnes, and S. Han. Arbitrary waveform modulated pulse EPR at 200 GHz. *Journal of Magnetic Resonance*, 279:81–90, Jun 2017.

[78] I. Kaminker and S. Han. Amplification of dynamic nuclear polarization at 200 GHz by arbitrary pulse shaping of the electron spin saturation profile. *The Journal of Physical Chemistry Letters*, 9(11):3110–3115, May 2018.

[79] A. Equbal, K. Tagami, and S. Han. Pulse-shaped dynamic nuclear polarization under magic-angle spinning. *The Journal of Physical Chemistry Letters*, 10(24): 7781–7788, Dec 2019.

[80] A. Kuzhelev, D. Akhmetzyanov, V. Denysenkov, G. Shevelev, O. Krumkacheva, E. Bagryanskaya, and T. Prisner. High-frequency pulsed electron–electron double resonance spectroscopy on DNA duplexes using trityl tags and shaped microwave pulses. *Physical Chemistry Chemical Physics*, 20(41):26140–26144, 2018.

[81] L. Delage-Laurin, R. S. Palani, N. Golota, M. Mardini, Y. Ouyang, K. O. Tan, T. M. Swager, and R. G. Griffin. Overhauser dynamic nuclear polarization with selectively deuterated BDPA radicals. *Journal of the American Chemical Society*, 143(48):20281–20290, Nov 2021.

[82] R. S. Palani, M. Mardini, L. Delage-Laurin, D. Banks, Y. Ouyang, E. Bryerton, J. G. Kempf, T. M. Swager, and R. G. Griffin. Amplified overhauser DNP with selective deuteration: Attenuation of double-quantum cross-relaxation. *The Journal of Physical Chemistry Letters*, 14(1):95–100, Dec 2022.

[83] C. D. Jeffries. Polarization of nuclei by resonance saturation in paramagnetic crystals. *Physical Review*, 106(1):164–165, Apr 1957.

[84] C. D. Jeffries. Dynamic orientation of nuclei by forbidden transitions in paramagnetic resonance. *Physical Review*, 117(4):1056–1069, Feb 1960.

[85] B. Corzilius, A. A. Smith, and R. G. Griffin. Solid effect in magic angle spinning dynamic nuclear polarization. *The Journal of Chemical Physics*, 137(5), Aug 2012.

[86] A. Kessenikh, V. Lushchikov, A. Manenkov, and Y. V. Taran. Proton polarization in irradiated polyethylenes. *Soviet Phys. Solid State*, 5:321–329, 1963.

[87] A. Kessenikh and A. Manenkov. Dynamic polarization of nuclei during saturation of nonuniformly broadened electron paramagnetic resonance lines. *Soviet Physics Solid State*, 5:835–837, 1963.

[88] K.-N. Hu, H.-h. Yu, T. M. Swager, and R. G. Griffin. Dynamic nuclear polarization with biradicals. *Journal of the American Chemical Society*, 126(35):10844–10845, Aug 2004.

[89] K.-N. Hu, V. S. Bajaj, M. Rosay, and R. G. Griffin. High-frequency dynamic nuclear polarization using mixtures of TEMPO and trityl radicals. *The Journal of Chemical Physics*, 126(4), Jan 2007.

[90] K.-N. Hu, G. T. Debelouchina, A. A. Smith, and R. G. Griffin. Quantum mechanical theory of dynamic nuclear polarization in solid dielectrics. *The Journal of Chemical Physics*, 134(12), Mar 2011.

[91] K.-N. Hu, C. Song, H.-h. Yu, T. M. Swager, and R. G. Griffin. High-frequency dynamic nuclear polarization using biradicals: A multifrequency EPR lineshape analysis. *The Journal of Chemical Physics*, 128(5), Jan 2008.

[92] R. S. Palani, M. Mardini, Y. Quan, and R. G. Griffin. Dynamic nuclear polarization with trityl radicals. *Journal of Magnetic Resonance*, 349:107411, Apr 2023.

[93] Y. Quan, Y. Ouyang, M. Mardini, R. S. Palani, D. Banks, J. Kempf, W. T. Wenckebach, and R. G. Griffin. Resonant mixing dynamic nuclear polarization. *The Journal of Physical Chemistry Letters*, 14(31):7007–7013, Jul 2023.

[94] A. Fokin, M. Glyavin, G. Golubiatnikov, L. Lubyako, M. Morozkin, B. Movschevich, A. Tsvetkov, and G. Denisov. High-power sub-terahertz source with a record frequency stability at up to 1 hz. *Scientific Reports*, 8(1), Mar 2018.

[95] S.-T. Han, R. G. Griffin, K.-N. Hu, C.-G. Joo, C. D. Joye, J. R. Sirigiri, R. J. Temkin, A. C. Torrezan, and P. P. Woskov. Spectral characteristics of a 140-GHz long-pulsed gyrotron. *IEEE Transactions on Plasma Science*, 35(3):559–564, Jun 2007.

[96] C. Sauvée, M. Rosay, G. Casano, F. Aussenac, R. T. Weber, O. Ouari, and P. Tordo. Highly efficient, water-soluble polarizing agents for dynamic nuclear polarization at high frequency. *Angewandte Chemie International Edition*, 52(41):10858–10861, Aug 2013.

[97] A. Equbal, Y. Li, T. Tabassum, and S. Han. Crossover from a solid effect to thermal mixing 1H dynamic nuclear polarization with trityl-OX063. *The Journal of Physical Chemistry Letters*, 11(9):3718–3723, Apr 2020.

[98] D. Shimon, K. A. Cantwell, L. Joseph, E. Q. Williams, Z. Peng, S. Takahashi, and C. Ramanathan. Large room temperature bulk DNP of 13C via P1 centers in diamond. *The Journal of Physical Chemistry C*, 126(41):17777–17787, Oct 2022.

[99] A. B. Barnes, E. A. Nanni, J. Herzfeld, R. G. Griffin, and R. J. Temkin. A 250 GHz gyrotron with a 3 GHz tuning bandwidth for dynamic nuclear polarization. *Journal of Magnetic Resonance*, 221:147–153, Aug 2012.

[100] P. C. A. van der Wel, K.-N. Hu, J. Lewandowski, and R. G. Griffin. Dynamic nuclear polarization of amyloidogenic peptide nanocrystals: GNNQQNY, a core segment of the yeast prion protein sup35p. *Journal of the American Chemical Society*, 128 (33):10840–10846, Aug 2006.

[101] D. Schmalbein, G. G. Maresch, A. Kamlowski, and P. Höfer. The bruker high-frequency-EPR system. *Applied Magnetic Resonance*, 16(2):185–205, Feb 1999.

[102] M. Lelli, S. R. Chaudhari, D. Gajan, G. Casano, A. J. Rossini, O. Ouari, P. Tordo, A. Lesage, and L. Emsley. Solid-state dynamic nuclear polarization at 9.4 and 18.8 T from 100 K to room temperature. *Journal of the American Chemical Society*, 137 (46):14558–14561, Nov 2015.

[103] S. R. Chaudhari, D. Wisser, A. C. Pinon, P. Berruyer, D. Gajan, P. Tordo, O. Ouari, C. Reiter, F. Engelke, C. Copéret, M. Lelli, A. Lesage, and L. Emsley. Dynamic nuclear polarization efficiency increased by very fast magic angle spinning. *Journal of the American Chemical Society*, 139(31):10609–10612, Jul 2017.

[104] I. Solomon. Relaxation processes in a system of two spins. *Physical Review*, 99(2): 559–565, Jul 1955.

[105] K. Hausser and D. Stehlik. Dynamic nuclear polarization in liquids. In *Advances in Magnetic Resonance*, volume 3, pages 79–139. Elsevier, 1968.

[106] N. S. Dalal, D. E. Kennedy, and C. A. McDowell. EPR and ENDOR studies of hyperfine interactions in solutions of stable organic free radicals. *The Journal of Chemical Physics*, 61(5):1689–1697, 1974.

[107] L. Lumata, Z. Kovacs, A. D. Sherry, C. Malloy, S. Hill, J. van Tol, L. Yu, L. Song, and M. E. Merritt. Electron spin resonance studies of trityl OX063 at a concentration optimal for DNP. *Phys. Chem. Chem. Phys.*, 15:9800–9807, 2013.

[108] S. Trukhan, V. Yudanov, V. Tormyshev, O. Rogozhnikova, D. Trukhin, M. Bowman, M. Krzyaniak, H. Chen, and O. Martyanov. Hyperfine interactions of narrow-line trityl radical with solvent molecules. *Journal of Magnetic Resonance*, 233:29–36, 2013.

[109] Y. Li, A. Equbal, T. Tabassum, and S. Han. 1H thermal mixing dynamic nuclear polarization with BDPA as polarizing agents. *The Journal of Physical Chemistry Letters*, 11(21):9195–9202, Oct 2020.

[110] R. C. Lamb, J. G. Pacifici, and P. W. Ayers. Organic peroxides. IV. kinetics and products of decompositions of cyclohexaneformyl and isobutyryl peroxides. BDPA as a free-radical scavenger. *Journal of the American Chemical Society*, 87 (17):3928–3935, Sep 1965.

[111] S. Jawla, Q. Z. Ni, A. Barnes, W. Guss, E. Daviso, J. Herzfeld, R. Griffin, and R. Temkin. Continuously tunable 250 GHz gyrotron with a double disk window for DNP-NMR spectroscopy. *Journal of Infrared, Millimeter, and Terahertz Waves*, 34(1):42–52, Nov 2012.

[112] S. Pylaeva, K. L. Ivanov, M. Baldus, D. Sebastiani, and H. Elgabarty. Molecular mechanism of Overhauser dynamic nuclear polarization in insulating solids. *The Journal of Physical Chemistry Letters*, 8(10):2137–2142, Apr 2017.

[113] S. Pylaeva, P. Marx, G. Singh, T. D. Kühne, M. Roemelt, and H. Elgabarty. Organic mixed-valence compounds and the Overhauser effect in insulating solids. *The Journal of Physical Chemistry A*, 125(3):867–874, Jan 2021.

[114] K. O. Tan, M. Mardini, C. Yang, J. H. Ardenkjær-Larsen, and R. G. Griffin. Three-spin solid effect and the spin diffusion barrier in amorphous solids. *Science Advances*, 5(7), Jul 2019.

[115] M. Borghini, W. de Boer, and K. Morimoto. Nuclear dynamic polarization by resolved solid-state effect and thermal mixing with an electron spin-spin interaction reservoir. *Physics Letters A*, 48(4):244–246, Jul 1974.

[116] W. de Boer. Dynamic orientation of nuclei at low temperatures. *Journal of Low Temperature Physics*, 22(1-2):185–212, Jan 1976.

[117] G. T. Trammell, H. Zeldes, and R. Livingston. Effect of environmental nuclei in electron spin resonance spectroscopy. *Physical Review*, 110(3):630–634, May 1958.

[118] M. Bowman, L. Kevan, and R. Schwartz. Analysis of matrix nuclei spin flip satellite lines in EPR spectra: Application to trapped hydrogen atoms. *Chemical Physics Letters*, 30(2):208–211, Jan 1975.

[119] M. Bowman, C. Mailer, and H. Halpern. The solution conformation of triarylmethyl radicals. *Journal of Magnetic Resonance*, 172(2):254–267, Feb 2005.

[120] J. H. Ardenkjær-Larsen, B. Fridlund, A. Gram, G. Hansson, L. Hansson, M. H. Lerche, R. Servin, M. Thaning, and K. Golman. Increase in signal-to-noise ratio of >10,000 times in liquid-state NMR. *Proceedings of the National Academy of Sciences*, 100 (18):10158–10163, Aug 2003.

[121] M. J. Graham, C.-J. Yu, M. D. Krzyaniak, M. R. Wasielewski, and D. E. Freedman. Synthetic approach to determine the effect of nuclear spin distance on electronic spin decoherence. *Journal of the American Chemical Society*, 139(8):3196–3201, Feb 2017.

[122] Q. Stern, S. F. Cousin, F. Mentink-Vigier, A. C. Pinon, S. J. Elliott, O. Cala, and S. Jannin. Direct observation of hyperpolarization breaking through the spin diffusion barrier. *Science Advances*, 7(18), Apr 2021.

[123] P. Schosseler, T. Wacker, and A. Schweiger. Pulsed ELDOR detected NMR. *Chemical Physics Letters*, 224(3-4):319–324, Jul 1994.

[124] O. Y. Rogozhnikova, V. G. Vasiliev, T. I. Troitskaya, D. V. Trukhin, T. V. Mikhalina, H. J. Halpern, and V. M. Tormyshev. Generation of trityl radicals by nucleophilic quenching of tris(2,3,5,6-tetrathiaaryl)methyl cations and practical and convenient large-scale synthesis of persistent tris(4-carboxy-2,3,5,6-tetrathiaaryl)methyl radical. *European Journal of Organic Chemistry*, 2013(16):3347–3355, Apr 2013.

[125] M. D. Hanwell, D. E. Curtis, D. C. Lonie, T. Vandermeersch, E. Zurek, and G. R. Hutchison. Avogadro: an advanced semantic chemical editor, visualization, and analysis platform. *Journal of Cheminformatics*, 4(1), Aug 2012.

[126] F. Neese. The ORCA program system. *WIREs Computational Molecular Science*, 2 (1):73–78, Jun 2011.

[127] A.-R. Allouche. Gabedit-a graphical user interface for computational chemistry softwares. *Journal of Computational Chemistry*, 32(1):174–182, Nov 2010.

[128] S. Huzinaga. Gaussian-type functions for polyatomic systems. i. *The Journal of Chemical Physics*, 42(4):1293–1302, Feb 1965.

[129] W. Kutzelnigg, U. Fleischer, and M. Schindler. The iglo-method: Ab-initio calculation and interpretation of nmr chemical shifts and magnetic susceptibilities. In *Deuterium and Shift Calculation*, pages 165–262, Berlin, Heidelberg, 1991. Springer Berlin Heidelberg.

[130] M. L. Munzarová. DFT calculations of EPR hyperfine coupling tensors, May 2004.

[131] A. Karabanov, G. Kwiatkowski, and W. Köckenberger. Spin dynamic simulations of solid effect DNP: the role of the relaxation superoperator. *Molecular Physics*, 112 (14):1838–1854, Feb 2014.

[132] G. Mathies, S. Jain, M. Reese, and R. G. Griffin. Pulsed dynamic nuclear polarization with trityl radicals. *The Journal of Physical Chemistry Letters*, 7(1): 111–116, Dec 2015.

[133] T. V. Can, J. E. McKay, R. T. Weber, C. Yang, T. Dubroca, J. van Tol, S. Hill, and R. G. Griffin. Frequency-swept integrated and stretched solid effect dynamic nuclear polarization. *The Journal of Physical Chemistry Letters*, 9(12):3187–3192, May 2018.

[134] T. Maly, L. B. Andreas, A. A. Smith, and R. G. Griffin. 2H-DNP-enhanced 2H–13C solid-state NMR correlation spectroscopy. *Physical Chemistry Chemical Physics*, 12(22):5872, 2010.

[135] I. Marin-Montesinos, J. C. Paniagua, M. Vilaseca, A. Urtizberea, F. Luis, M. Feliz, F. Lin, S. V. Doorslaer, and M. Pons. Self-assembled trityl radical capsules – implications for dynamic nuclear polarization. *Physical Chemistry Chemical Physics*, 17(8):5785–5794, 2015.

[136] A. Karabanov, G. Kwiatkowski, C. U. Perotto, D. Wiśniewski, J. McMaster, I. Lesanovsky, and W. Köckenberger. Dynamic nuclear polarisation by thermal mixing: quantum theory and macroscopic simulations. *Physical Chemistry Chemical Physics*, 18(43):30093–30104, 2016.

[137] J. L. White and P. Mirau. Probing miscibility and intermolecular interactions in solid polymer blends using the nuclear overhauser effect. *Macromolecules*, 26 (12):3049–3054, Jun 1993.

[138] J. L. White. Exploiting methyl groups as motional labels for structure analysis in solid polymers. *Solid State Nuclear Magnetic Resonance*, 10(1-2):79–88, Dec 1997.

[139] J. Zhou, R. Fu, J. Z. Hu, L. Li, and C. Ye. Measurement of spin-lattice relaxation times of 13C in organic solids. *Solid State Nuclear Magnetic Resonance*, 7(4): 291–299, Feb 1997.

[140] S. E. Ashbrook, N. G. Dowell, I. Prokes, and S. Wimperis. Nuclear overhauser effect (NOE) enhancement of 11B NMR spectra of borane adducts in the solid state. *Journal of the American Chemical Society*, 128(21):6782–6783, May 2006.

[141] D. Daube, V. Aladin, J. Heiliger, J. J. Wittmann, D. Barthelmes, C. Bengs, H. Schwalbe, and B. Corzilius. Heteronuclear cross-relaxation under solid-state dynamic nuclear polarization. *Journal of the American Chemical Society*, 138(51): 16572–16575, Dec 2016.

[142] V. Aladin and B. Corzilius. Methyl dynamics in amino acids modulate heteronuclear cross relaxation in the solid state under MAS DNP. *Solid State Nuclear Magnetic Resonance*, 99:27–35, Jul 2019.

[143] M. M. Hoffmann, S. Bothe, T. Gutmann, and G. Buntkowsky. Unusual local molecular motions in the solid state detected by dynamic nuclear polarization enhanced NMR spectroscopy. *The Journal of Physical Chemistry C*, 121(41): 22948–22957, Oct 2017.

[144] M. M. Hoffmann, S. Bothe, T. Gutmann, F.-F. Hartmann, M. Reggelin, and G. Buntkowsky. Directly vs indirectly enhanced 13C in dynamic nuclear polarization magic angle spinning NMR experiments of nonionic surfactant systems. *The Journal of Physical Chemistry C*, 121(4):2418–2427, Jan 2017.

[145] T. Maly, G. T. Debelouchina, V. S. Bajaj, K.-N. Hu, C.-G. Joo, M. L. Mak–Jurkauskas, J. R. Sirigiri, P. C. A. van der Wel, J. Herzfeld, R. J. Temkin, and R. G. Griffin. Dynamic nuclear polarization at high magnetic fields. *The Journal of Chemical Physics*, 128 (5), Feb 2008.

[146] W. Wenckebach, A. Capozzi, S. Patel, and J. Ardenkjær-Larsen. Direct measurement of the triple spin flip rate in dynamic nuclear polarization. *Journal of Magnetic Resonance*, 327:106982, Jun 2021.

[147] M. Veshtort and R. G. Griffin. SPINEVOLUTION: A powerful tool for the simulation of solid and liquid state NMR experiments. *Journal of Magnetic Resonance*, 178(2): 248–282, Feb 2006.